Bio-Inspired Control of Roughness and Trailing Edge Noise

Ian Andrew Clark

Dissertation submitted to the Faculty of the
Virginia Polytechnic Institute and State University
in partial fulfillment of the requirements for the degree of

Doctor of Philosophy
in
Aerospace Engineering

William J. Devenport, Chair
W. Nathan Alexander, Co-Chair
K. Todd Lowe
Stewart A. L. Glegg

March 24, 2017
Blacksburg, Virginia

Keywords: Bio-Inspired, Aeroacoustics, Roughness Noise, Trailing Edge Noise, Noise Control

Bio-Inspired Control of Roughness and Trailing Edge Noise

Ian A. Clark

ABSTRACT

Noise from fluid flow over rough surfaces is an important consideration in the design and performance of certain vehicles with high surface-area-to-perimeter ratios. A new method of noise control based on the anatomy of owls is developed and consists of fabric or fibrous canopies suspended above the surface. The method is tested experimentally and is found to reduce the total far-field noise emitted by the surface. The treatment also is found to reduce the magnitude of pressure fluctuations felt by the underlying surface by up to three orders of magnitude. Experimental investigations into the effects of geometric parameters of the canopies lead to an optimized design which maximizes noise reduction.

The results obtained during the canopy experiment inspired a separate new device for the reduction of trailing edge noise. This type of noise is generated by flow past the wing of an aircraft or the blades of a wind turbine, and is a source of annoyance for those in surrounding communities. The newly developed treatment consists of small fins, or "finlets," placed near the trailing edge of an airfoil. The treatment is tested experimentally at near-full-scale conditions and is found to reduce the magnitude of far-field noise by up to 10 dB. Geometric parameters of the finlets are tested to determine the optimal size and spacing of the finlets to maximize noise reduction. Follow-up computational and experimental studies reveal the fluid mechanics behind the noise reduction by showing that the finlets produce a velocity deficit in the flow near the trailing edge and limit the magnitude and spanwise correlation lengthscale of turbulence near the trailing edge, factors which determine the magnitude of far-field noise.

In a final experiment, the finlets are applied to a marine propeller and are found to reduce not only trailing edge noise, but also noise caused by the bluntness of the trailing edge. The results of this experiment show the potential usefulness of finlets to reduce noise from rotating systems, such as fans or propellers, as well as from structures which feature blunt trailing edges.

Bio-Inspired Control of Roughness and Trailing Edge Noise

Ian A. Clark

GENERAL AUDIENCE ABSTRACT

As vehicles and other engineering structures, such as wind turbines, pass through the atmosphere or ocean, noise is produced when fluid is disturbed by their passage. The dominant source of this noise may be a certain geometrical or structural feature depending on the type of vehicle or structure in question. The noise from marine vehicles can be dominated by interaction between the fluid flow and any roughness present on the surface of the vehicle, and this is termed roughness noise. This noise can be detrimental to the performance and efficient operation of marine vehicles, and few options exist to suppress this noise apart from removing the roughness itself. As this is not always feasible if the structure's design depends on the presence of roughness (for example, rivet heads which fasten structural components of the vehicle), other methods of noise control would be valuable.

The noise from large, rotating wind turbines is dominated by interaction between the fluid flow and the sharp trailing edges of the turbine blades, termed trailing edge noise. This noise can travel significant distances from wind turbines and can be a source of annoyance for those living in nearby communities. New methods of noise control would significantly improve the quality of life in these communities and increase the viability and popularity of wind energy.

This work takes inspiration from the anatomical features of silently-flying owls to develop new methods to control both roughness noise and trailing edge noise. Experiments and simulations were carried out to prove the effectiveness of these methods and to gain scientific understanding of the fluid mechanics responsible for noise reduction. The developments described in the present work give engineers new tools for designing future vehicles and wind turbines which operate more quietly and more efficiently.

Acknowledgments

The work presented in this dissertation would not have been possible without support from the Office of Naval Research, the Institute for Critical Technology and Applied Science at Virginia Tech, and Advanced Research Computing at Virginia Tech. Their support of this work is gratefully acknowledged and much appreciated.

I am fortunate to be able to name many people who have earned my sincere thanks and appreciation during my time as a graduate student. I have been gifted their support, both academically and personally, and I would not be where I am today without it.

I would first like to thank my advisor, Dr. William Devenport, for guiding me throughout my graduate career. In addition to the opportunity to conduct the research presented in this dissertation, he has given me the knowledge, skills, and inspiration needed to continue my research career beyond graduate school. I also want to thank my dissertation committee members Dr. W. Nathan Alexander, Dr. Stewart Glegg, and Dr. K. Todd Lowe for their insight and advice which has improved the nature and scope of my research tremendously.

I have had the privilege of working with other researchers including Dr. Nigel Peake, Dr. Conor Daly, and Mr. David Baker at the University of Cambridge, UK, Dr. Justin Jaworski at Lehigh University, and Mr. Mike Marcolini from NASA Langley. Their input has broadened my understanding of my own work, and our collaboration has yielded many interesting findings.

I owe a huge thanks to everyone I have worked with in Lab7 and in the Center for Renewable Energy and Aerodynamic Technology (CREATe). As a new graduate student, the support of Manuj Awasthi, Tim Meyers, Liselle Joseph, and Ken Brown was integral to my success. I would also like to thank Anthony Millican, Neehar Balantrapu, Henry Murray, Jonathan Reardon, David Wisda, Dan Cadel, Nick Molinaro, Christopher Hickling, and everyone else with whom I have worked.

I want to deeply thank my parents, Warren and Susan Clark, for supporting me in everything that I do. My success here at Virginia Tech was built on the foundation they provided to me through endless love and self-sacrifice. Finally, I want to thank my fiancée, Alexandra Egert, for all of the love and support that she has given me throughout our time together.

Thank you everyone!

Ian A. Clark

Contents

List of Figures

List of Tables

Attributions

I have been fortunate to work alongside some extremely talented faculty and students during my graduate studies. In particular, the contributions of a few have made a significant impact on the present work:

Dr. William Devenport is the primary advisor and committee chair for this research. He has provided technical direction throughout these projects and has reviewed all publications included here.

Dr. W. Nathan Alexander is the committee co-chair for this research, and has also provided technical guidance for all work presented here.

Dr. Stewart Glegg is a committee member who provided advice on the analysis of data gathered during experiments.

Dr. Justin Jaworski provided insight into the anatomy of the owl and how these features lead to silent flight. The pictures and analysis presented in Chapter 3 under the section titled "The structure of the owl feather down" were developed jointly by the present author and Dr. Jaworski. In addition, Dr. Jaworski contributed advice for and insight into the measurements performed during experiments.

Dr. Conor Daly and Dr. Nigel Peake developed the model of surface pressure reduction presented in Chapter 3 under the section titled "The mixing layer instability as a model of surface pressure reduction." The model was developed using the experimental results produced and presented by the author earlier in Chapter 3, but this section and all figures introduced therein are nonetheless attributed entirely to Dr. Daly and Dr. Peake. In addition, they contributed advice for and insight into the data gathered during experiments.

Chapter 1

Introduction

The presence of noise induced by fluid flow over engineering structures can lead to negative consequences ranging from simple annoyance to economic losses to tactical disadvantages depending on the particular situation in which it occurs. In virtually any case, reduction of aerodynamic/hydrodynamic noise is advantageous. Two notable sources of noise are rough surfaces and the trailing edges of wings. These sources of noise are common on two different types of engineering structures.

Roughness noise is a primary component of the noise emitted by structures with high surface-area-to-perimeter ratios, such as marine vehicles. Roughness on the surface of this type of vehicle may be present due to surface finish, fasteners (rivets, for example), or to the growth of marine organisms which attach themselves to the surface. Flow over this roughness generates noise which can disadvantageous.

Trailing edge noise is a primary component of the noise generated by large wind turbines. This noise is an annoyance to those living in nearby communities. As a result, government regulations set standards for turbine noise emissions. To comply with these regulations, wind turbines are designed to run quietly and to reduce trailing edge noise as much as possible, but still may exceed the maximum allowable noise level during certain meteorological conditions. During these times, the on-board control system configures the blades to run less efficiently and therefore more slowly. Since trailing edge noise is primarily a function of flow speed over the blade, this reduces noise. It also directly reduces the amount of power generated by the wind turbine. Since the conditions corresponding to maximum noise also correspond to maximum power generation (higher wind speeds), this leads directly to a significant economic loss. Wind turbine designers and manufacturers have dedicated substantial sums of money for research into trailing edge noise control technologies for precisely this reason.

The present dissertation describes the development and testing of two noise control technologies, each of which target one of the two noise sources just described. In the first part, a new method of roughness noise control is described which features the suspension of sparse fabric canopies above the roughness. This setup was inspired by the anatomy of owls' feathers which feature fine hairs on their surface which form a sort of canopy above the feather structure itself. The method is tested experimentally and is found to be capable of not only reducing the total far-field noise created by surface roughness but also reducing the magnitude of unsteady surface pressure by as much as three orders of magnitude in some cases.

The second part of this dissertation describes a new method of trailing edge noise control which treats the incoming boundary layer (the source of trailing edge noise) before it reaches the scattering trailing edge through the use of "finlets". This methodology is different from existing trailing edge noise control technologies which seek to modify the scattering edge itself. The development of the finlets was inspired by the results presented in the first portion of the dissertation. It was thought that a similar geometry to the suspended canopies would lead to a similar reduction of surface pressure fluctuation magnitude at the trailing edge, thereby reducing noise. The new methodology was tested experimentally at high Reynolds number conditions on a typical wind turbine airfoil and was found to reduce trailing edge noise by up to 10 dB at some conditions.

The third portion of the dissertation seeks to gain further understanding of the finlets and the particular fluid mechanics behind the noise reduction achieved with their use. This involved a two-part study consisting of a flow simulation replicating the flow conditions and geometry of a wind tunnel test with finlets applied to a wind turbine airfoil, along with a companion experiment which featured finlets on the same airfoil with additional instrumentation not used in the previous experiment (detailed in the second part of the dissertation). Specifically, microphones were installed in the airfoil model itself, which allowed for direct measurement of the influence of the finlets on both the magnitude and correlation length scale of surface pressure fluctuations. These measurements were analyzed using previously-developed trailing edge noise theory as a framework for understanding how noise reduction is achieved.

The fourth portion of the dissertation describes an experiment performed to determine whether the finlet technology would effectively reduce noise from a rotating system, namely a marine propeller. Phased microphone array measurements were taken of the noise emitted by a marine propeller in a wind tunnel with and without finlets applied. Velocity measurements were taken just downstream of the propeller to analyze the fluid dynamic effects of the finlets. Empirical relationships documented in the literature are used to predict the characteristics of noise from this setup. These predictions are then used as an analysis tool to draw conclusions about the usefulness of finlets, not only for use on rotating systems but also for use on structures with blunt trailing edges.

1.1 Structure and Contents

This dissertation is divided into five chapters.

Chapter 1 provides a general introduction and overview of the dissertation's content and organization.

Chapter 2 is comprised of a literature review outlining previous work related to roughness noise, the anatomy of the owl, trailing edge noise, phased microphone arrays, and noise control technologies.

Chapter 3 is the first manuscript, "Bio-inspired canopies for the reduction of roughness noise," published in the Journal of Sound and Vibration (2016 385:33-54, DOI 10.1016/ j.jsv.2016.08.027). This paper begins with a visual study and review of the anatomy of owls' feathers and the characterization of their downy coating. Next, a series of analogous canopies consisting of fabric with high open-area ratios are selected for experimentation. Results are presented, analyzed with respect to unique geometric parameters of each canopy, and used for the development of optimized canopies featuring only streamwise-aligned fibers. Use of these canopies is found to reduce the noise generated by the underlying roughness with no additional noise measured at any frequency.

Chapter 4 is the second manuscript, "Bioinspired Trailing-Edge Noise Control," published in the American Institute of Aeronautics and Astronautics (AIAA) Journal (2016, DOI 10.2514/1.J055243). This paper outlines the development and testing of twenty configurations of "finlets", for which the overall design was based on the first manuscript presented in Chapter 3. Results for this study primarily consisted of measurements of trailing edge noise produced by a DU96-W180 airfoil with and without finlets in the Virginia Tech Stability Wind Tunnel using a 117-microphone phased array. The effects of geometric parameters such as finlet height, spacing, and thickness are analyzed, and preliminary conclusions are drawn based on this information. The study also featured preliminary measurements of lift and drag. The overall results showed that noise reductions of up to 10 dB were achievable over a wide frequency range, and that the impact on airfoil aerodynamics was minimal.

Chapter 5 is the third manuscript to be submitted to AIAA Journal, titled "Understanding Trailing Edge Noise Control Using Finlets," to be submitted to AIAA Journal. This manuscript outlines a series of follow-on investigations to build understanding of the finlets' noise control mechanism and their influence on the flow near the trailing edge. A representative Reynolds-Averaged Navier-Stokes flow simulation was performed for a DU96-W180 airfoil with and without finlets. Results obtained from the simulation were related to those from a new experiment performed in the Virginia Tech Stability Wind Tunnel which featured surface pressure microphones in the surface of the airfoil near the trailing edge, in addition to improved mean pressure taps over the entirety of the airfoil which allowed for accurate lift measurements with the finlets applied. The flow simulation was validated through comparison to experimental results. Results showed that the suction and pressure side finlets had significantly different effects on their respective flows, leading to slightly different but complementary noise reduction effects. The experimental results were related to a previously-developed theory of trailing edge noise to gain further insight into the function of finlets.

Chapter 6 is the fourth manuscript, consisting of a full-length conference paper to be presented at the 23rd AIAA/CEAS Aeroacoustics Conference in June of 2017. This manuscript outlines an experiment performed in the Virginia Tech Stability Wind Tunnel with the goal of reducing noise from a rotating marine propeller using finlets. Acoustic and flow measurements were obtained for the propeller in untreated and treated configurations. Analysis tools developed in the literature were used to identify the frequency ranges where two sources of

noise were likely to be dominant. The results indicated that the finlets were effective at reducing noise caused by both of these sources, thus validating and increasing the usefulness of the finlets for a wide variety of applications.

The formatting of this dissertation differs among chapters because of the inclusion of the published papers and manuscripts. Chapter 3 follows the published format of Journal of Sound and Vibration, Chapter 4 follows the published format of AIAA Journal. Chapters 5 and 6 were developed as manuscripts to be submitted to AIAA Journal and to the 23rd AIAA/CEAS Aeroacoustics Conference Proceedings, respectively, but were modified to follow the formatting conventions set by the remainder of this document.

1.2 Achievements

Key results and developments from the present research include:

- Development and demonstration of the only known (at the time of this writing) method for the reduction of flow-generated noise from existing surface roughness, which involves the use of suspended fabric canopies.
- Determination of the effects of canopy geometric parameters on the emitted far-field noise and pressure fluctuations on the underlying surface.
- Development and demonstration of a novel trailing edge noise control methodology which modifies the boundary layer turbulence approaching the trailing edge through the use of small fins ("finlets") placed at the trailing edge of an airfoil.
- Analysis of the effects of geometric parameters of the finlets (height, spacing, thickness, etc.) on trailing edge noise reduction.
- Simulation of the flow over a DU96-W180 airfoil with and without finlets. The simulation gives results that yield insight into the fluid mechanics of finlets and their precise influence on the flow near the trailing edge.
- Detailed experimental measurements of the surface pressure fluctuations near the trailing edge of a DU96-W180 airfoil at high Reynolds number with and without finlets. The results yield further insight into the effects of finlets on boundary layer turbulence as it approaches the trailing edge.
- Analysis of the effects of finlets on trailing edge noise through the use of previously developed trailing edge noise theory. The results indicate the relative contribution of the finlets' effects on unsteady surface pressure magnitude and spanwise correlation length scale in reducing overall noise emitted by the trailing edge.

- Experimental measurements of noise from a rotating marine propeller with and without finlets applied. The results demonstrate the noise reduction capability of finlets on a rotating system, and complementary measurements of the flow downstream of the propeller allow for additional analysis.
- Predictions of the noise from the rotating propeller using empirical methods documented in the literature reveal the likelihood of noise due to the bluntness of the propeller's trailing edge. Analysis of the acoustic data shows the finlets to be effective at reducing this noise, further increasing the variety of applications which could benefit from their use.

Chapter 2

Background and Literature Review

2.1 Roughness Noise

Many experimental and theoretical studies have been undertaken to understand the nature of roughness noise, and the impact of roughness on underlying surface pressure fluctuations. Because the present work does not seek to advance the fundamental understanding of roughness noise and instead proposes a method for reduction, this review is limited to several recent studies which yield an understanding of the sources of roughness noise in the context of the present work.

Early experimental studies [1, 2, 3] showed that rough-wall boundary layer noise is of dipole order with far-field noise levels that scale with the sixth power of velocity. Hersh [3] suggested that the noise source could be the unsteady drag force on the individual roughness elements, which would lead to a streamwise-aligned dipole source. One of the earliest theoretical developments was mas made by Howe [4] who developed a model for the scattering of fluctuating Reynolds stresses in the boundary layer above hemispherical roughness elements. However, several limitations were noted in this model, namely that the roughness elements do not influence the wall pressure spectrum. Howe [5] later used his theory with Chase's [6] wall pressure spectrum model to generate a far-field noise spectrum which was shown to scale in the same way as Hersh's [3] data.

Understanding of roughness noise advanced significantly with the work of Grissom *et al.* [7] who performed acoustic measurements in the Virginia Tech Anechoic Wall-Jet Wind Tunnel. The low background levels of this tunnel permitted accurate measurements of roughness noise. A follow-on study by Devenport *et al.* [8] measured far-field acoustics as well as the surface pressure spectrum. They found that the far-field sound was proportional to the surface pressure spectrum by a factor of $(k_0 h)^2$, where k_0 is the acoustic wavenumber and h is the root-mean-square roughness height.

In 2009, Glegg and Devenport [9] developed a "Unified Theory of Roughness Noise," which encompasses all types of rough surfaces (as opposed to the hemispherical bosses of Howe [4]) by accounting for the specific geometry of the surface. Their theory is based on Lighthill's [10, 11] equation reformulated by Goldstein [12], which is then simplified for the specific problem of flow past a rigid surface at low Mach number. They show that the far-field noise

can be expressed as a convolution integral of the wavenumber transform of the surface slope and the surface pressure wavenumber-frequency spectrum. This convolution integral is given as:

$$(\rho'(\boldsymbol{x},\omega)c_\infty^2)_{dipole} \approx \frac{-ik_0 e^{ik_0|\boldsymbol{x}|}}{2\pi|\boldsymbol{x}|}\int_\kappa p_s(\kappa_1,\kappa_3,\omega)\left[\left(\frac{x_1\zeta^{(1)}}{|\boldsymbol{x}|}+\frac{x_3\zeta^{(3)}}{|\boldsymbol{x}|}\right)-ik_0h\zeta^{(2)}\right](2\pi)^2 d\kappa_1 d\kappa_3 \tag{2.1}$$

Here, the left hand side of the equation represents the acoustic pressure fluctuations due to the dipole source, $\boldsymbol{x}$ is the observer position, ω is angular frequency, c_∞ is the free-stream speed of sound, k_0 is the acoustic wavenumber, p_s is the surface pressure wavenumber-frequency spectrum, and, for acoustically compact scales, κ_1 and κ_3 are wavenumber components in the y_1 (streamwise) and y_3 (spanwise) directions. $\zeta^{(1)}$ and $\zeta^{(3)}$ are the wavenumber transforms of the surface slope, given as:

$$\zeta^{(j)}(\kappa_1,\kappa_3) = \frac{1}{(2\pi)^2}\int_\Sigma \frac{\partial\xi}{\partial y_j}e^{i(\kappa_1 y_1+i\kappa_3 y_3)}d\Sigma, j=1,3 \tag{2.2}$$

$\zeta^{(2)}$ is the wavenumber transform of the surface height, give as:

$$\zeta^{(2)}(\kappa_1,\kappa_3) = \frac{1}{(2\pi)^2 h}\int_\Sigma \xi e^{i(\kappa_1 y_1+i\kappa_3 y_3)}d\Sigma \tag{2.3}$$

Here, h is the root-mean-square roughness height, ζ is the rough surface height in the y_2 direction, and Σ is the area of the rough surface projected onto the y_1y_3 plane.

The theory was tested in 2010 when Devenport *et al.* [13] used noise measurements of a well-defined surface of elliptical ridges to obtain high-resolution results for the wall pressure wavenumber-frequency spectrum which would have required conventional transducer spacing of no more than 0.63 mm. These results qualitatively agreed with those of Corcos [14] and Chase [6]. This conclusively links the surface pressure spectrum to the far-field noise, and suggests a possible method for noise reduction wherein the magnitude of the surface pressure spectrum is simply reduced, leading directly to a decrease in the far-field noise.

2.2 The Structure of Owls' Wings

Owls have long been known to fly virtually silently. Their hunting strategy is based entirely around stealth, flying silently to avoid detection by their prey until it is too late for the prey to escape. This is in contrast with other birds of prey (such as hawks, eagles, etc.) which utilize high speed flight to ambush prey. Mice and other prey have exceptional hearing

through the frequency range between 2-20 kHz [15], and owls have therefore evolved to fly silently above 2 kHz.

The earliest investigations into the owl's silent flight was presented by Graham [16], who identified three unique features of owls' feathers:

- A comb of evenly-spaced bristles along the wing leading edge.
- A compliant and porous fringe of feathers at the trailing edge.
- A velvety down material distributed over the upper wing surface

The leading and trailing edge features of the wing were believed to treat the flow directly, but Graham hypothesized that the velvety down material was meant primarily to muffle the rustling of feathers as the owl moved its wings. He supposed that the velvety down located in areas not involved with feather movement might act as a sound absorber or may act to slow the airflow in the boundary layer of the wing. Notably, Graham [16] mentions several species of owls which feed on fish and observes that these owls do not possess the three features listed above, presumably because stealth is no longer necessary when hunting water-dwelling prey.

Other researchers have investigated these three features of owls' feathers. Kroeger, Gruschka, and Helvey [17] found that owls produce significant low-frequency noise, which is unsurprising given common prey's poor hearing at low frequencies. Kroeger *et al.* focused particular attention on the leading edge bristles and found that these bristles acted as vortex generators which allowed the flow to remain attached to the wing at up to thirty degrees angle of attack. Klan *et al.* [18, 19] developed detailed experimental models for owls' wings and tested velvety surfaces, but their studies were focused primarily on the aerodynamic effects of this feature, namely the tendency for the flow to remain attached to the wing at low speeds and high angles of attack. They point out that lower flight speeds correspond directly to lower noise levels, meaning features which allow the owl to fly slowly would also assist in their silent flight. Bachmann *et al.* [20] performed detailed measurements of the owl's downy coating, but simply repeated the speculation that they reduce rubbing noise between the feathers while possibly altering the flow in the boundary layer.

The most compelling argument for a noise reduction mechanism of the downy coating was given by Lilley [15], who analyzed the noise-reducing characteristics of the leading and trailing edge features of the owls' wings and found that the owl would still produce significant aerodynamic noise above 2 kHz. He argues that the velvety coating, with the small diameter and compliant nature of the fibers, must modify the turbulence in the boundary layer as it approaches the trailing edge, damping the small scale eddies which cause high-frequency noise. In this way, turbulent eddies (and therefore surface pressure fluctuations) would be significantly dampened at frequencies lower than the frequency at which viscous dissipation would normally take effect. This opens the possibility of replicating this type of structure

for the reduction of roughness noise, if pressure fluctuations can be reduced on the rough surface itself.

2.3 Early Trailing Edge Noise Theory

Ffowcs Williams and Hall [21] were the first to consider the case of trailing edge noise in the context of Lighthill's [10, 11] theory. Prior to this work, the only considerations were to situations where the velocity and length scales of the problem were set only by the turbulence in the flow. In this case, the intensity of the noise generated by free turbulence increases with the eighth power of velocity, while that induced by unsteady pressure on a surface increases with the sixth power of velocity. However, the presence of a sharp trailing edge introduces a new scale to the problem, with the sharp edge scattering unsteady pressure. Therefore, the field around the edge would be governed by diffraction effects. Ffowcs Williams and Hall determined that the edge scattered field is proportional in intensity to the fifth power of velocity, and would therefore dominate at low Mach numbers.

Ffowcs Williams and Hall [21] begin by writing Lighthill's equation as an inhomogeneous Helmholtz equation using the Fourier transforms of each term:

$$\nabla^2 p^* + k_0^2 p^* = -\left[\frac{\partial \rho v_i v_j}{\partial y_i \partial y_j}\right]^* \tag{2.4}$$

Here, p is the pressure in the fluid, ρ is the fluid density, and v represents the fluid velocity. The superscript $*$ represents the general Fourier transform of a quantity. The solution of equation (2.4) is written down in terms of a Green's function whose normal derivative vanishes on the half-plane:

$$p^*(\boldsymbol{x}, \omega) = \frac{1}{4\pi} \int \left(\frac{\partial^2 \rho v_i v_j}{\partial y_i \partial y_j}\right)^* G dV(\boldsymbol{y}) + \frac{1}{4\pi} \int \frac{\partial p^*}{\partial n} G dS \tag{2.5}$$

where

$$(\nabla^2 + k^2) G = -4\pi \delta(\boldsymbol{x} - \boldsymbol{y}) \tag{2.6}$$

$$\frac{\partial G}{\partial n} = 0 \text{ on the half-plane.} \tag{2.7}$$

Through some simplification and far-field approximations, Ffowcs Williams and Hall find that longitudinal quadrupoles aligned parallel with the trailing edge are not enhanced by the edge. Also, the sound at $\theta = \pi$, which corresponds to the downstream direction, is exactly the same as sound from free turbulence. Ffowcs Williams and Hall investigated the scattering effects of eddies which are various distances from the edge in terms of eddy size. It is found that scattering by the edge is most intense when the inequality $2kr_0 \ll 1$ is satisfied,

where k is the acoustic wavenumber and r_0 is the distance from the center of an eddy to the edge.

A result for the maximum intensity is presented as:

$$I_{max} \approx \frac{\rho k U^4 V^2 \alpha^2}{\pi^3 c_\infty R^2 \delta^3} \tag{2.8}$$

Here, U is a typical flow velocity, V is the volume of the eddy, α is the normalized turbulence intensity, R is the separation of the source point and the field point (observer location), and 2δ is the diameter of the cylinder representing the eddy. It is noted that the typical frequency of the turbulent source is of order $U/2\delta$ so k is of the order $\pi U/c\delta$. Therefore the scattered intensity increases with the fifth power of fluid velocity.

This result indicates some possible methods for noise reduction. The maximum intensity of the emitted trailing edge noise will be reduced if the overall volume of eddies are reduced, or if the turbulence intensity of the flow is lowered. In addition, due to the result indicating the scattering is most intense when $2kr_0 \ll 1$, it can be seen that scattering could be reduced if the eddies were pushed further from the edge.

2.4 Trailing Edge Noise Related to Surface Pressure

The work of Ffowcs Williams and Hall [21] used Lighthill's theory to good effect to analyze the dependence of trailing edge noise on turbulent velocity fluctuations in terms of turbulent eddy parameters. However, the limitation of this formulation is its dependence on the Lighthill tensor, $T_{ij} = \rho v_i v_j$, which represents the acoustic sources in the fluid domain. Although the tensor gives exactly the information needed for acoustic calculations, the quantity itself is not feasibly measurable, which makes it difficult for experimental work to support the theory. Therefore, researchers looked to take a different track for further theory development which would be of practical use to experimenters and engineers.

The first such development was made by David Chase in 1972 [22]. He related the scattered far-field noise to the wavevector-frequency spectral density of the hydrodynamic pressure fluctuations near the edge. His formulation focused on a plate embedded in a turbulent jet, as opposed to a free-stream of a vehicle in flight. The advantage of such a model was that the pressure fluctuation statistics on the surface of a plate or airfoil could be measured using a microphone embedded in the surface, and indeed significant work in this area had already been accomplished by this time (see a review by Willmarth [23]). The surface pressure fluctuations are an integral quantity of the velocity fluctuations (Reynolds stresses) in the flow, which circumvented the measurement problem of Lighthill's stress tensor. The incompressible relationship between velocity and pressure fluctuations can be stated using the pressure Poisson's equation, obtained by taking the divergence of the momentum equation

(see Batchelor [24] or Willmarth [23]):

$$\frac{1}{\rho}\nabla^2 p = -\frac{\partial^2 u_i u_j}{\partial x_i \partial x_j} \tag{2.9}$$

Chandiramani [25] considered a similar formulation in 1974 by modeling the diffraction of an evanescent wave traveling over the trailing edge, which more closely resembles the pressure fluctuations associated with a turbulent boundary layer. Chase [26] used this evanescent wave formulation in 1975 while using a different model for the near-field pressure fluctuations. Again, however, these works were focused on the noise from a plate embedded in a turbulent jet.

The relation between turbulent pressure fluctuations and far-field noise reached maturity with Amiet's [27, 28] work, which modeled the noise from the edge of a half-plane in a free-stream flow. The far-field noise is given as:

$$S_{pp}(x, 0, z, \omega) = \left(\frac{\omega b z}{2\pi c_\infty \sigma^2}\right)^2 l_y(\omega) d |\mathscr{L}|^2 S_{qq}(\omega, 0) \tag{2.10}$$

In this equation, ω is angular frequency, b is the airfoil semichord, x is position in the streamwise direction, z is position in the vertical direction, c_∞ is the sound speed, $\sigma^2 = x^2 + \beta^2 z^2$, $\beta = 1 - M^2$, d is the airfoil semispan, $\mathscr{L}$ is the airfoil lift response function, $S_{qq}(\omega, 0)$ is the surface pressure power spectral density at a point, and $l_y(\omega)$ is the spanwise correlation length scale of the turbulent pressure fluctuations, given as:

$$l_y(\omega) = \frac{1}{S_{qq}(\omega, 0)} \int_0^\infty S_{qq}(\omega, y) dy \tag{2.11}$$

The spanwise correlation length scale can be measured using a spanwise array of microphones embedded in the surface near the trailing edge, but it can also be approximated as:

$$l_y(\omega) \approx 2.1 U_c / \omega \tag{2.12}$$

Here, U_c is convective velocity of turbulent pressure fluctuations, which is commonly approximated as 60-80% of the free-stream velocity, although in reality is somewhat frequency-dependent.

The results of Amiet's theory indicate that reducing the magnitude and spanwise correlation length scale of turbulent pressure fluctuations can lead directly to reductions in far-field noise. In addition, reducing convection velocity may indirectly affect the far-field noise by reducing the spanwise correlation length scale.

2.5 Early Trailing Edge Noise Experiments

With the developments of theory relating surface pressure and far-field noise, the theoretical field of trailing edge noise was now mature enough for significant, comprehensive experiments to be undertaken to verify some of the claims of Amiet and others.

Brooks and Hodgson [29] performed an extensive set of experiments on trailing edge noise in the quiet flow facility at NASA Langley. They used a 2 ft chord NACA 0012 mounted between endplates in an open jet with both far-field microphones and embedded Kulite surface pressure sensors. The authors studied several different trailing edges which could be applied to the airfoil. The edges ranged in thickness from 2.5 mm to 0.0 mm (sharp). Kulite sensors with a pinhole diameter of 0.34 mm were mounted in the airfoil. The closest sensor to the trailing edge was placed 2.54 mm upstream of the edge. A streamwise array was embedded with the farthest upstream sensor placed 206.2 mm upstream of the edge. A spanwise array was also embedded with all sensors 2.54 mm upstream of the edge, extending approximately 0.2 m in each direction along the trailing edge. The distances used here refer to the case when no trailing edge attachment was used (so the trailing edge had a thickness of 2.5 mm. Attaching trailing edge extensions increased the sensor distance from the edge. Eight half-inch B&K microphones were used around the airfoil to measure far-field sound.

The authors' discussion of results begins with the surface pressure fluctuations, specifically the power spectral density and coherence. The power spectral density of pressure fluctuations should scale with boundary layer thickness, and the characteristic frequency should scale with the inverse of this thickness, as the boundary layer sets the characteristic length scale of the flow. The spectra mostly collapse when normalized using the dynamic pressure and the approximated displacement thickness δ^*. However, a better collapse is observed for δ^* raised to the 1.2 power, which suggests that δ^* increases more rapidly for an adverse pressure gradient than for a flat plate. A notable result observed by Brooks and Hodgson is a spectral "hump" that occurs in the surface pressure data very close to the trailing edge. This is due to coherent vortex shedding off of the trailing edge of the airfoil.

Brooks and Hodgson's far-field noise results were obtained by using a special method of processing termed the "coherent output power" method. Essentially, instead of using only the autospectrum from each microphone, they used the cross-spectrum from a pair of microphones placed at similar locations on each side of the airfoil. Since the airfoil noise is expected to be emitted from the trailing edge identically on each side of the airfoil, albeit with a 180 degree phase difference, the cross-spectral method allows the background, facility, and parasitic noise to be filtered out, leaving only the trailing edge noise. This leads to a much lower uncertainty in the results, and allows for better comparison to theoretical developments. The agreement between predictions performed for this test and the experimental results were satisfactory, particularly when using the measured surface pressure values, providing the first evidence supporting the earlier theoretical developments.

A few years later in 1989, Brooks, Pope, and Marcolini [30] published a NASA reference

publication which identified five sources of airfoil noise: Turbulent-Boundary-Layer-Trailing-Edge Noise (the primary subject of this review), Separation-Stall Noise, Laminar-Boundary-Layer-Vortex-Shedding Noise, Tip Vortex Formation Noise, and Trailing-Edge-Bluntness-Vortex-Shedding Noise. The authors investigated all of these sources in detail through a series of experiments in an open-jet anechoic facility. In particular, they performed hot-wire velocity measurements near the trailing edge of the airfoil. They then use the boundary layer parameters to build a model of the noise from the trailing edge using only flow measurements.

For acoustic measurements, Brooks, Pope, and Marcolini used a similar method as that of Brooks and Hodgson by examining the cross-spectra of two microphones to focus on the noise of interest. In addition, they are able to identify leading edge noise and trailing edge noise as peaks on the cross-correlation plot between two microphones. They present noise spectra from airfoils of numerous chords and angles of attack along with associated predictions for each case.

A major result of Brooks *et al.* is the scaling law for trailing edge noise, given here for zero angle of attack as:

$$\text{Scaled SPL}_{1/3} = \text{SPL}_{1/3} - 10log\left(M^5 \frac{\delta_0^* L}{r_e^2}\right) \tag{2.13}$$

Here, $\text{SPL}_{1/3}$ is the one-third octave sound pressure level, M is Mach number, δ_0^* is displacement thickness at the trailing edge, L is spanwise extent of the airfoil wetted by the flow, and r_e is the retarded observer position. A similar scaling can be used to normalize results at different angles of attack, the only difference being the use of the suction side displacement thickness. The scaling laws collapsed the data well, although it is important to note that Brooks, Pope, and Marcolini showed that the scaling worked best for the 30.48 cm airfoil, while the frequency scaling for airfoils of smaller chord did not display the same level of collapse, especially for different angles of attack. This could be due to lower Reynolds number effects and the rise of other sources of noise (boundary layer separation, etc.). The peak of the trailing edge noise occurs at a nondimensionalized frequency $St = f\delta^*/U$ of between 0.05 and 0.1. The authors lay out a method of calculating trailing edge noise based around a semi-empirical model developed from the data presented in the report.

2.6 Phased Microphone Arrays

Experimental work on trailing edge noise has been aided by a number of advancements in measurement techniques. In particular, the developments of microphone phased arrays and aeroacoustic wind tunnels has allowed for higher fidelity measurements than were previously possible. The use of microphone phased arrays can be viewed as an extension to the coherent output power method of Brooks and Hodgson [29]. Essentially, a large number of microphones is used to identify individual sound sources over a large area. In this way, one

can focus on the trailing edge of airfoil and consider only the sound from this region in the analysis. As this type of array processing is used to produce a major portion of the results in the present dissertation, this will be examined in more detail.

In general, phased microphone arrays seek to identify the locations of noise sources in space. Most processing algorithms assume that the noise sources of interest are of monopole type, meaning their strength is constant with respect to propagation direction. In the simplest case of an isolated noise source in quiescent air, the propagation time from the noise source to each microphone is dependent on the speed of sound and the distance from the source point to each microphone. To locate a noise source, a "scanning plane," or a grid of points over which to search for noise sources is first defined. Then, for each point in the scanning plane, the signals from each microphone are appropriately delayed by accounting for the distance in propagation time between that point in the scanning plane and the microphone. The delayed microphone signals are then summed to obtain a relative noise level for each point. This methodology is termed "delay-and-sum beamforming" for this reason, but is often also referred to as "conventional beamforming."

In practice, it is often desirable to obtain frequency-dependent source levels from the beamform maps, and the beamforming technique is therefore applied in the frequency domain. This process will now be outlined in detail. Post-processing of the raw time series from each microphone begins with taking the Fast Fourier Transform (FFT). The time series is broken up into records (with 50% overlap and using a Hanning window in the present work), and the FFT is performed for each record. A Cross-Spectral Matrix (CSM) is generated by combining the FFT's from pairs of microphones i and j to form each element of the CSM as follows [31]:

$$G_{ij}(f) = \frac{1}{NW_s} \sum_{k=1}^{N} \left[X_{ik}^{*}(f) X_{jk}(f) \right] \tag{2.14}$$

Here, N represents the total number of records obtained from each time series, W_s is the data-window weighting constant, and X is the FFT data record. The superscript $*$ represents the complex conjugate. Next, a "steering matrix" is needed which relates the geometry of the array to the scanning grid to appropriately delay, or phase-shift, the elements of the CSM. Many options are available for the development of the steering matrix, particularly when considering more advanced beamforming techniques, but the simplest choice used for conventional beamforming is [32]:

$$\hat{e} = col[e_1 \quad e_2 \quad ... \quad e_{m_0}] \tag{2.15}$$

Here, the total number of microphones is m_0. Each component of the matrix $\hat{e}$ for each microphone m is [32]:

$$e_m = a_m \frac{r_m}{r_c} e^{j2\pi f \tau_m} \tag{2.16}$$

$$2\pi f \tau_m = (\vec{k} \cdot \vec{x}_m) + 2\pi f \Delta t_{m,shear} \tag{2.17}$$

In these equations, r_m is the distance from the grid point to the microphone, r_c is the distance from the grid point to the center of the microphone array, τ_m is the propagation time from the grid point to the microphone, $\vec{k}$ is the acoustic wave vector, and $\vec{x}_m$ is the distance vector from the grid point to the microphone. In the absence of a flow shear layer between the microphone array and the scanning point, the second term in equation 2.17 is zero. If a shear layer is present, the convection and refraction of the sound must be taken into account, as this will alter the propagation time between the grid point and each microphone. The corrections are contained in the term $\Delta t_{m,shear}$ in equation 2.17 for the additional propagation time, as well as in the term a_m in equation 2.16 for the amplitude correction. A method for calculating the shear layer correction is given by Amiet [33] and is verified and refined by Bahr *et al.* [34] to a form suitable for implementation into a beamforming algorithm.

To perform the final beamforming and obtain source strengths at each point in the scanning grid, and matrix is calculated as [31]:

$$P(\hat{e}) = \frac{\hat{e}^T G \hat{e}}{m_0^2} \tag{2.18}$$

Here, the superscript T represents the complex transpose of the matrix. From the matrix P, the diagonal elements are taken which represent the mean-squared-pressure at each scanning grid point.

Diagonal Removal (DR) is often used in situations where the signal-to-noise ratio of the microphone measurements is low, such as when the array is located in the wall of a closed-test-section wind tunnel and thus exposed to near-field pressure fluctuations in the wall's boundary layer. Diagonal Removal refers to the removal of diagonal elements from the CSM which has the effect of removing the influence of any noise which is uncorrelated between pairs of microphones from the resulting beamform maps [35]. The resulting beamforming equation is thus [32]:

$$P(\hat{e}) = \frac{\hat{e}^T G_{diag=0} \hat{e}}{m_0^2 - m_0} \tag{2.19}$$

Although this beamforming process can adequately identify regions of noise, the results are a convolution of the true noise source distribution and the response function of the array itself. The response function is determined by the size of the array along with the number and arrangement of microphones in the array, and has the effect of "blurring" the noise

sources in the beamform maps. Deconvolution techniques have been developed in order to remove the influence of the array response function, resulting in acoustic maps which display precise noise source locations. The Deconvolution Approach for the Mapping of Acoustic Sources (DAMAS) algorithm developed by Brooks and Humphreys [32] was one of the earliest methods developed specifically for use in aeroacoustic measurements. The algorithm reformulates the beamforming algorithm as an inverse problem to solve for the true acoustic source distribution. This is done by modeling the response of the array to a single noise source at each grid location (the point spread function, or PSF), inverting the resulting matrix, and multiplying by the results obtained through conventional beamforming. However, the matrix to be inverted is found to be of rank less than one, meaning many solutions to the resulting set of linear equations exist. The true physical solution is found by solving the linear equations through an iterative procedure which enforces the positivity of the acoustic sources at all grid points throughout the procedure.

The "CLEAN" deconvolution method was originally developed for use in radio astronomy [36] and has been adapted for use in aeroacoustic measurements. The algorithm functions by searching for the peak location in the "dirty" map (the map obtained through conventional beamforming), subtracting the scaled PSF from this map, and replacing it with an idealized source. This is done in an iterative procedure until some stopping condition is reached.

Both the DAMAS and CLEAN algorithms assume that the noise sources to be found are compact, incoherent sources. However, these methods have been extended for use with spatially-coherent sources, and these extensions are termed DAMAS-C [37] and CLEAN-SC [38]. Instead of utilizing the point spread function to determine how "blurred" a source is, the coherence between points in the acoustic source map is used to determine the spatial extent of a source.

As a final discussion point, it is useful to consider the methodology for generating noise spectra from beamform maps. One limitation of beamform maps is their constraint to a single frequency. If one is interested in the behavior of a source at a particular location across many frequencies, it is inconvenient to examine the many beamform maps associated with that frequency. To generate a noise spectra for a given region within the beamform maps, it is possible to "integrate" the beamform maps over this region [35]. This method assumes incoherence of the noise sources, and as such assumes no interference effects from these sources. The levels at each grid point within the integration region of the acoustic source map are summed, and this summation is then divided by the point spread function in order to account for the artificial "blurring" of the acoustic sources in the map. This integration can be performed over all frequencies to generate a single noise spectrum.

In order to reject any sidelobes which may be present in the integration region from sources outside (or inside) the region, a threshold is normally defined as being some level (5 dB for the present work) below the peak level in the integration region. Levels are then only summed if they are above this threshold.

As mentioned above, phased arrays have been utilized to great effect in aeroacoustic mea-

surements. Hutcheson and Brooks [39] measured noise from both a rod and airfoil using two different methods. The first measurement used the coherent output power method of Brooks and Hodgson [29] while the second used a directional microphone array consisting of 33 microphones in four concentric rings. They found that the results from both methods were generally consistent, establishing the phased array as a viable method for measurement of trailing edge noise. Their results suggested that the array can more accurately distinguish between leading and trailing edge noise, which further increases its value as a research and diagnostic tool. The same authors published a study [40] several years later which used these same tools to quantify the effects of angle of attack and velocity on trailing edge noise.

In 2007, Oerlemans *et al.* [41] published a study in which a 148-microphone phased array was used in the field to measure the noise of a 58-m diameter wind turbine in operation. The array was placed on the ground upwind of the wind turbine. The results indicated that the majority of the noise from a wind turbine is produced by the outer portion of the blade, near the tip, when the blade is sweeping towards the observer.

In addition to phased arrays, a new method for constructing wind tunnels test sections with tensioned Kevlar walls [42] has improved the quality of aeroacoustic measurements. These tunnels contain the flow in the test section with acoustically-transparent Kevlar leading to reduced issues with flow deflection and eliminating the parasitic noise from the nozzle and jet catcher of a traditional open-jet acoustic wind tunnel. Microphone instrumentation can be placed behind the Kevlar such that flow noise is reduced, and appropriate corrections can be made to account for the presence of the Kevlar. Devenport *et al.* [43] used the Virginia Tech Stability Wind Tunnel along with a 63-microphone phased array to test a series of wind turbine airfoils. Results were compared to those of Brooks *et al.* [30] and were found to be in good agreement, validating the wind tunnel for use in aeroacoustic tests.

2.7 Noise Reducing Technologies

Existing methods of trailing edge noise reduction focus on reducing the discontinuity at the trailing edge so that the edge scattering mechanism is less efficient. One of the most widely used devices for trailing edge noise reduction is trailing edge serrations. Serrations were first analyzed theoretically by Howe [44]. His theory was based around the premise that the serrations caused an effective reduction in span responsible for noise generation. By orienting the serrations such that the edge was more closely aligned with the wavenumber vector of dominant turbulent fluctuations, the scattering efficiency of the edge would be reduced. His analysis showed that serrations can have a substantial impact on trailing edge noise particularly when the angle of the serrations relative to the unserrated trailing edge exceeds forty-five degrees. Howe showed that the expected noise reduction is about $10log[1 + (4h/\lambda)^2]$ dB where h is the root-to-tip distance of the serrations, and λ is their spanwise wavelength. He also found that reductions were only achieved for frequencies $\omega h/U \gg 1$, so the dimensions of the serrations should be greater than the boundary layer

thickness at the trailing edge.

Oerlemans *et al.* [45] tested serrations experimentally on a 2.3 MW, 94-m diameter wind turbine in operation. The three-bladed turbine featured one standard baseline (untreated) blade, one blade with an optimized airfoil shape, and one standard blade with serrations. Their results showed that serrations could achieve an average overall sound pressure level reduction of 3.2 dB compared with the standard blade. The optimized airfoil achieved only about 0.5 dB reduction compared to the standard blade. At certain points in the turbine's rotation, where the peak of the noise occurred for the standard blade, the serrated blade reduced the noise level by about 4 dB. However, it was found that the serrations increased high-frequency noise due to the sharp tips of the serrations.

Experimentally measured noise reductions due to serrations, such as those measured by Oerlemans *et al.* [45], have not quite met the expectations set by the theory of Howe [44]. Gruber *et al.* [46] tested over 30 flat-plate sawtooth inserts of different geometries on a NACA6512 airfoil. They found that the serrations caused a noise increase at non-dimensional frequencies $f\delta/U_0$ above 1, and that the noise reduction at lower frequencies was improved for sharper serrations. However, Howe's theory [44] predicted the greatest noise reduction at high frequencies, with less effect on low frequencies. In contrast, Chong *et al.* [47] tested serrations cut into the normal profile of a NACA 0012 airfoil, which left blunt edges at the roots of the serrations. They found that, for a tripped airfoil with no boundary layer instability tonal noise present, the serrations generated additional noise over a narrow frequency band due to the bluntness at the roots, but higher frequency noise was then reduced. As such, the non-flat-plate serrations exhibited much better performance than flat-plate serrations at high frequencies. Moreau and Doolan [48] investigated flat plate serrations using hot-wire anemometry and found that the serrations have a significant influence on the hydrodynamic field near the trailing edge. Therefore, they assert that Howe's [44] assumption that the serrations have no influence on the turbulent field is not valid which explains the lack of agreement between theoretical predictions and the majority of experimental measurements.

A similar concept to serrations, flexible trailing edge brushes have also been investigated experimentally as potential noise reducers. Herr and Dobrzynski [49] placed flexible brushes at the trailing edge of a flat plate in an open jet anechoic wind tunnel. They found that brushes could reduce the measured noise by up to 10 dB, although it is worth noting that a component of the baseline noise was composed of noise due to bluntness of trailing edge, which is a separate source of noise as classified by Brooks, Pope, and Marcolini [30]. One advantage of flexible trailing edge brushes is that they automatically align themselves in the flow direction at the trailing edge, which is identified as a requirement of serrations by Oerlemans *et al.* [45].

One final edge treatment to discuss is porous and elastic, or poroelastic, trailing edges investigated theoretically by Jaworski and Peake [50]. Their work was based around previous work by Crighton and Leppington [51] which showed the velocity dependence of noise from

a trailing edge could be increased to the sixth power if the edge was sufficiently limp, along with the work of Howe [52] which showed porosity could reduce edge noise. Physically, these two features can be thought to serve as a pressure-release mechanism for unsteady pressure fluctuations as they approach the trailing edge. Jaworski and Peake [50] modeled the problem as a semi-infinite poroelastic plate, and analyzed the acoustic response using the Wiener-Hopf technique. The effect of poroelastic trailing edges was found to be significant particularly at low frequencies, whereas at higher frequencies the change in noise level was found to be mostly produced by the elasticity of the edge. The effect of porosity on its own was found to reduce the acoustic dependence on velocity to the sixth power, compared to the fifth power determined by Ffowcs Williams and Hall [21]. Similarly, the effect of elasticity on its own was found to lead to a seventh power dependence.

2.8 Aerodynamic Devices

There currently exist several aerodynamic devices used for modifying the flow over a wing which bear superficial resemblance to the devices developed in the present dissertation. To reinforce the novelty of the current work, these devices will be described here in order to clearly distinguish the differences in both form and function separating the present work from these other devices.

Riblets, investigated by Walsh and Weinstein [53], Bechert *et al.* [54], and others, is inspired by the skin of fast-moving sharks [55] and is intended for drag reduction only. The ribbed surfaces feature small fins which are located entirely within the viscous sublayer of the boundary layer flow. Walsh [56] states that maximum drag reduction was observed with fin heights of $h^+ = 8 - 12$ in law of the wall coordinates, such that $h^+ = \sqrt{C_f/2}(hu_\infty/\nu)$ where C_f is the wall coefficient of friction, h is the riblet height, u_∞ is the free-stream velocity, and ν is kinematic viscosity.

Wing fences consist of large plates placed vertically on aircraft wings. They are placed such that the spanwise flow across a wing is interrupted, thus improving the aerodynamics of the wing and the high-lift characteristics of the aircraft. Williams *et al.* [57] performed a comprehensive test of wing fences on a T-38 Talon and found that the fences produced a discrete streamwise vortex which prevented flow separation near the wingtip at high angle of attack. As a result, the maximum coefficient of lift was increased by 2% as measured during flight tests.

Finally, vortex generators have been used as a method of reducing flow separation at high-lift conditions on numerous aircraft (see Lin [58] for a review). These structures are placed along the surface of the wing at a substantial angle relative to the incoming flow such that flow separates off of the downstream edge of the generator. This small region of separated flow forms a vortex which transports high-energy fluid from the outer boundary layer into the inner region of the boundary layer. This added energy allows the flow to remain attached

to the main wing, thus improving high-lift characteristics and delaying wing stall.

It is noted here that although these structures bear superficial resemblance to the finlets developed in Chapter 4, their scales, intended functions, and effects on the flow are entirely different from those of finlets, which seek to reduce the noise from the trailing edge of a wing by shielding the trailing edge from unsteady pressure fluctuations.

2.9 Summary and Conclusions

This chapter has highlighted some key studies which set the stage for the work presented in this dissertation. The overarching goal of the present work is to develop bio-inspired methods for reducing roughness and trailing edge noise. The primary work for understanding the generation of roughness noise was presented by Glegg and Devenport [9] who established a link between the unsteady pressure at the rough surface to the far-field noise. Similarly, Amiet [27] produced work which related unsteady pressure near the trailing edge to far-field noise. By considering the anatomy of owls' feathers, the present work mimics the downy coating of the feathers which was described by Lilley [15] as playing a key role in the silent flight of the owl by damping the small scale turbulence in the flow over an owl's wing, thereby reducing the pressure fluctuations at the surface. This methodology separates the present work from previous noise-reducing technologies which seek to modify the scattering geometry while not altering the turbulence in the boundary layer. Phased microphone arrays, along with some of the associated data processing algorithms, will be used in the present work to evaluate some of the noise-control devices developed here.

References

[1] Skudrzyk, E. J. and Haddle, G. P., "Noise production in a turbulent boundary layer by smooth and rough surfaces," *The Journal of the Acoustical Society of America*, Vol. 32, No. 1, 1960, pp. 19–34.

[2] Chanaud, R. C., "Experimental study of aerodynamic sound from a rotating disk," *The Journal of the Acoustical Society of America*, Vol. 45, No. 2, 1969, pp. 392–397.

[3] Hersh, A., "Experimental investigation of surface roughness generated flow noise," *8th AIAA Aeroacoustics Conference*, American Institute of Aeronautics and Astronautics, Atlanta, GA, apr 1983.

[4] Howe, M. S., "On the Generation of Sound by Turbulent Boundary Layer Flow Over a Rough Wall," *Proceedings of the Royal Society A: Mathematical, Physical and Engineering Sciences*, Vol. 395, No. 1809, 1984, pp. 247–263.

[5] Howe, M. S., "The Turbulent Boundary-Layer Rough-Wall Pressure Spectrum at Acoustic and Subconvective Wavenumbers," *Proceedings of the Royal Society A: Mathematical, Physical and Engineering Sciences*, Vol. 415, No. 1848, 1988, pp. 141–161.

[6] Chase, D. M., "The Character of the Turbulent Wall Pressure Spectrum at Subconvective Wavenumbers and a Suggested Comprehensive Model," *Journal of Sound and Vibration*, Vol. 112, No. 1, 1987, pp. 125–147.

[7] Grissom, D., Smith, B., Devenport, W., and Glegg, S., "Rough-Wall Boundary Layer Noise: An Experimental Investigation," *13th AIAA/CEAS Aeroacoustics Conference*, may 2007.

[8] Devenport, W. J., Grissom, D. L., Nathan Alexander, W., Smith, B. S., and Glegg, S. A. L., "Measurements of roughness noise," *Journal of Sound and Vibration*, Vol. 330, No. 17, 2011, pp. 4250–4273.

[9] Glegg, S. and Devenport, W., "The far-field sound from rough-wall boundary layers," *Proceedings of the Royal Society A: Mathematical, Physical and Engineering Sciences*, Vol. 465, No. 2106, 2009, pp. 1717–1734.

[10] Lighthill, M. J., "On Sound Generated Aerodynamically. I. General Theory," *Proceedings of the Royal Society A: Mathematical, Physical and Engineering Sciences*, Vol. 211, No. 1107, 1952, pp. 564–587.

[11] Lighthill, M. J., "On Sound Generated Aerodynamically. II. Turbulence as a Source of Sound," *Proceedings of the Royal Society A: Mathematical, Physical and Engineering Sciences*, Vol. 222, No. 1148, 1954, pp. 1–32.

[12] Goldstein, M., *Aeroacoustics*, McGraw Hill, New York, NY, 1976.

[13] Devenport, W., Wahl, E. A., Glegg, S. A. L., Nathan Alexander, W., and Grissom, D. L., "Measuring surface pressure with far field acoustics," *Journal of Sound and Vibration*, Vol. 329, No. 19, 2010, pp. 3958–3971.

[14] Corcos, G. M., "The structure of the turbulent pressure field in boundary layer flows," *Journal of Fluid Mechanics*, Vol. 18, 1964, pp. 353–378.

[15] Lilley, G., "A study of the silent flight of the owl," *4th AIAA/CEAS Aeroacoustics Conference*, American Institute of Aeronautics and Astronautics, Toulouse, France, jun 1998.

[16] Graham, R. R., "The silent flight of owls," *The Journal of the Royal Aeronautical Society*, Vol. 38, 1934, pp. 837–843.

[17] Kroeger, R. A., Grushka, H. D., and Helvey, T. C., "Low Speed Aerodynamics for Ultra-Quiet Flight," Tech. rep., Air Force Flight Dynamics Laboratory, 1972.

[18] Klän, S., Bachmann, T., Klaas, M., Wagner, H., and Schröder, W., "Experimental analysis of the flow field over a novel owl based airfoil," *Experiments in Fluids*, Vol. 46, No. 5, 2009, pp. 975–989.

[19] Klän, S., Burgmann, S., Bachmann, T., Klaas, M., Wagner, H., and Schröder, W., "Surface structure and dimensional effects on the aerodynamics of an owl-based wing model," *European Journal of Mechanics - B/Fluids*, Vol. 33, 2012, pp. 58–73.

[20] Bachmann, T., *Anatomical, Morphometrical and Biomechanical Studies of Barn Owls' and Pigeons' Wings*, Ph.D. thesis, 2010.

[21] Ffowcs Williams, J. E. and Hall, L. H., "Aerodynamic sound generation by turbulent flow in the vicinity of a scattering half plane," *Journal of Fluid Mechanics*, Vol. 40, No. 4, 1970, pp. 657–670.

[22] Chase, D. M., "Sound Radiated by Turbulent Flow off a Rigid Half-Plane as Obtained from a Wavevector Spectrum of Hydrodynamic Pressure," *The Journal of the Acoustical Society of America*, Vol. 52, No. 3B, 1972, pp. 1011–1023.

[23] Willmarth, W. W., "Pressure Fluctuations Beneath Turbulent Boundary Layers," *Annual Review of Fluid Mechanics*, Vol. 7, No. 1, jan 1975, pp. 13–36.

[24] Batchelor, G. K., "Pressure fluctuations in isotropic turbulence," *Mathematical Proceedings of the Cambridge Philosophical Society*, Vol. 47, No. 02, apr 1951, pp. 359.

[25] Chandiramani, K. L., "Diffraction of evanescent waves, with applications to aerodynamically scattered sound and radiation from unbaffled plates," *The Journal of the Acoustical Society of America*, Vol. 55, No. 1, 1974, pp. 19–29.

[26] Chase, D. M., "Noise Radiated from an Edge in Turbulent Flow," *AIAA Journal*, Vol. 13, No. 8, 1975, pp. 1041–1047.

[27] Amiet, R. K., "Noise due to turbulent flow past a trailing edge," *Journal of Sound and Vibration*, Vol. 47, No. 3, aug 1976, pp. 387–393.

[28] Amiet, R. K., "Effect of the Incident Surface Pressure Field on Noise Due to Turbulent Flow Past a Trailing Edge," *Journal of Sound and Vibration*, Vol. 57, No. 2, 1978, pp. 305–306.

[29] Brooks, T. F. and Hodgson, T. H., "Trailing Edge Noise Prediction From Measured Surface Pressures," *Journal of Sound and Vibration*, Vol. 78, No. 1, 1981, pp. 69–117.

[30] Brooks, T. F., Pope, D. S., and Marcolini, M. A., "Airfoil Self-Noise and Prediction," Tech. rep., NASA, 1989.

[31] Brooks, T. F., Humphreys, W. M., and Humphreys, J. W., "Effect of directional array size on the measurement of airframe noise components," *5th AIAA Aeroacoustics Conference*, Bellevue, Washington, may 1999, pp. 1–20.

[32] Brooks, T. F. and Humphreys, W. M., "A deconvolution approach for the mapping of acoustic sources (DAMAS) determined from phased microphone arrays," *Journal of Sound and Vibration*, Vol. 294, No. 4-5, 2006, pp. 856–879.

[33] Amiet, R., "Refraction of sound by a shear layer," *Journal of Sound and Vibration*, Vol. 58, No. 4, 1978, pp. 467–482.

[34] Bahr, C., Zawodny, N. S., Yardibi, T., Liu, F., Wetzel, D., Bertolucci, B., and Cattafesta, L., "Shear Layer Time-Delay Correction Using a Non-Intrusive Acoustic Point Source," *International Journal of Aeroacoustics*, Vol. 10, No. 5-6, oct 2011, pp. 497–530.

[35] Mueller, T. J., editor, *Aeroacoustic Measurements*, Springer-Verlag, 2002.

[36] Hogbom, J. A., "Aperture synthesis witha non-regular distribution of interferometer baselines," *Astronomy and Astrophysics Supplement*, Vol. 15, 1974, pp. 417–426.

[37] Brooks, T. F. and Humphreys, W. M., "Extension of DAMAS Phased Array Processing for Spatial Coherence Determination (DAMAS-C)," 2006.

[38] Sijtsma, P., "CLEAN based on spatial source coherence," *International journal of aeroacoustics*, Vol. 6, No. 4, 2007, pp. 357–374.

[39] Hutcheson, F. V. and Brooks, T. F., "Measurement of Trailing Edge Noise Using Directional Array and Coherent Output Power Methods," *Aeroacoustics*, Vol. 1, No. 4, 2002, pp. 329–353.

[40] Hutcheson, F. V. and Brooks, T. F., "Effects of Angle of Attack and Velocity on Trailing Edge Noise Determined using Microphone Array Measurements," *Aeroacoustics*, Vol. 5, No. 1, 2006, pp. 39–66.

[41] Oerlemans, S., Sijtsma, P., and Méndez López, B., "Location and quantification of noise sources on a wind turbine," *Journal of Sound and Vibration*, Vol. 299, No. 4-5, 2007, pp. 869–883.

[42] Devenport, W. J., Burdisso, R. A., Borgoltz, A., Ravetta, P. A., Barone, M. F., Brown, K. A., and Morton, M. A., "The Kevlar-walled anechoic wind tunnel," *Journal of Sound and Vibration*, Vol. 332, No. 17, 2013, pp. 3971–3991.

[43] Devenport, W., Burdisso, R. A., Camargo, H., Crede, E., Remillieux, M., Rasnick, M., and Van Seeters, P., "Aeroacoustic Testing of Wind Turbine Airfoils," Tech. rep., 2010.

[44] Howe, M. S., "Aerodynamic Noise of a Serrated Trailing Edge," *Journal of Fluids and Structures*, Vol. 5, 1991, pp. 33–45.

[45] Oerlemans, S., Fisher, M., Maeder, T., and Kögler, K., "Reduction of Wind Turbine Noise Using Optimized Airfoils and Trailing-Edge Serrations," *AIAA Journal*, Vol. 47, No. 6, 2009, pp. 1470–1481.

[46] Gruber, M., Joseph, P., and Chong, T., "On the mechanisms of serrated airfoil trailing edge noise reduction," *17th AIAA/CEAS Aeroacoustics Conference (32nd AIAA Aeroacoustics Conference)*, American Institute of Aeronautics and Astronautics, Portland, Oregon, jun 2011.

[47] Chong, T. P., Vathylakis, A., Joseph, P. F., and Gruber, M., "Self-Noise Produced by an Airfoil with Nonflat Plate Trailing-Edge Serrations," *AIAA Journal*, Vol. 51, No. 11, nov 2013, pp. 2665–2677.

[48] Moreau, D. J. and Doolan, C. J., "Noise-Reduction Mechanism of a Flat-Plate Serrated Trailing Edge," *AIAA Journal*, Vol. 51, No. 10, oct 2013, pp. 2513–2522.

[49] Herr, M. and Dobrzynski, W., "Experimental Investigations in Low-Noise Trailing Edge Design," *AIAA Journal*, Vol. 43, No. 6, 2005, pp. 1167–1175.

[50] Jaworski, J. W. and Peake, N., "Aerodynamic noise from a poroelastic edge with implications for the silent flight of owls," *Journal of Fluid Mechanics*, Vol. 723, 2013, pp. 456–479.

[51] Crighton, D. G. and Leppington, F. G., "Scattering of aerodynamic noise by a semi-infinite compliant plate," *Journal of Fluid Mechanics*, Vol. 43, No. 04, oct 1970, pp. 721.

[52] Howe, M. S., "On the Added Mass of a Perforated Shell, with Application to the Generation of Aerodynamic Sound by a Perforated Trailing Edge," *Proceedings of the Royal Society A: Mathematical, Physical and Engineering Sciences*, Vol. 365, No. 1721, mar 1979, pp. 209–233.

[53] Walsh, M. J., Weinstein, L. M., Walsh, M. J., and Weinstein, L. M., "Drag and Heat Transfer on Surfaces with Small Longitudinal Fins," *AIAA 11th Fluid and Plasma Dynamics Conference*, Seattle, Washington, 1978.

[54] Bechert, D. W., Bruse, M., Hage, W., Van Der Hoeven, J. G. T., and Hoppe, G., "Experiments on drag-reducing surfaces and their optimization with an adjustable geometry," *Journal of Fluid Mechanics*, Vol. 338, 1997, pp. 59–87.

[55] Bechert, D. and Reif, W., "On the Drag Reduction of the Shark Skin," *23rd Aerospace Sciences Meeting*, 1985.

[56] Walsh, M. J., "Riblets as a Viscous Drag Reduction Technique," *AIAA Journal*, Vol. 21, No. 4, 1983, pp. 485–486.

[57] Williams, M. D., Reeder, M. F., Maple, R. C., and Solfelt, D. A., "Modeling, Simulation, and Flight Tests for a T-38 Talon with Wing Fences," *Journal of Aircraft*, Vol. 47, No. 2, 2010, pp. 423–433.

[58] Lin, J. C., "Review of research on low-profile vortex generators to control boundary-layer separation," *Progress in Aerospace Sciences*, Vol. 38, No. 4, 2002, pp. 389–420.

Chapter 3

Bio-inspired canopies for the reduction of roughness noise

This chapter presents the development and testing of a method for the control of roughness noise which takes inspiration from the anatomy of owls' feathers, published as "Bio-inspired canopies for the reduction of roughness noise" in the Journal of Sound and Vibration (2016 385:33-54, DOI 10.1016/j.jsv.2016.08.027).

Journal of Sound and Vibration 385 (2016) 33–54

Contents lists available at ScienceDirect

Journal of Sound and Vibration

journal homepage: www.elsevier.com/locate/jsvi

Bio-inspired canopies for the reduction of roughness noise

Ian A. Clark [a,*], Conor A. Daly [b], William Devenport [a], W. Nathan Alexander [a], Nigel Peake [b], Justin W. Jaworski [c], Stewart Glegg [d]

[a] Virginia Polytechnic Institute and State University, Blacksburg VA 24061, USA
[b] University of Cambridge, Cambridge CB3 0WA, UK
[c] Lehigh University, Bethlehem PA 18015, USA
[d] Florida Atlantic University, Boca Raton FL 33431, USA

ARTICLE INFO

Article history:
Received 4 November 2015
Received in revised form
6 June 2016
Accepted 24 August 2016
Handling Editor: P. Joseph
Available online 8 September 2016

ABSTRACT

This work takes inspiration from the structure of the down covering the flight feathers of larger species of owls, which contributes to their ability to fly almost silently at frequencies above 1.6 kHz. Microscope photographs of the down show that it consists of hairs that form a structure similar to that of a forest. The hairs initially rise almost perpendicular to the feather surface but then bend over in the flow direction to form a canopy with an open area ratio of about 70 percent. Experiments have been performed to examine the noise radiated by a large open area ratio canopy suspended above a surface. The canopy is found to dramatically reduce pressure fluctuations on the underlying surface. While the canopy can produce its own sound, particularly at high frequencies, the reduction in surface pressure fluctuations can reduce the noise scattered from an underlying rough surface at lower frequencies. A theoretical model is developed which characterizes the mechanism of surface pressure reduction as a result of the mixing layer instability of flow over forest canopies.

1. Introduction

Many species of owl are able to hunt in effective silence, a feat which is believed to be linked to three unique physical attributes [1]: a comb of evenly-spaced bristles along the wing leading-edge; a compliant and porous fringe of feathers at the trailing-edge; and a velvety down material distributed over the upper wing surface. Early work by Kroeger et al. [2] investigated these features experimentally with live owls, where the removal of the leading-edge comb resulted in increased aerodynamic noise as well as a loss of flight control authority. Related experiments by Hersh et al. [3] for airfoils with leading-edge serrations demonstrated their ability to reduce aerodynamic noise. Trailing-edge noise is a known major contributor to airframe noise, and recent theoretical modeling by Jaworski and Peake [4,5] has suggested that the porous and compliant nature of the trailing edge can effectively eliminate the edge scattering mechanism. Specifically, they show, in a scaling sense, that trailing-edge noise levels may be reduced to levels comparable to ordinarily secondary noise mechanisms such as roughness noise.

Work on the downy surface, particularly as it relates to the acoustics of owl flight, is somewhat limited. Lilley [6] postulated by process of elimination that the downy material, which creates a rough but compliant upper wing surface,

* Corresponding author.
E-mail address: clarki91@vt.edu (I.A. Clark).

http://dx.doi.org/10.1016/j.jsv.2016.08.027
0022-460X/

contains a mechanism to diminish aerodynamic noise at the source for a broad frequency range relevant to the owl. Bachmann et al. [7] measured the barbules (downy fibers) of barn owls and compared them in length and frequency density to pigeon feathers. In their discussion of the morphology of the barbules, the impact of these barbules on the noise generation is left an open question but they speculate that they reduce the noise of rubbing between feathers and perhaps alter the boundary layer. Additional details of the feather anatomy, including that of the velvety surface, are given later by Bachmann [8]. A similar feather comparison (this time between an eagle owl and a buzzard) by Chen et al. [9] arrives at essentially the same conclusions, noting that the length of the barbules creates a porous structure that could affect the acoustics. However, like the Bachmann et al. [7] study, the function of the barbules/down is not clarified, and in the case of Chen et al. [9], it is speculated that it behaves as an ordinary sound absorber for high frequencies. Later investigations by Klan et al. [10,11] installed artificial hairy surfaces to match the measured length and density of the barn owl barbules in the study of Bachmann et al. [7]. The focus was on the effect of the hairs on the fluid flow and not on noise generation/suppression. However, there is no effort here or elsewhere to measure the elastic properties of the barbules or try to match them quantitatively to an elastic barbule material in their experiments.

The present work seeks to examine the hypothesis of Lilley [6] with a study of the owl down and subsequent theoretical modeling and aeroacoustic experiments informed by the structure of the down. The organization of this paper is as follows. First, a photographic study is described that is carried out with feathers of well-known silent owl species, which identifies a 'forest' structure that creates a buffer between the turbulent boundary layer flow and the wing (or wall) surface. This concept is then explored experimentally for specialized smooth and rough surfaces veiled by various porous materials to emulate the effect of the owl down. This work is then investigated theoretically to describe the attenuation of surface pressure fluctuations with a mixing layer instability model. The paper is then concluded with a summary of findings and results.

2. The structure of the owl feather down

As discussed above, one possible noise-reducing mechanism of the owl's feathers is the downy coating consisting of flexible fibers on the surface of the feather. In order to investigate this further and to prepare for experimentation, a visual study of some owl feathers was performed to understand the structure of the fibers and to determine the average length and density of the fibers.

Four primary feathers were studied which were molted by an eagle owl, a great gray owl, and a snowy owl, Fig. 1. Multiple locations on one feather were studied to characterize changes in fiber size and density with position. The feathers

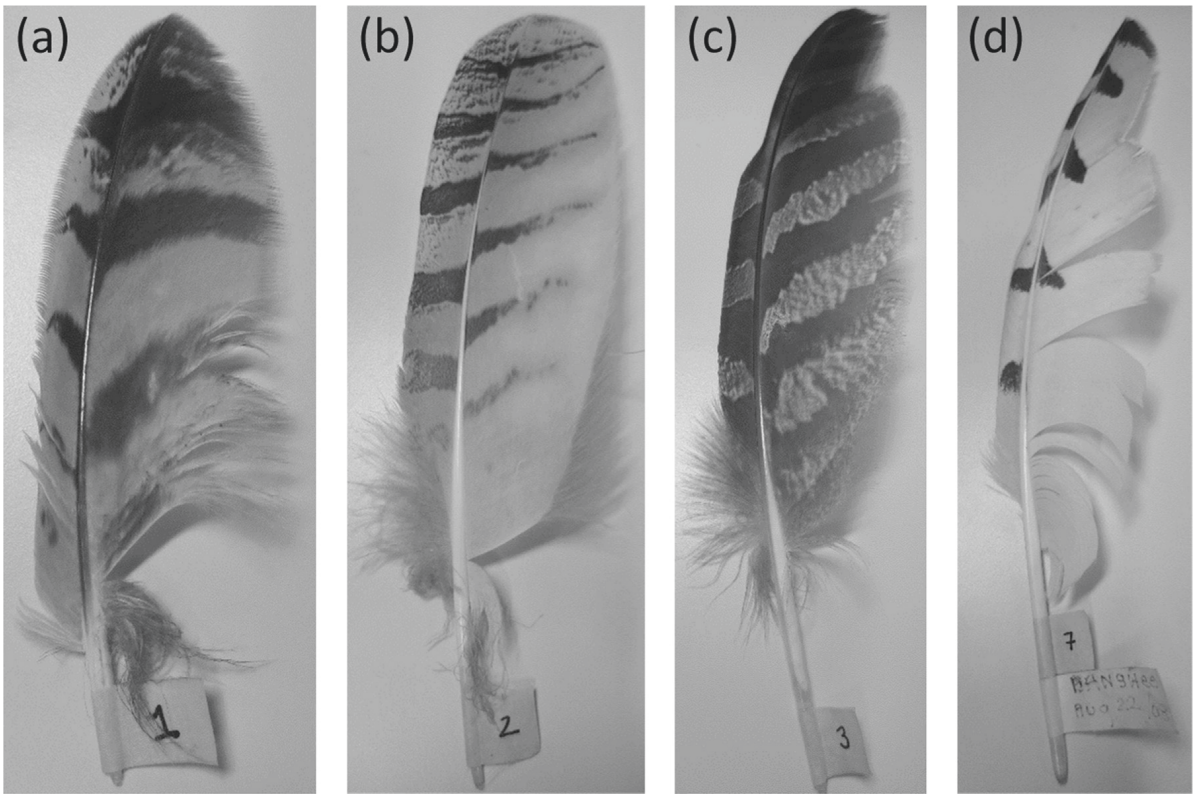

Fig. 1. Feathers examined: (a,b) Eurasian eagle owl (Bubo bubo) (c) great gray owl (Strix nebulosi) (d) snowy owl (Bubo scandiacus).

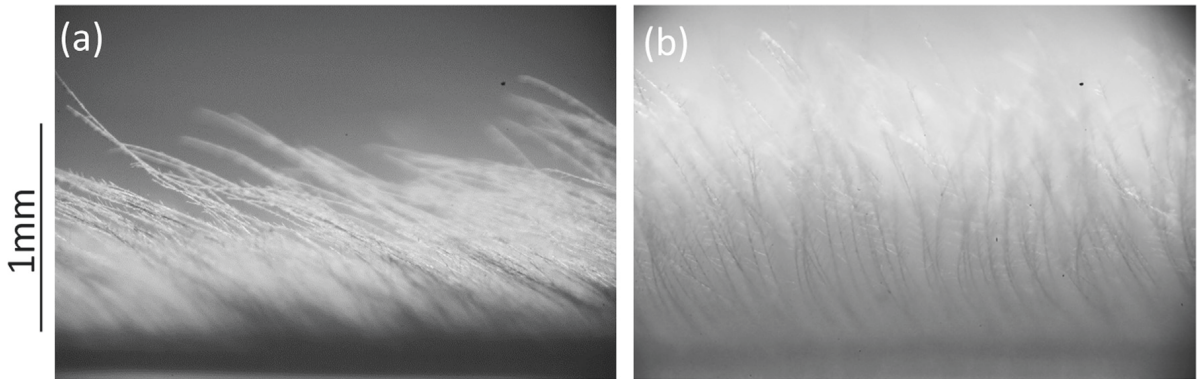

Fig. 2. Cross section views of feathers from (a) a great gray owl and (b) a snowy owl.

were studied and imaged using a Nikon SMZ1500 microscope and a Nikon D300S Digital SLR camera. An Edmund 53713 micrometer was used to scale the images. Aside from scaling the 2D images, the focal adjustment of the microscope was calibrated in order to obtain measurements in the vertical plane.

In cross section (e.g. Fig. 2) the feathers are seen to be covered in hairs that typically rise 1 mm off the surface. The samples for these pictures were approximately taken from the center span and chord of the feathers. In different parts of the owl's wing, the hairs rise at different angles to the feather surface. The individual hairs are also barbed, a feature that is particularly clearly seen in planform view (Fig. 3c). The hairs tend to be longer near the root of the feathers and shorter near the tip.

Using shallow depth of focus in planform view it is clear that the surface structure is organized into layers (Fig. 3). The lowest layer (the substrate) is formed by an apparently impermeable mat of fibers (Fig. 3a). Rising from these fibers is a 'forest' of hairs visible in Fig. 3b. After rising about 0.5 mm off the substrate, the hairs bend over creating a 'canopy' (Fig. 3c), which is enhanced by the barbs on the individual hairs.

Overall, the average vertical thickness of the downy coating is 0.25 to 1.5 mm. The coating is thicker near the root of the feather and thinner near the tip of the feather. The average lengths of the fibers are on the order of 1–2 mm. Based on the number and arrangement of the fibers above the surface of the feather, it is estimated that the canopy formed by the down

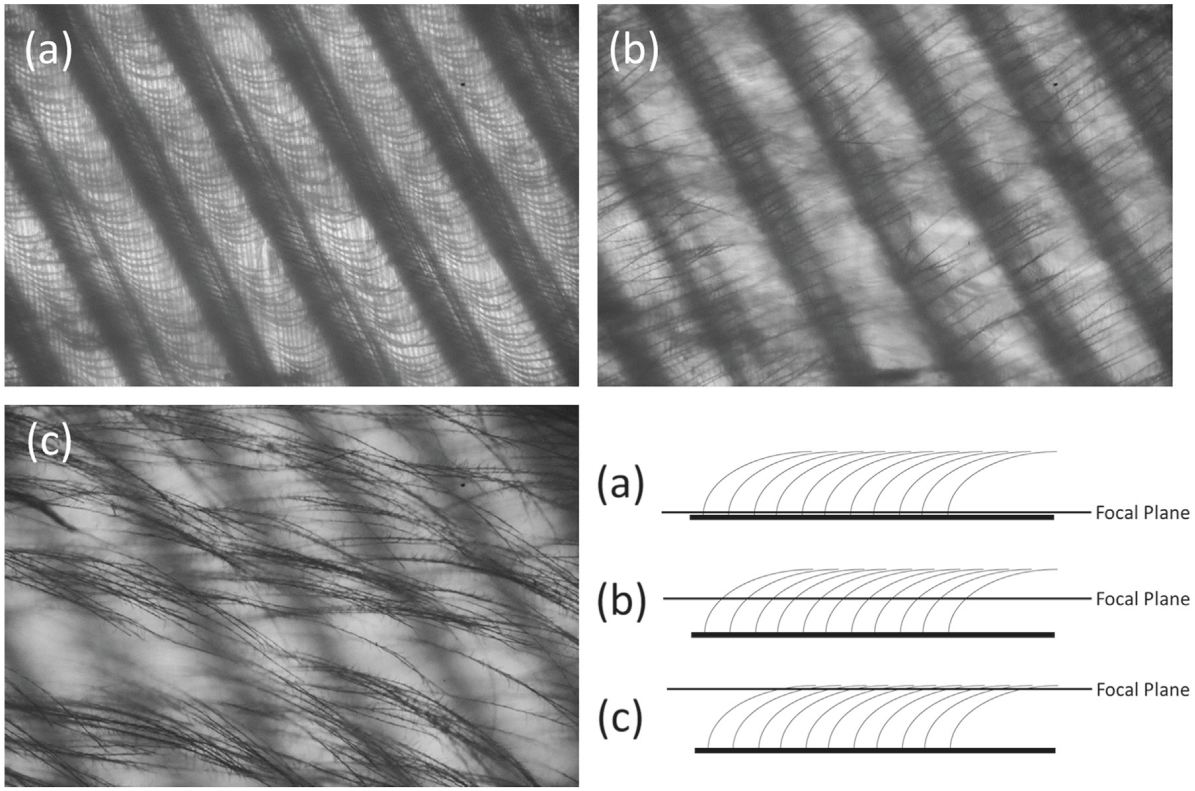

Fig. 3. Planform views at different depths. (a) Impermeable base layer, (b) middle layer, (c) top layer or 'canopy' (great gray owl).

has an open area ratio of approximately 70 percent., which is within the range of 45–90 percent. given by Bachmann [8] for those areas of feathers which are exposed to the flow. The fibers feature very short (~0.05 mm) barbs along the lengths of the fibers which fill some of the area between the fibers.

The length scales of the owl's downy coating are very small, and the flow Reynolds number based on the length of the fibers is estimated to be around 100, while that based on the diameter of the fibers or the lengths of the barbs could be as low as 7. It was also evident that the fibers are oriented in a certain direction which would be aligned with the flow during normal flight.

3. Experimental apparatus and instrumentation

Experimental studies were performed on the aeroacoustics of flow surfaces with configurations inspired by the results of the photographic study. Surface pressure fluctuations and sound produced by a boundary layer flowing over smooth and rough surfaces were measured. The effects of placing a series of high open area ratio fabric coverings just above these surfaces was examined. The fabric acted as a canopy over the surface roughness in order to simulate the downy coating of the owl's feathers. The rough surfaces included two surfaces (hemispherical and sandpaper) whose roughness noise characteristics are well known from previous studies [12,13].

3.1. Wind tunnel facility

The Virginia Tech Anechoic Wall-Jet Wind Tunnel was used, shown in Fig. 4. This wind tunnel produces a quiet two-dimensional wall jet within an acoustic enclosure that flows and decays over a 3 m long smooth flat plate. The wall jet consists of a boundary layer flow adjacent to a flat plate topped by a mixing layer. This open upper boundary allows for the measurement of far-field noise without the need to place microphones in or near the flow. The small scale of the flow source needed for a wall jet allows background sound to be reduced to a minimum and the natural decay of this flow enables any edges (and potential scattering sources) to be positioned away from regions of significant flow velocity. The extremely low background noise levels allow for high signal-to-noise ratio, single microphone measurements of roughness noise over a range of carefully controlled boundary layer conditions, as well as measurements of supporting aerodynamic data.

The wall jet exhausts from a nozzle 1219 mm wide and 12.7 mm high with an initial velocity that was varied between 20 and 60 m/s. By the time the jet exits from under the baffle it has reached a fully-developed form with two-dimensional flow over its central 900 mm region. The scaling parameters of its mean velocity profile downstream of this point can be

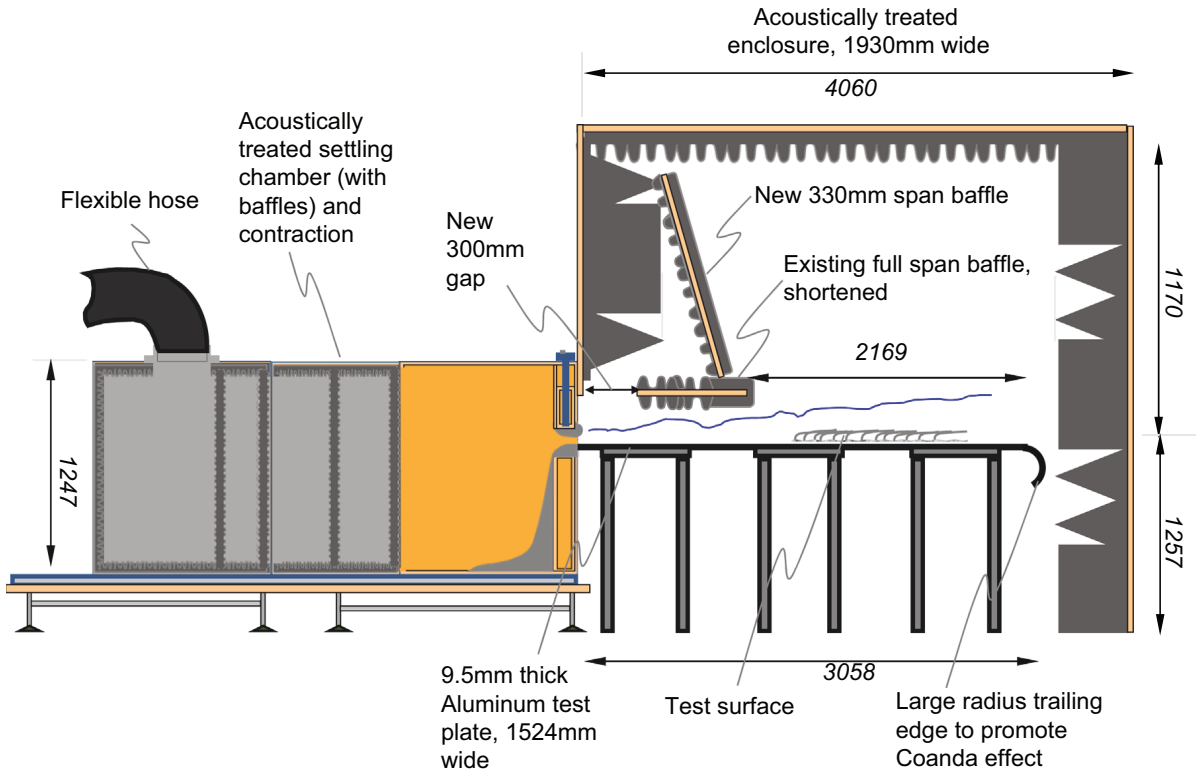

Fig. 4. Side-view schematic of the Virginia Tech Anechoic Wall Jet Wind Tunnel. All dimensions shown are in mm.

Table 1
Boundary layer properties at $\boldsymbol{x} =$ 1410 mm.

Jet speed, U_j [m/s]	Max speed, U_m [m/s]	BL thickness, δ [mm]
20	6.5	18.5
30	10.1	17.2
40	13.6	16.3
50	17.3	15.7
60	21.0	15.2

accurately described using the power-law relations of Wygnanski et al. [14]:

$$\frac{U_m}{U_j} = 1.6814\, Re_j^{n+1} Re_x^n \tag{1.1}$$

$$\frac{\delta}{b} = 0.1153\, Re_j^{p-2} Re_x^p \tag{1.2}$$

where U_m is the maximum velocity in the mean velocity profile (at the boundary layer edge), U_j is the jet exit velocity, δ is the boundary layer thickness (i.e. the distance from the wall to U_m), b is the nozzle height, and Re_j and Re_x are jet-exit velocity Reynolds numbers based, respectively, on the nozzle height and distance x downstream from the nozzle. The values n and p were found experimentally to be -0.4702 and 0.9099, respectively. Flow properties implied by the above relations for the location $x = 1410$ mm (the streamwise center of the surfaces tested) are given in Table 1.

3.2. Rough surfaces

Two rough surfaces were tested. Both a hemispherical roughness fetch and a sandpaper roughness fetch were positioned symmetrically with respect to the wall-jet plate centerline, were centered at $x = 1410$ mm, and were attached directly to the wall-jet plate. The hemispherical roughness, pictured in Fig. 5a, extended 300 mm in the streamwise direction and 600 mm spanwise and consisted of 3 mm-radius hemispheres spaced 16.5 mm center to center in a square array. This surface was identical to that tested previously as part of roughness noise studies conducted by Alexander [12]. The second surface, pictured in Fig. 5b, was formed by a sheet of 20-grit sandpaper roughness extending 200 mm streamwise and 600 mm spanwise. This type of surface, tested previously by Devenport et al. [13], has a nominal grain size of 0.95 mm, a grain density of 0.23 grains/mm^2, and an RMS roughness height of 0.206 mm. The edges of these roughness patches were taped and faired to the surrounding wall using 0.12 mm thick aluminum tape. Devenport et al. [13] demonstrated that the perimeter of the roughness substrate and the tape produces no detectable noise with this arrangement.

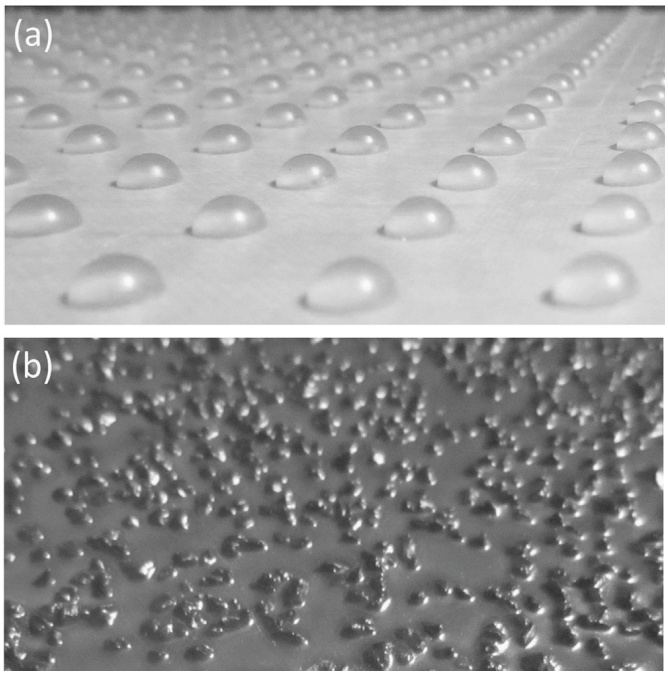

Fig. 5. (a) Hemispherical and (b) 20-grit sandpaper rough surfaces.

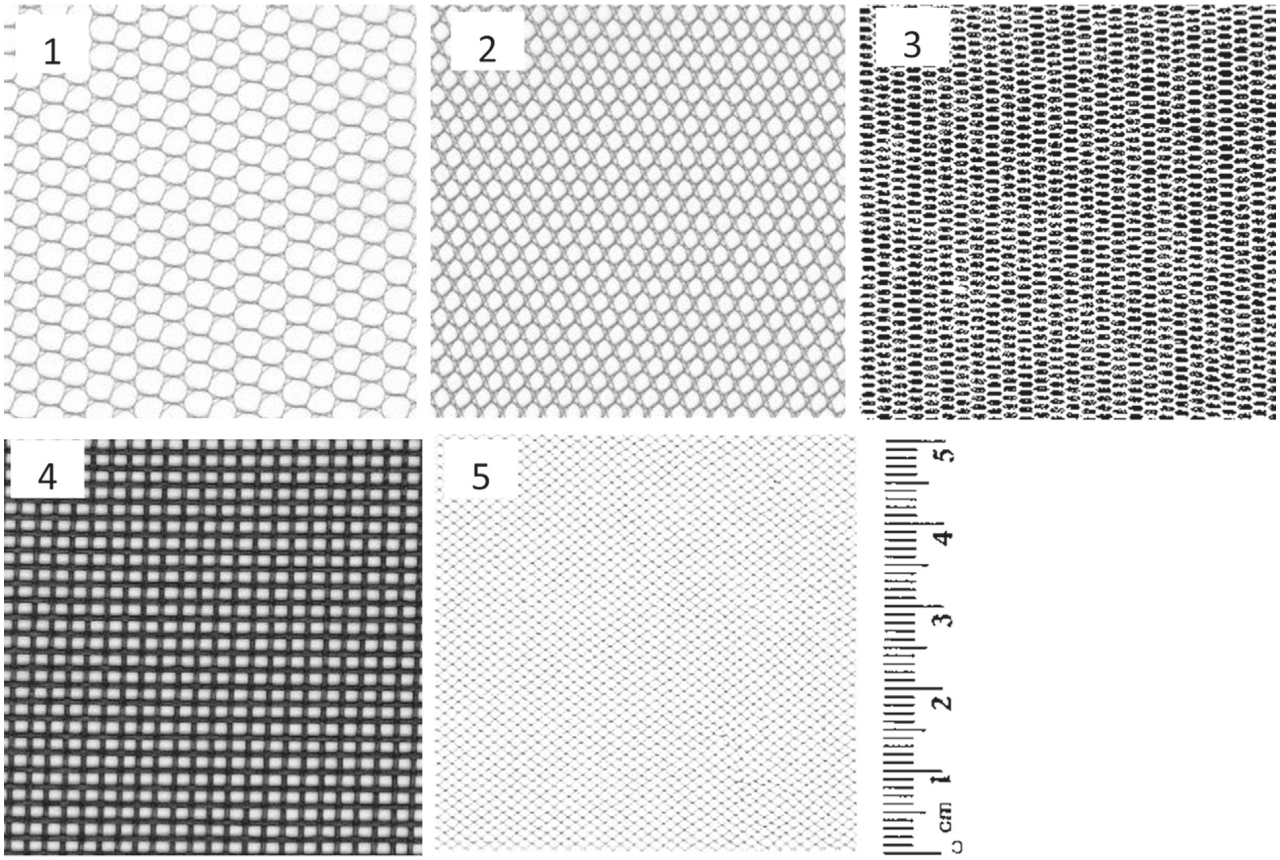

Fig. 6. Images of the fabrics used. Fabrics were mounted so that the flow direction was top to bottom as shown in these figures. Note the diagonal orientation of the threads in the fabric 5, the finest mesh.

3.3. *Fabric canopies*

Five mesh-like polyester or nylon fabrics, later down selected to four, were used to mimic the effect of the canopy portion of the owl down. The fabrics were selected based on qualitative similarity to the structure of the owl's downy coating (high open area ratio, interlocking fibers). Pictures of the fabrics are shown in Fig. 6. Characteristics of the fabrics are listed in Table 2.

The fabrics are structured as meshes with a 2.5:1 ratio of pore sizes, a 5:1 ratio of thread diameters, and open area ratios from 38 percent to 76 percent. In terms of filament size and open area ratio, fabric 5 most closely simulates the owl-down canopy, but even with this finest fabric the thread diameter is about three times the estimated diameter of the owl's hairs. The least similar is fabric 4 – a much heavier mesh than the other fabrics. The fabric meshes are not isotropic surfaces, although some display rotational symmetries. All fabrics were tested with the vertical direction in Fig. 6 aligned with the flow direction, thus placing a significant fraction of the fibers perpendicular to the flow direction for fabrics 1, 3 and 4, but with most of the fibers at 45° to the flow for fabrics 2 and 5.

For all conditions the fabric canopies were suspended above the surface by using two tapered half-round dowels mounted on either side of the test area, as shown schematically in Fig. 7–9. The dowels effectively created acoustically silent 4-mm high ridges running down either side of the test area. The 25 mm long tapered sections of the dowel upstream and downstream of the test area produced short sections of fabric ramp at the leading and trailing edges of the test areas.

Table 2
Characteristics of fabric canopies.

Fabric	Material	Open Area	Pore Diameter [mm]	Thread Diameter [mm]	Tension Modulus [N/m]
1	Nylon	75%	3.9	0.3	508
2	Nylon	64%	3.1	0.4	555
3	Nylon	76%	2.1	0.2	1320
4	Polyester	38%	2.3	0.7	7930
5	Nylon	70%	1.6	0.06	117

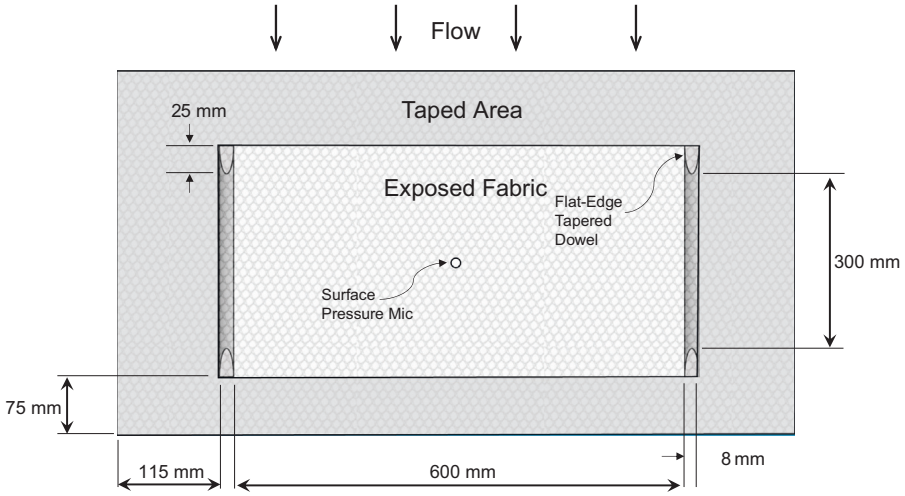

Fig. 7. Schematic view of fabric canopy suspended above smooth plate, with surface pressure microphone at center. The grey area outside the tapered dowels was covered with tape to restore a smooth surface.

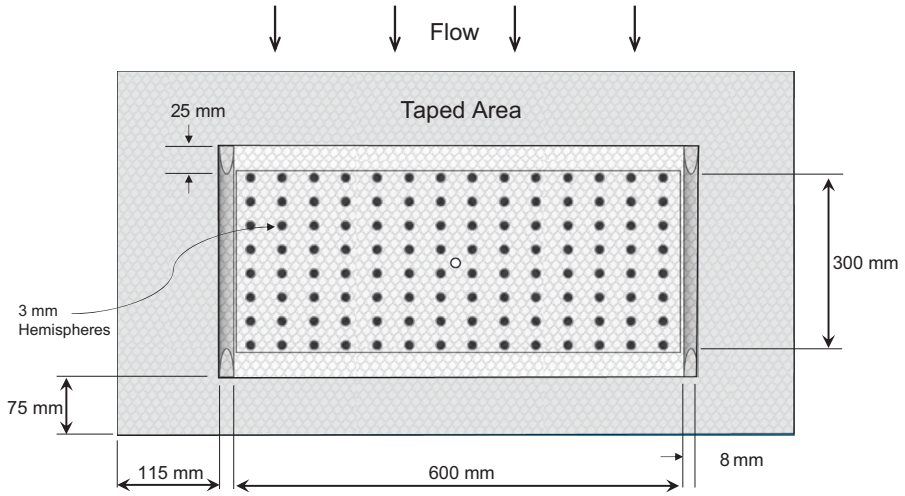

Fig. 8. Schematic view of fabric canopy suspended above hemispherical roughness.

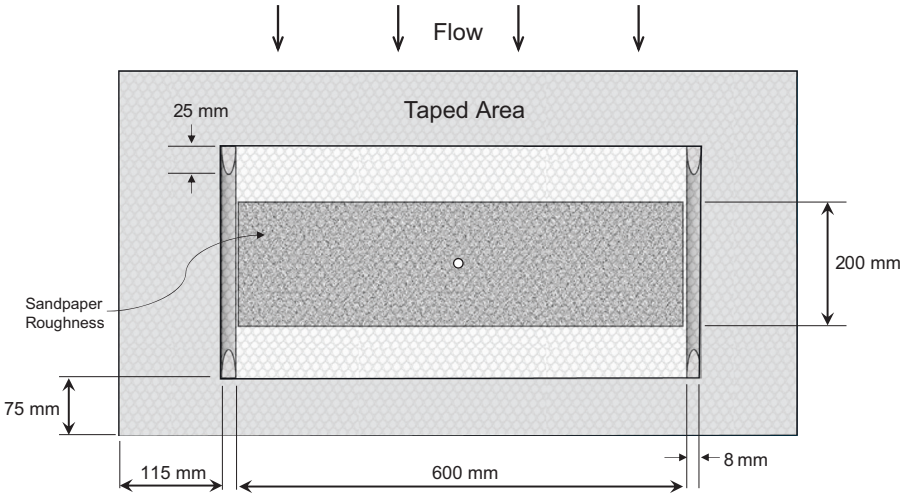

Fig. 9. Schematic view of fabric canopy suspended above sandpaper roughness.

Draping the fabrics over these dowels, tensioning the fabric spanwise and then taping the fabrics to the flow surface outside of the test area enabled a measure of control of the fabric height. An estimated tension of 5-10 N was distributed in the spanwise direction when the fabrics were mounted above the plate, and slight tension was distributed in the streamwise direction to eliminate any wrinkling of the fabric. It was observed that the shapes of the fabrics' pores were not significantly influenced by the application of this tension.

3.4. Unidirectional canopies

Unidirectional canopies (essentially fabric canopies with fibers only aligned with the flow direction) were also tested. These were composed of fishing line (forming the fibers) suspended from a pair of 3D-printed, smoothly curved, 6.4 mm high humps (referred to as fiber supports) placed at the upstream and downstream edges of the same sandpaper roughness used in the mesh canopy experiment (Fig. 10). The fiber supports were attached to an aluminum plate, and fishing line was wrapped around the entire plate and over the supports. To accommodate the increased thickness of this surface, a shaped metal transition, 305 mm in length, was used to gradually elevate the wall-jet 12.7 mm above the base plate (Fig. 10). The transition, used previously by Awasthi et al. [15], had the shape of a shallow inflection. The 0.7 mm-high forward step at the leading edge of the transition was faired using 0.12 mm thick metal tape to eliminate it as a noise source and to minimize its flow disturbance. When assembled in the wind tunnel, the result was a surface flat and continuous with the surrounding wall, with the exception of the streamlined supports at the leading and trailing edges of the test-portion of the surface and the unidirectional canopy formed between them.

Three complete test surfaces were manufactured, each with a different fishing line diameter. Table 3 gives the relevant parameters of the three canopies. The top surfaces of the supports used with each test surface were manufactured with evenly-spaced grooves so as to precisely accommodate the fishing line fibers wound over them and to set the fiber spacing so as to produce an open area ratio of 70 percent. Fig. 11 shows close-up views of each of the three canopies suspended above sandpaper roughness.

The tension used to wrap the fishing line was intended to be kept constant at around 4–8 N using a fishing reel with a calibrated line drag setting. This was successfully accomplished for canopies 1 and 2. However, this proved more difficult

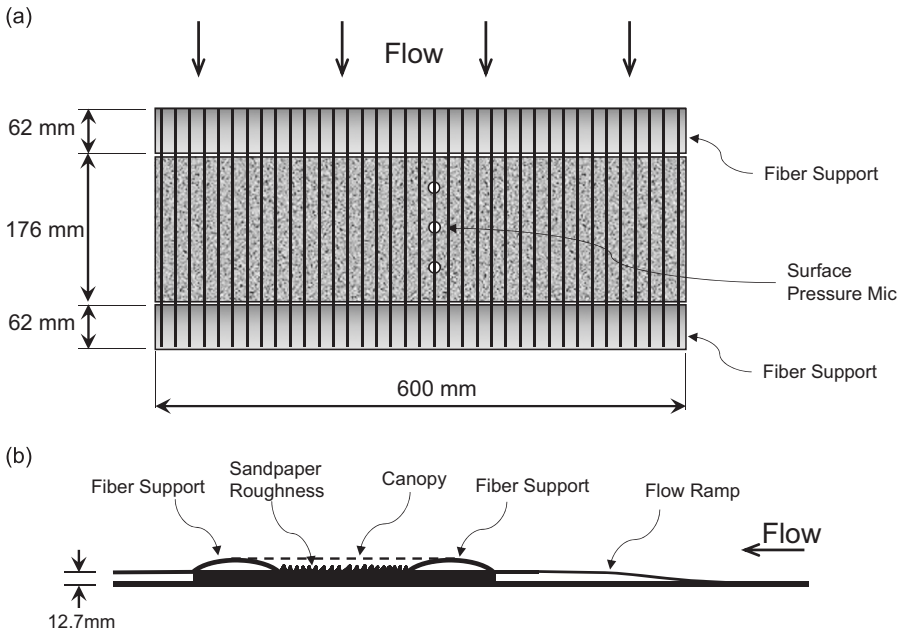

Fig. 10. Schematic view of unidirectional canopy suspended above sandpaper roughness. (a) Top View (b) Side View.

Table 3
Characteristics of unidirectional canopies.

Canopy	Fiber diameter [mm]	Fiber spacing [mm]
1	0.28	1.02
2	0.56	1.82
3	0.91	3.05

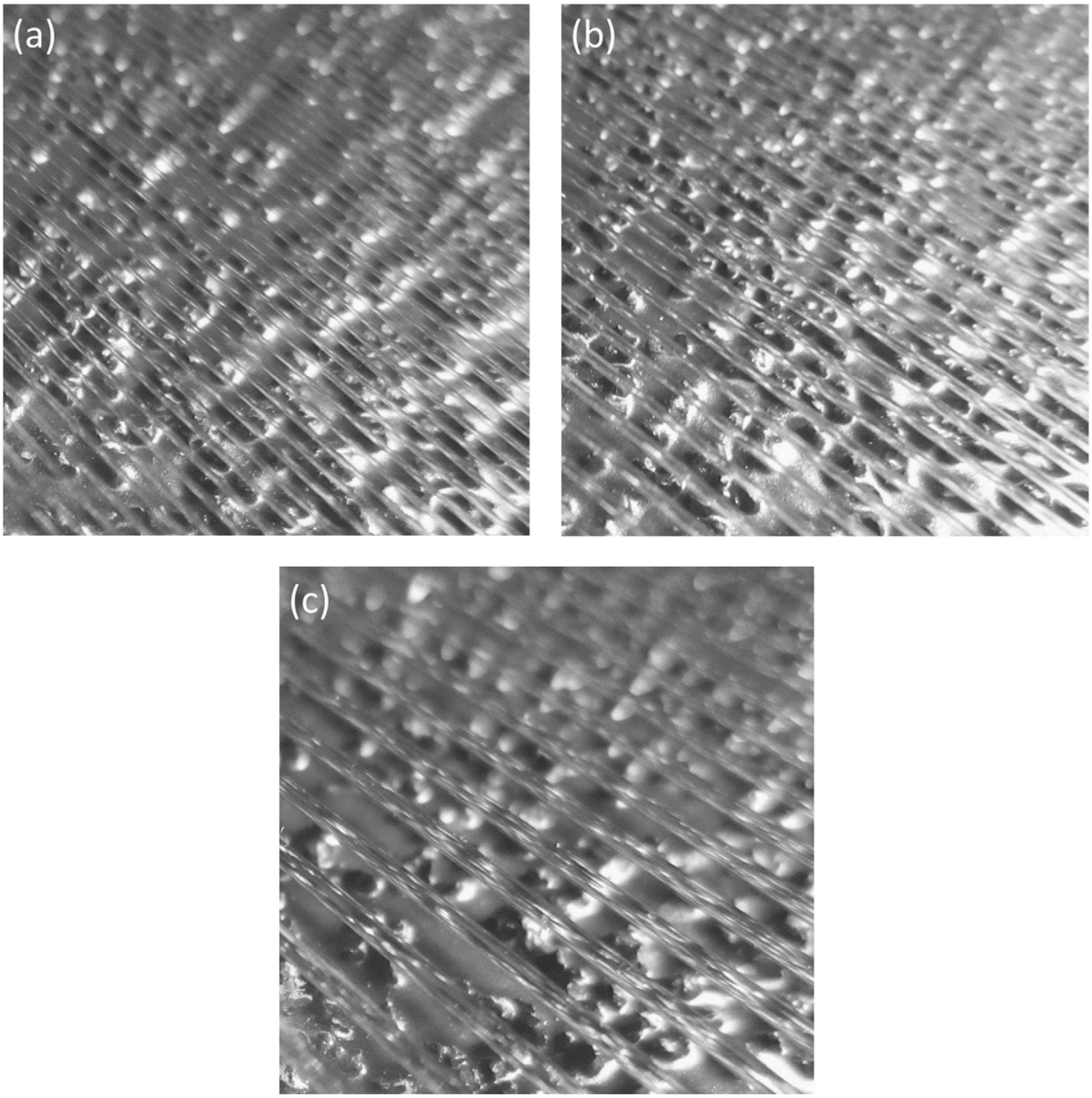

Fig. 11. Unidirectional canopies suspended above sandpaper roughness: (a) canopy 1, (b) canopy 2, and (c) canopy 3.

than expected for the thickest fishing line (canopy 3). In this case, the thread was wrapped by hand while attempting to keep the tension in the fibers constant.

3.5. Microphone Instrumentation

Measurements of the far-field sound spectrum and directivity radiated by the roughness and fabric were made using a series of six ½-inch diameter Bruel and Kjaer (B&K) Type 4190 microphones positioned in an arc 607 mm from the center of the roughness fetch with receiver angles between 55 and 129 degrees from the downstream surface. The microphone configuration is illustrated in Fig. 12. All far-field data presented in this paper was collected from the microphone located at 129°, as no additional conclusions could be drawn from the other microphones' data. Surface pressure fluctuations at the center of the test area were measured for all surface and flow conditions, either on the smooth wall or on the roughness substrate surfaces. During the unidirectional canopy experiments, surface pressure fluctuations were also measured 51 mm directly upstream and downstream of the center. Pressure fluctuations were sensed using a Sennheiser KE4-211 pinhole electret microphone with an attached ½-mm pinhole covering. Phase and amplitude characteristics of the Sennheiser, with pinhole, were obtained by calibrating it against a B&K Type 4138 microphone using a white noise source in an anechoic chamber.

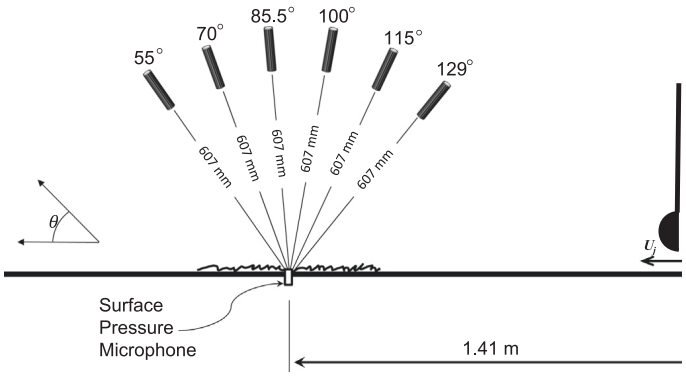

Fig. 12. Schematic, side view of microphone instrumentation in wall-jet tunnel.

4. Experimental results and discussions

4.1. The uncovered smooth and rough surfaces

Fig. 13 compares surface pressure spectra measured on the smooth wall and on the substrates of each of the rough surfaces. For the smooth wall, the surface pressure spectra display a form that is fairly typical of a wall jet. At low frequencies (less than about 1 kHz in the present flows) spectral levels are relatively high, presumably because of the pressure footprint of the energetic large scale structures that populate the outer mixing-layer portion of the flow. At mid-range frequencies, the spectra have a slope of close to -0.8, analogous to the overlap region seen in external flow boundary layers, and then at high frequencies the spectra show a rapid roll off associated with viscous attenuation. As the speed and Reynolds number of the flow increases, the spectra shift up and to the right as a result of the greater absolute energy in the turbulence, the greater convective speed over the surface pressure microphone, and the decreasing scale at which viscous dissipation becomes important.

The rough surfaces have different effects on this background form. Spectra measured at the center of the 3 mm hemispherical roughness fetch (Fig. 13a) show only very slightly altered levels compared to the smooth wall, the most marked difference being a reduction of several decibels in levels at high frequencies. Because the roughness elements were somewhat widely spaced, with the surface pressure microphone located some distance from the nearest element, the microphone did not capture the full effect of the roughness elements on the surface pressure fluctuations, the majority of which is seen in the wake of each element. This does not happen with the sandpaper roughness (Fig. 13b) which is a very effective turbulence producer and increases wall pressure fluctuations across the spectrum, particularly at high frequencies and low speeds.

Radiated noise spectra from the surfaces measured by the forward-most microphone are compared in Fig. 14. Roughness noise is generated by the scattering of these pressure fields (or at least their parent wavenumber frequency spectra) from the uneven surface geometry. The acoustic spectra for the smooth wall, of course, include no such scattering effects and instead merely indicate the background noise levels in the facility as a function of flow speed. Devenport et al. [13] identify these as result of jet noise generated at the nozzle exit. At speeds of 40 m/s and above, the hemispherical rough surface

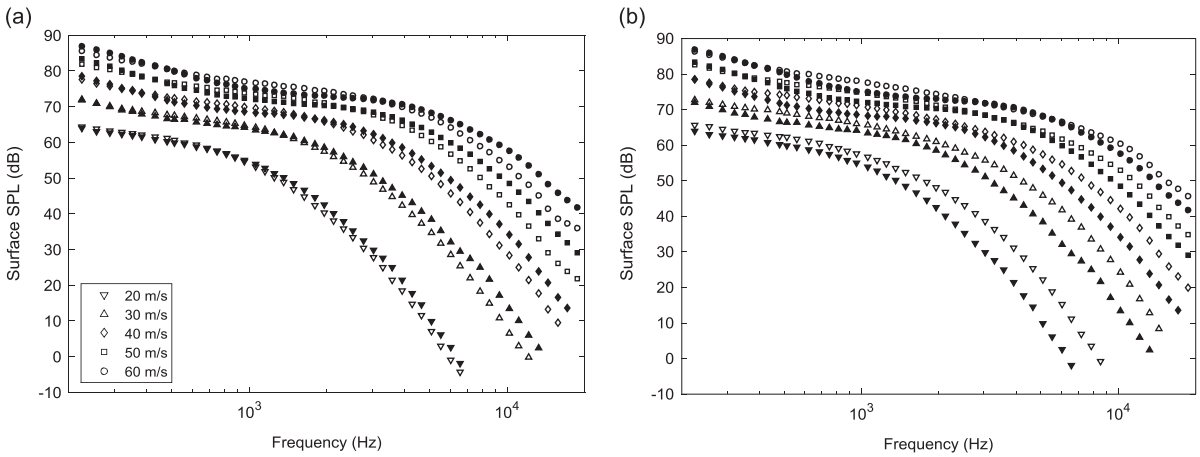

Fig. 13. Surface-pressure spectra measured with the clean wall (solid symbols) and with the (a) hemispherical and (b) sandpaper rough surfaces (open symbols). Spectral levels are 1Hz bandwidth SPL and are shown for different jet exit velocities U_j.

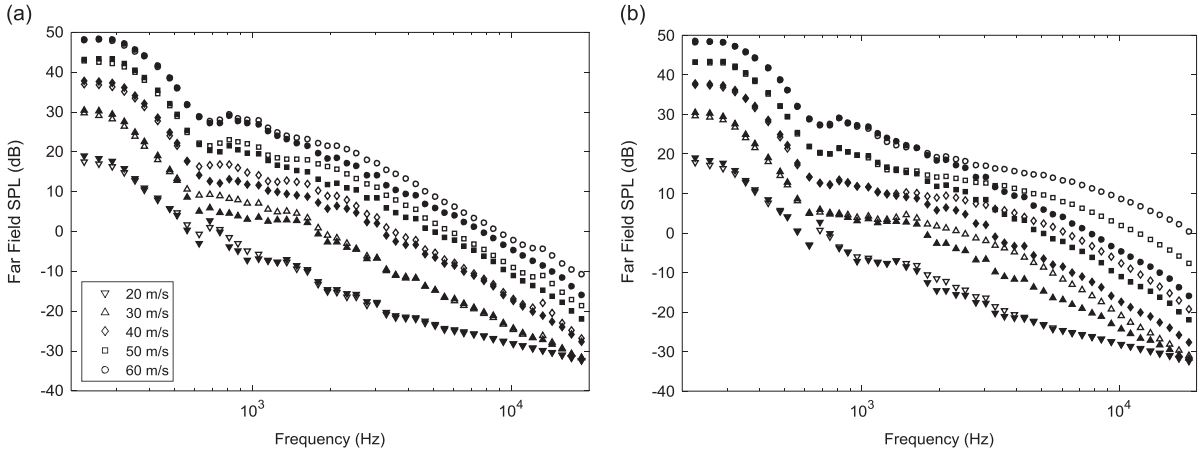

Fig. 14. Background far-field noise measurements made with the clean wall (solid symbols) and with the addition of roughness noise from the (a) hemispherical and (b) sandpaper rough surfaces (open symbols). Spectral levels are 1 Hz bandwidth SPL and are shown for different jet exit velocities U_j.

produces discernable roughness noise above the background starting at about 700 Hz and extending to the upper limit of the measured frequency range at 20 kHz. The signal to noise ratio, however, remains quite low, never exceeding about 4 dB. The sandpaper surface has sharp corners that serve as much more efficient scatterers. Signal levels are therefore much higher. Noise from the sandpaper roughness at 60 m/s becomes audible at about 2 kHz but by 20 kHz is some 18 dB above the background.

4.2. Fabric canopies

In this section acoustic and surface pressure fluctuation results are presented and discussed for the various smooth and rough surface conditions with the canopy coverings. Fabric 5, described above, will be the focus of this section for two distinct reasons. First, this canopy most closely mimics the characteristics of the owl-down canopy since it has the thinnest fibers which run approximately 45° relative to the flow direction, while the other canopies have thicker fibers, some of which run perpendicular to the flow direction. Second, it became clear from the data gathered during this experiment that fabric 5 was the most effective in reducing the far-field noise and surface pressure fluctuations while minimizing additional noise from the canopy itself. We also focus our presentation on acoustic measurements made with the forward-most far-field microphone, at a receiver angle of 129°.

Fig. 15 and 16 show the effects of installing fabric 5 over top of these different surfaces in terms of pressure fluctuations at the center surfaces and the sound recorded overhead. Considering first the surface pressure fluctuations for the smooth surface, it is evident that the canopy causes a slight increase in pressure fluctuation intensities at low frequencies (<2 kHz for 60 m/s), but a substantial reduction in pressure fluctuations at higher frequencies, particularly in the viscous roll-off region. At 9 kHz the canopy causes about a 15 dB reduction in the surface pressure fluctuations. It is almost as though the canopy increases the effective viscosity, reducing the frequency at which the roll off occurs.

While the suppressing effect of the canopy on high-frequency surface pressure fluctuations is large with the smooth wall, it becomes overwhelming with the rough surfaces. Within the hemispherical roughness fetch pressure fluctuations at 60 m/s are slightly increased below 800 Hz and reduced at higher frequencies, with the attenuation reaching some 25 dB at 9 kHz. The fabric covering over sandpaper produces very little amplification of low frequency pressure disturbances, but retains the approximate 25 dB attenuation near 10 kHz at 60 m/s, as seen for the hemispherical roughness. Interestingly, the maximum attenuation appears to increase as the flow speed and the Reynolds number are reduced, reaching 30 dB around 1500 Hz with the hemispherical roughness at 20 m/s. This suggests that the canopy is able to exert the greatest viscous influence on the flow at lower speeds due to the lower Reynolds number of the canopy fibers. At this lowest speed, the estimated Reynolds number based on the filament diameter (0.06 mm) and the local undisturbed mean flow velocity is about 20, compared to 7 for the owl down fibers. Fig. 17 shows a comparison with results obtained with the other canopy materials of Fig. 6 covering the hemispherical roughness fetch. The result is an overall increase in the attenuation of surface pressure fluctuations as the open area ratio and the pore size are reduced.

As a final point of discussion regarding the attenuation of surface pressure fluctuations, Fig. 18 shows scaled surface pressure spectra obtained with canopy 5 shrouding each underlying surface. The frequency scaling is based on the maximum local flow speed in the boundary layer (U_m) and the boundary layer thickness (δ), while the magnitude scaling is obtained by normalizing the power spectral density levels (G_{pp}) on the square of the dynamic pressure $\left(1/4\rho^2U_m^4\right)$. As seen in the figures, the attenuation of surface pressure fluctuations starts at a non-dimensional frequency near one, suggesting that the canopies are having the majority of their effect on turbulent structures which would be located in the boundary

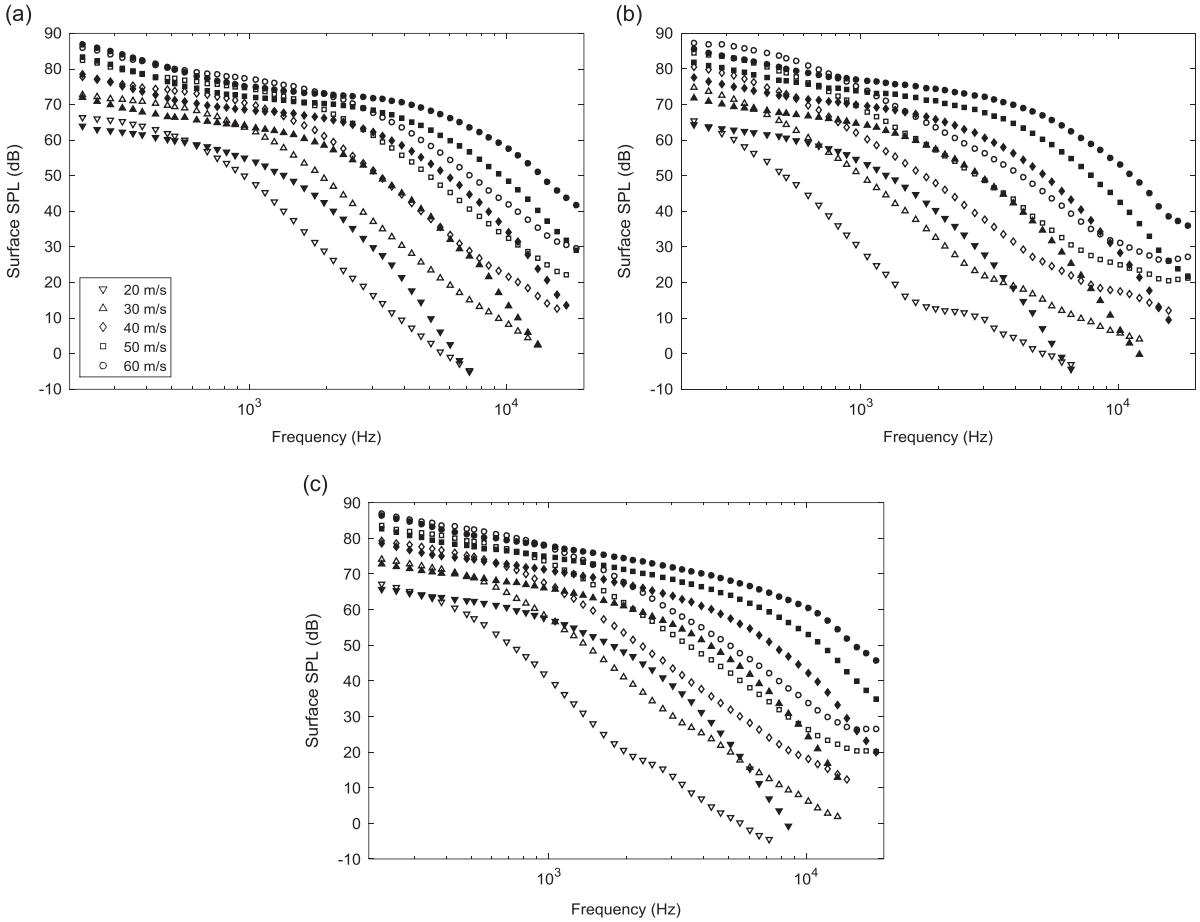

Fig. 15. Surface pressure fluctuations measured with fabric canopy 5 shrouding (a) the smooth wall, and the (b) hemispherical and (c) sandpaper rough surfaces (open symbols). Solid symbols show pressure fluctuation spectra recorded for each of these surfaces, respectively, without canopy.

layer portion of the wall-jet flow, as opposed to the much larger turbulent structures present in the upper shear-layer portion of the flow. This might be expected as the height of canopy (approximately 4 mm) is well-embedded in the boundary layer (with thickness of approximately 16–17 mm).

With the surface pressure fluctuations attenuated one might expect an effect upon the noise radiated from the rough surfaces, depending on the amount of sound produced by the canopy itself. The self-noise of the canopy can be judged in Fig. 16a, which compares noise levels with the canopy draped over the smooth wall to background levels in the facility. Audible canopy noise is seen at high frequencies, above 5 kHz at 60 m/s, with the signal-to-noise ratio becoming larger as the frequency is increased. As seen in Fig. 19, comparison with results obtained using the other fabrics shows an increase in canopy self-noise with filament diameter and the degree to which the filaments are perpendicular to the flow. This is, of course, consistent with the stealth of the owl, given the fineness of the fibers that form its down and their alignment with the flow direction in the down canopy.

The canopy has a mixed effect on the sound radiated from the rough surfaces (Fig. 16b and c). At mid-range frequencies the canopy actually reduces the roughness noise. Greater reductions are observed when the canopy is placed over sandpaper as compared to the hemispherical roughness case, and the largest attenuation is approximately 5 dB near 5 kHz for the 60 m/s case. At high frequencies the canopy self-noise increases far-field sound levels over the rough surface alone. The increase in sound levels is smallest for the sandpaper rough surface.

4.3. Unidirectional canopies

The results of the fabric canopy experiment showed that, in general, far-field noise increased as the fabrics featured cross-threads placed at higher angles relative to the flow direction. As such, a new hypothesis was developed which stated that if these cross-threads were to be removed, leaving a canopy with only fibers oriented in the flow direction, then the majority of the canopy self-noise could be eliminated, while the noise-canceling aspects of the canopy could be retained. This led to the development of a unidirectional canopy, featuring faired thread supports upstream and downstream of the roughness fetch. There was concern that the presence of these supports would substantially alter the flow over the

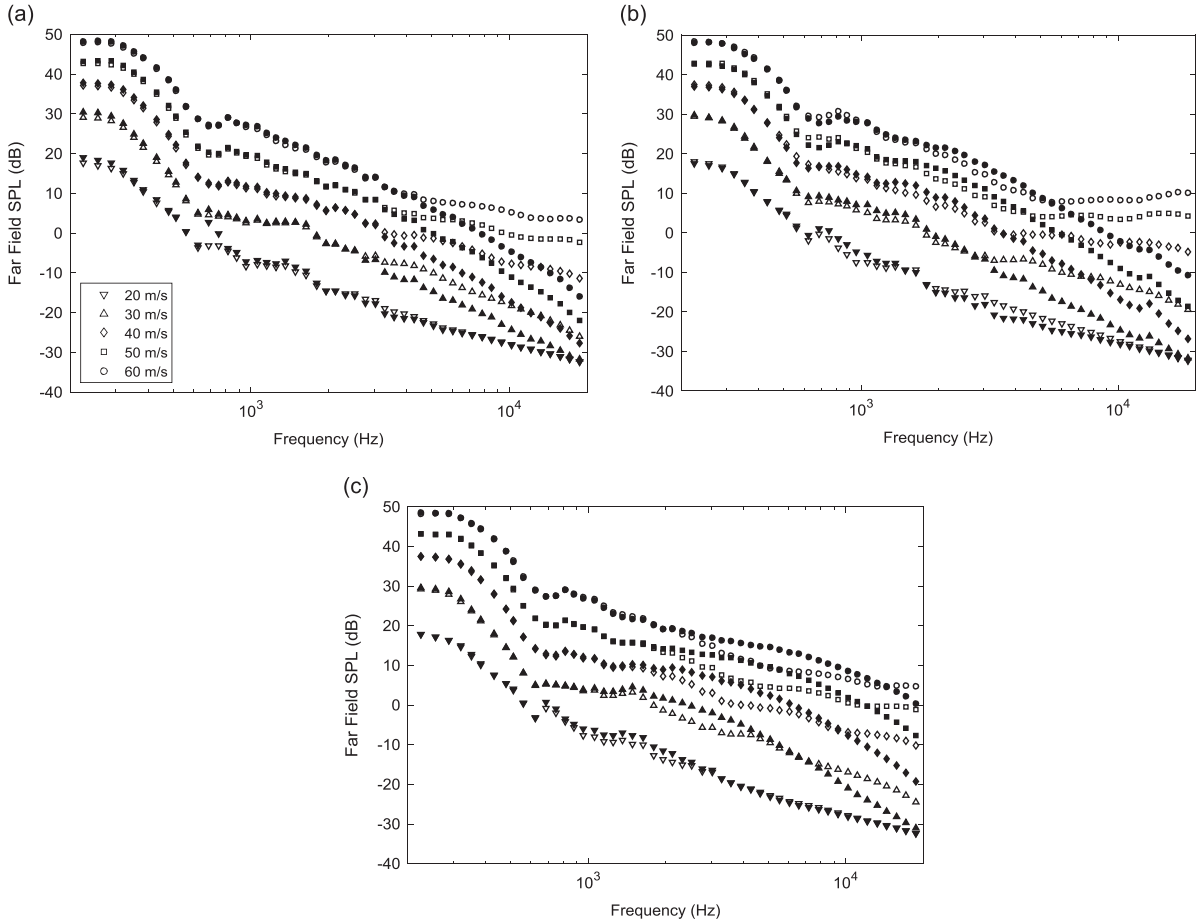

Fig. 16. Noise measurements made with fabric canopy 5 shrouding (a) the smooth wall, and the (b) hemispherical and (c) sandpaper rough surfaces (open symbols). Solid symbols show sound levels recorded for each of these surfaces, respectively, without canopy.

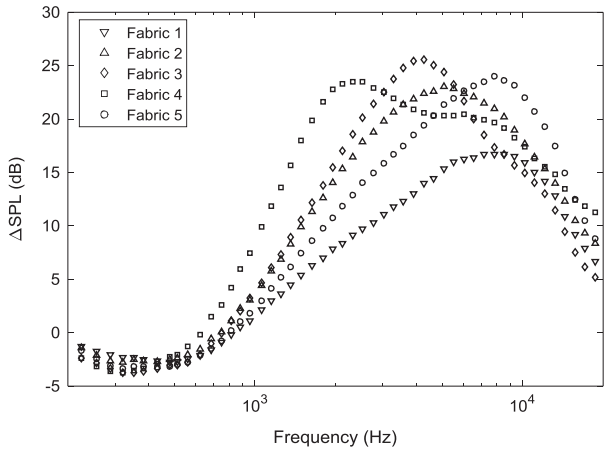

Fig. 17. Attenuation of surface pressure fluctuations for each canopy over 3 mm roughness at $U_j = 60$ m/s.

sandpaper or canopy, thereby affecting the acoustic behavior of these items. Therefore, before presenting data for the effects of the unidirectional canopies, results are given that reveal the comparatively minor effects of the thread supports on the radiated noise and surface pressure field. Fig. 20 shows the isolated effect of the thread supports compared to the background levels of the tunnel without roughness. The supports raised the far-field levels by approximately 1–2 dB above the background across the frequency spectrum. It is hypothesized that the majority of the far-field effect is due to scattering of the nozzle noise from the curved surface of the support, and not to any additional aerodynamic source.

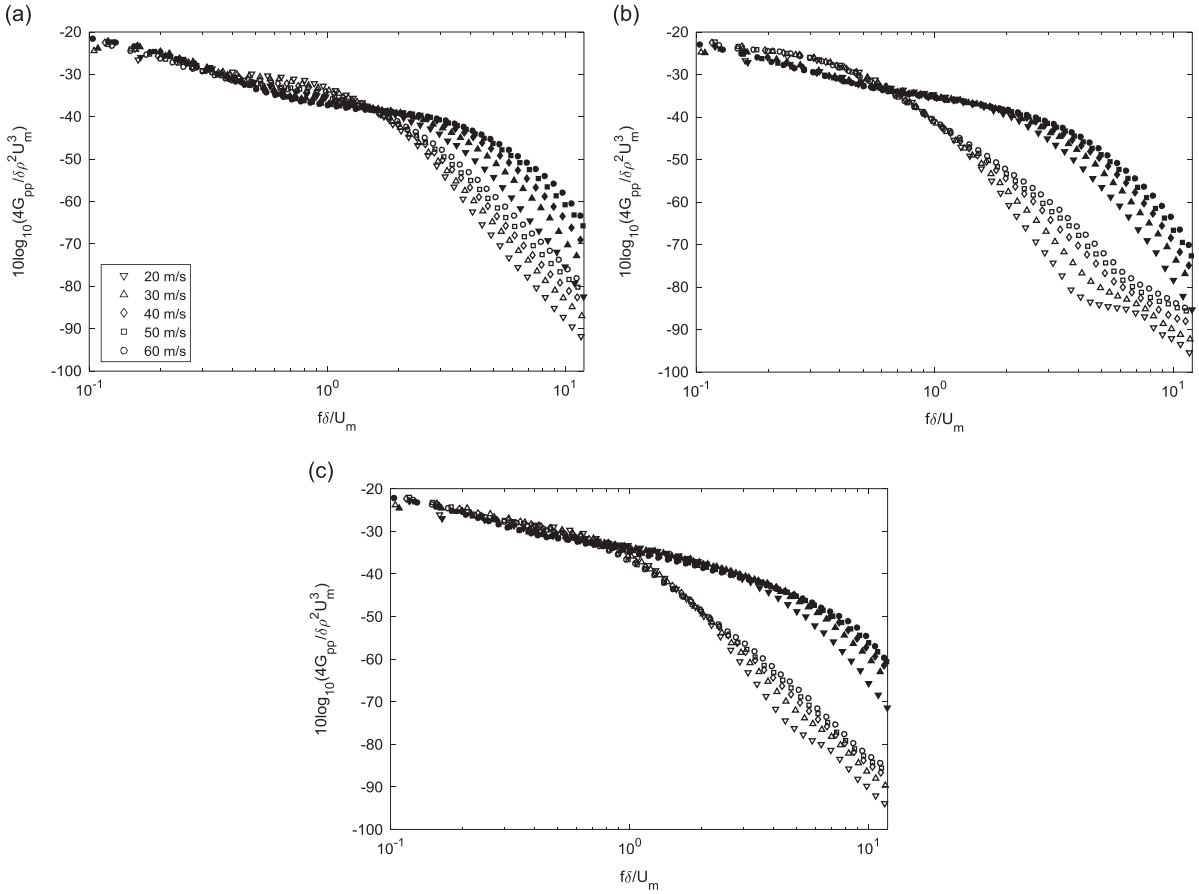

Fig. 18. Scaled surface pressure fluctuations measured with fabric canopy 5 shrouding (a) the smooth wall, and the (b) hemispherical and (c) sandpaper rough surfaces (open symbols). Solid symbols show pressure fluctuation spectra recorded for each of these surfaces, respectively, without canopy.

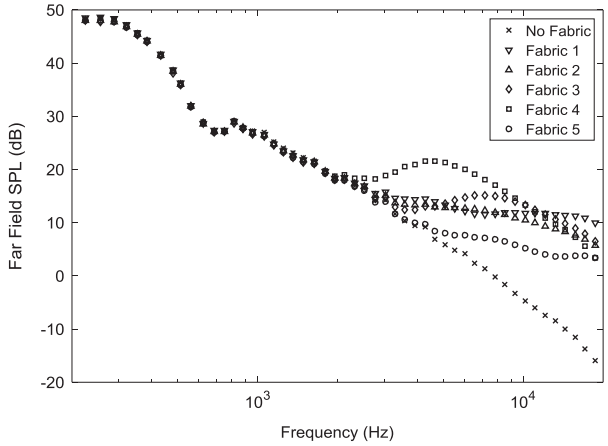

Fig. 19. Comparison of far-field noise for each fabric suspended above a clean wall at U_j=60 m/s, illustrating the self-noise of each fabric.

Fig. 20 also shows the effect of the supports on the surface pressure spectrum at the three streamwise locations. The most upstream location (Fig. 20b) shows an increase in magnitude across the frequency range for all speeds, with the greatest increase at 20 m/s. This increase could be caused by local separation at the down-slope of the support, which decreases in severity with increasing Reynolds number. Interestingly, the center location (Fig. 20c) shows almost no effect from the addition of the supports. The downstream location (Fig. 20d) experiences an increase in low and mid frequency levels, which could be due to slight upstream influence of the downstream support. Overall, although there are some noticeable effects from the supports, the differences are minor and do not hinder the canopy measurements.

Fig. 21 shows the effect of placing sandpaper roughness between the mounts, again without a canopy present. The near- and far-field effects are nearly identical to the effect of sandpaper seen previously (as in Figs. 13 and 14). The presence of the

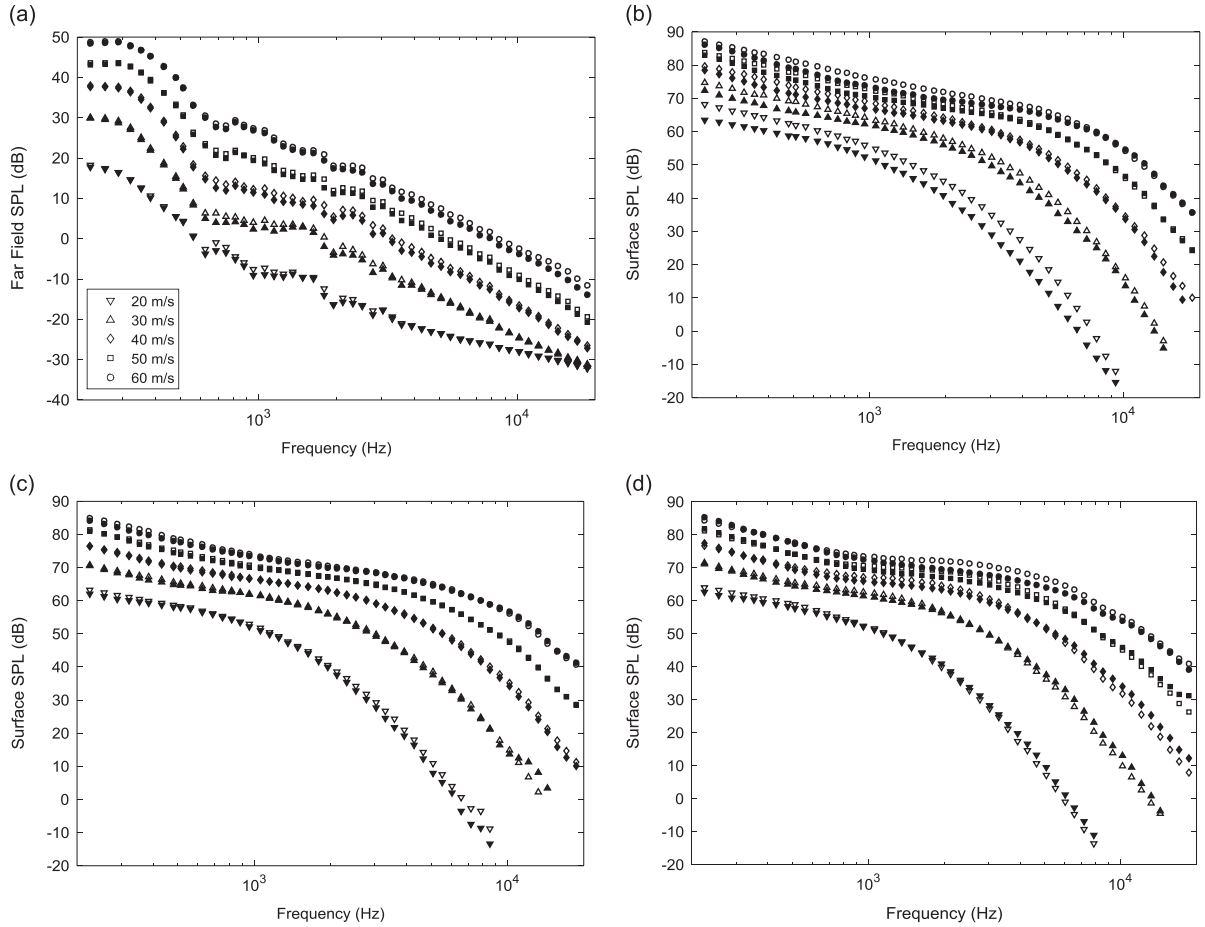

Fig. 20. Measurements of (a) far-field sound and surface pressure measurements from (b) upstream, (c) middle, and (d) downstream microphones showing the effects of adding the mounts (open symbols) to the clean configuration (solid symbols).

mounts does not significantly alter the noise generation of the sandpaper, so the effects of adding a canopy should not be influenced by the support structure.

Fig. 22a shows the far-field effects of stringing the thinnest fibers over the sandpaper roughness. At higher flow speeds, far-field sound levels were reduced by as much as 6 dB at higher frequencies. At low flow speeds, the far-field results are distorted somewhat by the noise floor of the microphones, but even so, a noise reduction is observed. Fortunately, these reductions are achieved without the large increases in high-frequency noise observed with the mesh canopies.

Fig. 22 also shows the acoustic results for unidirectional canopies with different thread diameters, but the same open-area ratio of 70 percent. As the diameter of the thread (and the spacing between the fibers) increases, the canopy appears to become less effective at reducing the far-field noise. This may be explained by the differences in the attenuation of the surface pressure fluctuations produced by adding the canopy in each case, shown in Fig. 23. Fig. 23 shows the difference in the measured surface pressure spectra on a dB scale for each of the three canopies, sensed by the microphone at the center of the canopy. Several patterns emerge in looking at the complete data set. There appears to be a strong Reynolds number effect on the attenuation. In general, as the flow speed over the canopy increases, the attenuation decreases, especially for the thinnest canopy. For the case of the thinnest canopy and a jet speed of 20 m/s, the attenuation is highest.

At a fundamental level, this result points to physical scale as the dominant factor in the effectiveness of the canopy. The distance between the fibers likely plays an integral role by determining the scale of eddies which may pass through the canopy unhindered, which may be distorted or broken up upon passing through, and which may stay above the canopy altogether. At an extreme level, one could think of a canopy with many microscopic fibers, with microscopic areas between them. In this case, even with the same open area ratio of 70 percent, the fibers would physically prevent all but the very smallest turbulent eddies to pass through unhindered, and viscous effects would dominate at this scale to dampen these eddies. This situation closely resembles that of owls' wings, and their slow flight speeds and microscopic hairs likely combine to produce extremely efficient pressure fluctuation attenuation at the surface.

Another pattern seems to be that the attenuation develops as it moves downstream. This trend is seen for all three canopies, but is most evident in the data corresponding to canopy 3. Fig. 24 shows the surface pressure attenuation beneath canopy 3 sensed by each of the three microphones underneath. This may be the sign of a pseudo-viscous damping

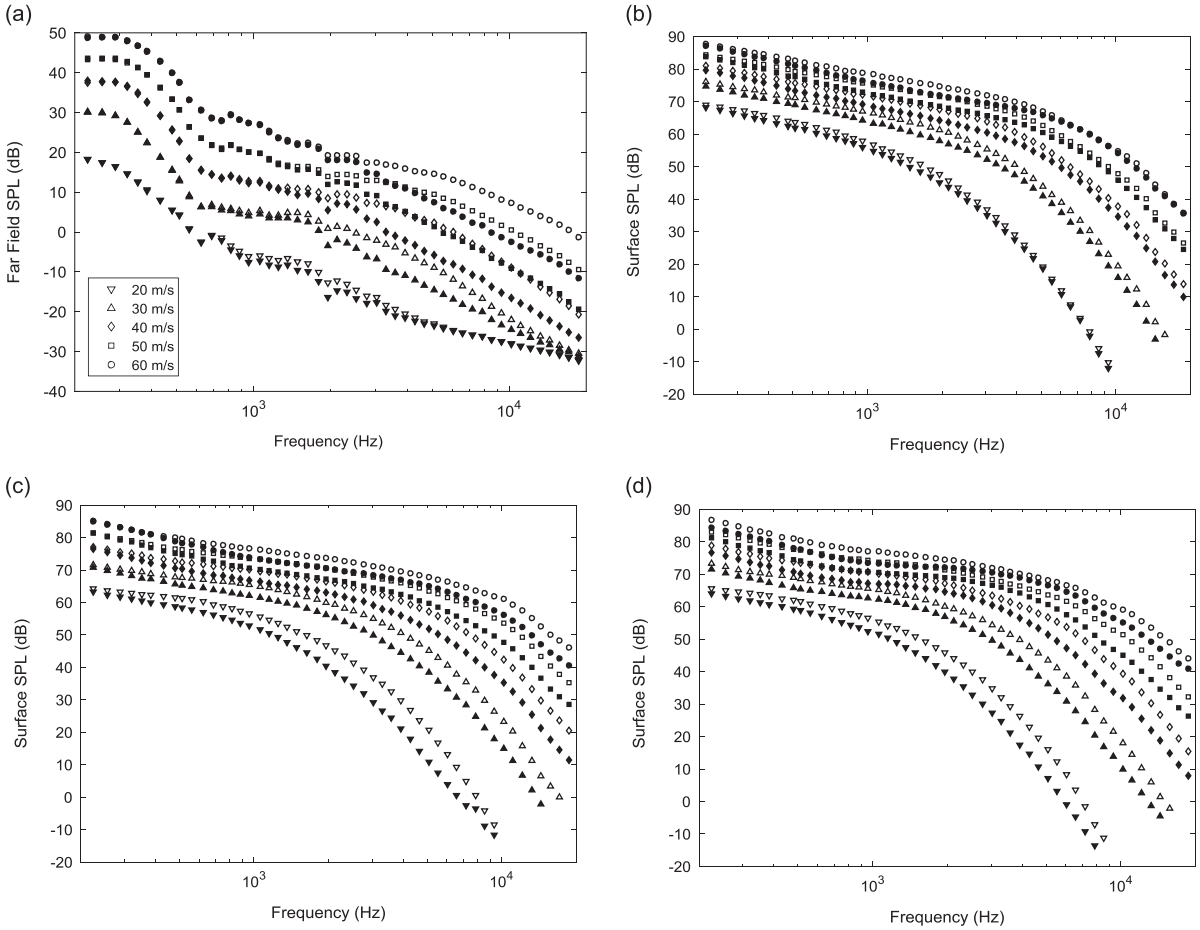

Fig. 21. Measurements of (a) far-field sound and surface pressure measurements from (b) upstream, (c) middle, and (d) downstream microphones showing the effects of adding sandpaper roughness (open symbols) to the canopy mounts (solid symbols).

mechanism which influences the flow as it moves downstream beneath the canopy. This damping mechanism may be the result of the turbulent eddies' interactions with the canopy itself, or the fact that the small-scale eddies beneath the canopy no longer receive energy from any large-scale turbulent eddies such that any remaining turbulent energy is quickly dissipated, or a combination of these two phenomena.

Fig. 25 shows the comparison of far-field noise produced with and without sandpaper roughness beneath canopy 1. Strangely, the effect of the sandpaper seems to be minimal. The levels are only about 1–2 dB higher when sandpaper is included in the test, which is nearly within the uncertainty of the measurements. This means that the sandpaper is making very little noise at all while covered with the canopy, and any noise above background levels is due primarily to the canopy itself. This is consistent with the fact that the surface pressure fluctuations have been attenuated by the canopy, which means that relatively little turbulent energy is available to be scattered into the far-field by the roughness. However, the canopy itself can act as a scattering mechanism given its exposure to the undisturbed flow above.

5. The mixing layer instability as a model of surface pressure reduction

We now wish to propose a tentative model to explain features of the reduction in unsteady surface pressure levels which result from introduction of the unidirectional canopy. We note that in the surface pressure fluctuation attenuation plots of Fig. 23, the shapes of the curves are remarkably similar to each other. In each case there is a definite maximum reduction, whose amplitude decreases with U_{jet}. Our inspiration for modelling this effect comes from studies of air flow over forest canopies (see references [16,17] for a review), where it is well known that the drag of the canopy retards the lower portion of the atmospheric boundary layer and creates thin shear layers above the canopy, which undergo a classical mixing-layer instability [18]. We hypothesize that the introduction of the fabric canopy has the same effect on the wall-jet boundary layer.

The next step in our argument is to note that shear instability leads to exponential growth in the streamwise direction, but exponential decay in the direction transverse to the shear layer. This effect can be seen most simply in the case of Helmholtz instability of a vortex sheet: for a shear of strength U at frequency ω, the Kelvin-Helmholz wave has exponential

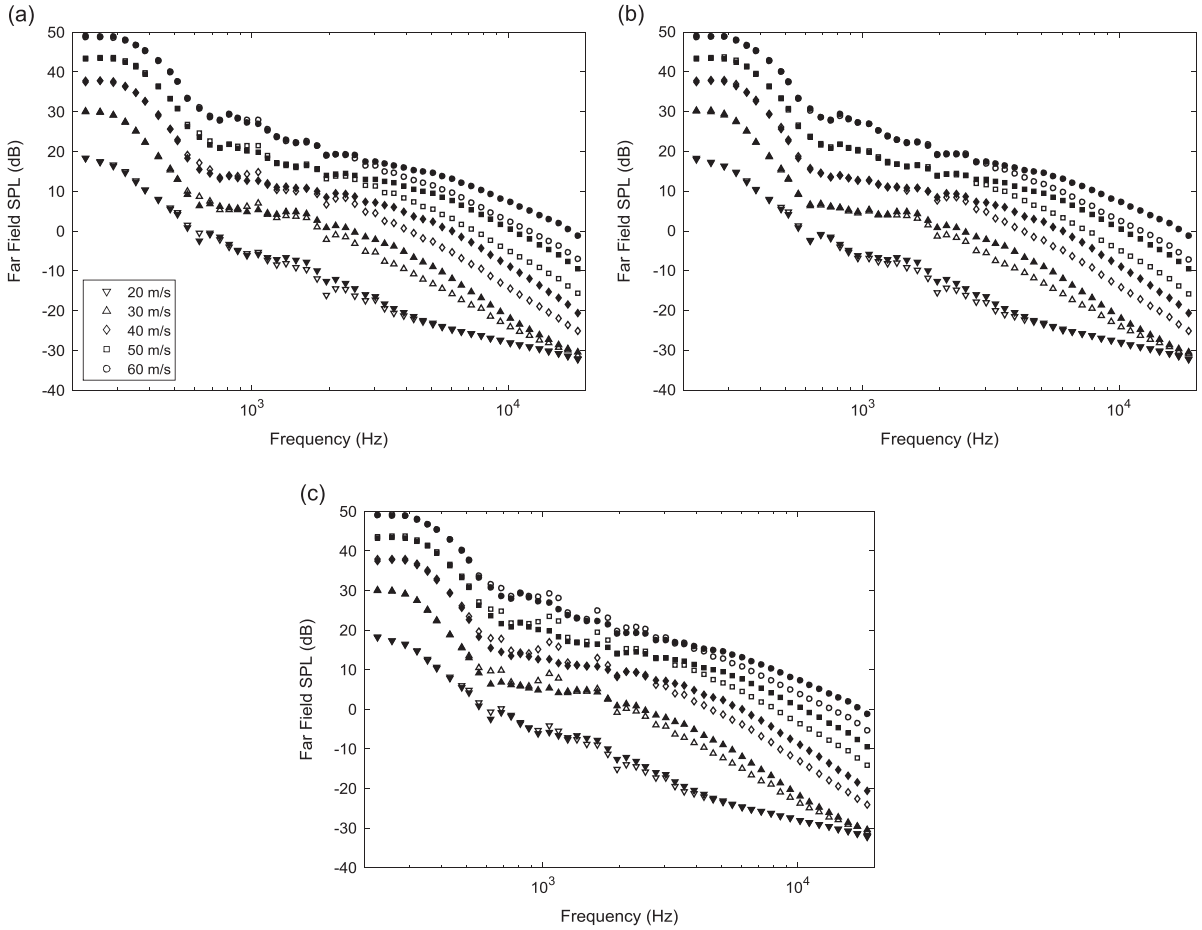

Fig. 22. Measurements of far-field noise from sandpaper covered with canopies (a) 1, (b) 2, and (c) 3 (open symbols) compared with those from uncovered sandpaper (solid symbols).

spatial growth rate ω/U and decays with transverse distance at exponential decay rate ω/U. The vortex sheet is of course unstable at all frequencies and its spatial growth rate is unbounded. However, a genuine, finite-thickness, shear layer will typically only be spatially unstable over a finite frequency range, and will typically have a definite frequency at which a maximum growth rate (and therefore by analogy with Kelvin-Helmholtz a maximum transverse decay rate) occurs. These features are very much in tune with the features of the experimental results described in the first paragraph. Our hypothesis for the effect of the canopy is therefore as follows: the canopy introduces a mixing layer, which leads to instability waves (as nascent turbulent eddies), which, due to the presence of the canopy, are lifted higher above the solid boundary than they would have been without the canopy present. The pressure footprint of these eddies on the solid surface is therefore substantially reduced, by both the transverse exponential decay effect of the instability wave and by their greater stand-off from the wall.

In order to investigate our hypothesis further, we now consider the stability of a simple linear shear layer above the canopy, and compute the spatial growth rates of the system for varying frequency, which we will then use to infer the surface pressure response. Specifically, we investigate the spatial instability of the linear mixing layer, with a base flow. Velocities and lengths are non-dimensionalized in terms of the free-stream velocity U_s and the layer thickness δ. In terms of the wall-normal coordinate y, the mixing layer velocity profile is written as

$$U(y) = \begin{cases} 0, & y < 0, \\ \dfrac{U_s y}{\delta}, & 0 \le y \le \delta, \\ U_s, & y > \delta. \end{cases} \tag{5.1}$$

To determine the spatial stability of the base flow $U(y)$ we first assume wavelike, two-dimensional velocity and pressure perturbations of the form

$$[\tilde{u}(x,y,t), \tilde{v}(x,y,t), \tilde{p}(x,y,t)] = [u(y), v(y), p(y)]e^{ikx - i\omega t}. \tag{5.2}$$

Here x is the streamwise coordinate, $\omega \in \mathbb{R}$ is the temporal frequency, $k \in \mathbb{C}$ is the streamwise wavenumber, $\tilde{u}$ and $\tilde{v}$ are the

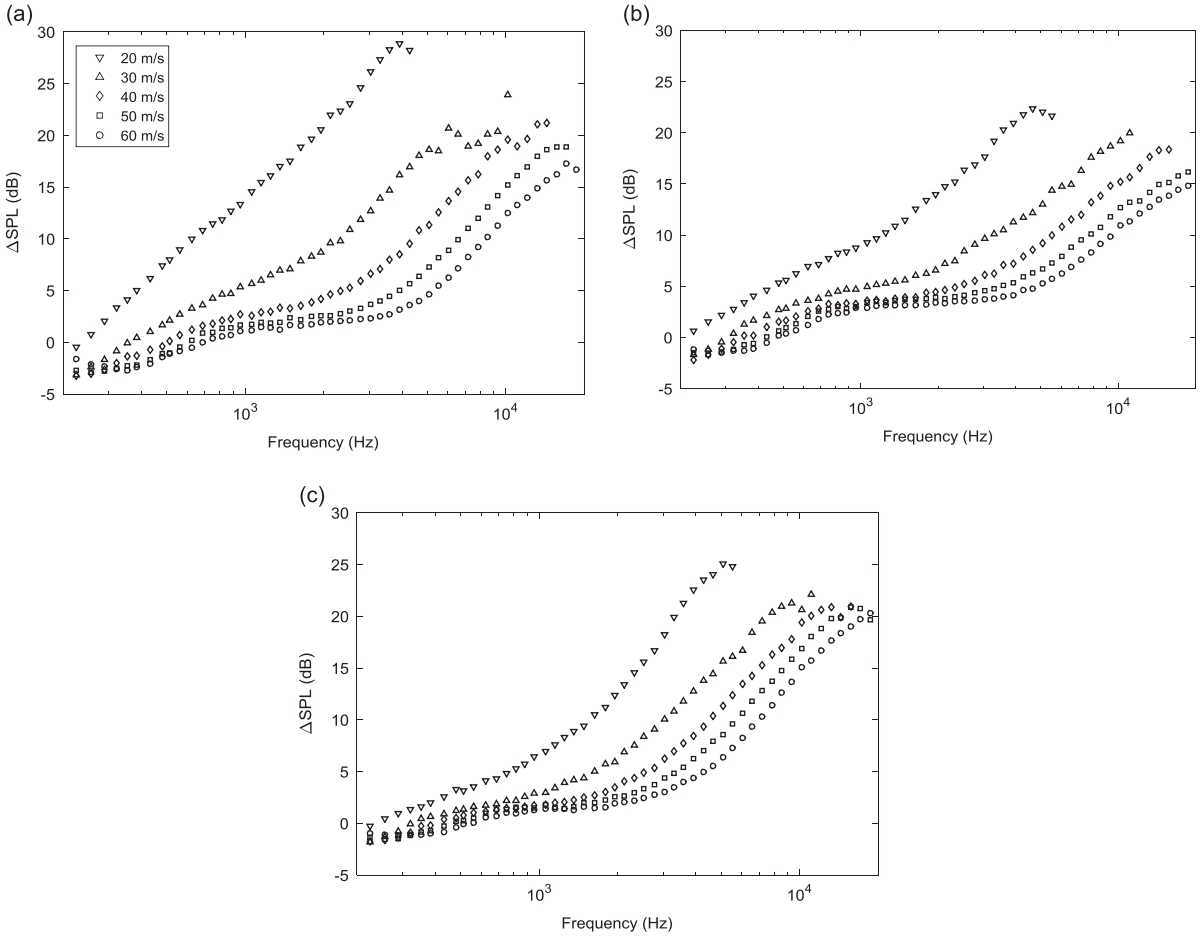

Fig. 23. Surface pressure attenuation due to canopy (a) 1, (b) 2, and (c) 3 shrouding sandpaper roughness sensed by the center microphone.

streamwise and wall-normal velocities, respectively, and $\tilde{p}$ is the pressure perturbation. Perturbations of this form satisfy the reduced Rayleigh equation

$$\left(D^2 - k^2\right)v = 0, \tag{5.3}$$

where $D = d/dy$. This simplification allows us to determine an exact dispersion relation $d(\omega, k, b, \delta)$. Assuming a wall-normal velocity perturbation profile which satisfies the Rayleigh equation in each of the three mean profile regions gives

$$v(y) = \begin{cases} Ae^{ky}, & y < 0, \\ Be^{-ky} + Ce^{ky}, & 0 \le y < \delta, \\ De^{-ky}, & y > \delta, \end{cases} \tag{5.4}$$

for $\mathrm{Re}\{k\} > 0$. We impose continuity of the wall-normal velocity at $y = \delta$. At $y = 0$ we introduce the following condition to account for the disruption of wall-normal momentum caused by the canopy

$$v_+ / v_- = \gamma, \quad 0 \le \gamma \le 1. \tag{5.5}$$

In Eq. (5.5), v_+ and v_- denote the wall-normal velocities above and below the canopy at $y = 0$, respectively. For $\gamma = 0$ we have $v_+ = 0$, and the canopy behaves as a solid wall. For $\gamma = 1$ we have $v_+ = v_-$ and there is perfect continuity across the canopy. Therefore γ acts as a homotopy parameter between these two cases. We thus identify γ as a parameterization of the open-area ratio of the canopy. Since this quantity is held constant at 0.7 for all canopies experimentally tested, we fix $\gamma = 0.7$ in our calculations, unless otherwise specified.

In addition to the conditions on v at $y = 0, \delta$, we impose continuity of the pressure perturbation p at the same wall-normal locations $y = 0, \delta$. Pressure continuity requires, with $s = 0, \delta$

$$(\omega - kU_s)kv' + kU_s' v|_{y=s+} = (\omega - kU_s)kv' + kU_s' v|_{y=s-}, \tag{5.6}$$

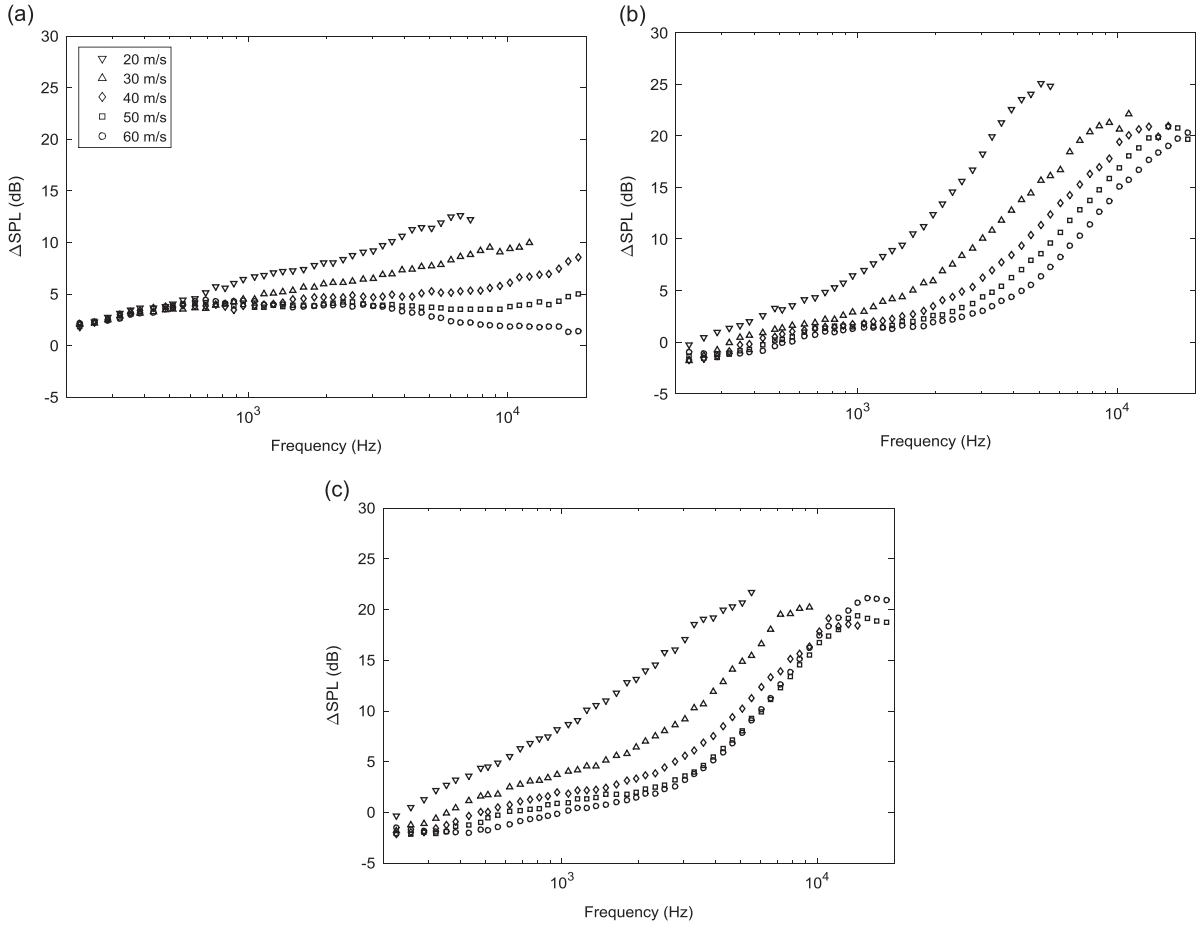

Fig. 24. Surface pressure attenuation due to canopy 3 shrouding sandpaper roughness sensed by microphone (a) 1, (b) 2, and (c) 3.

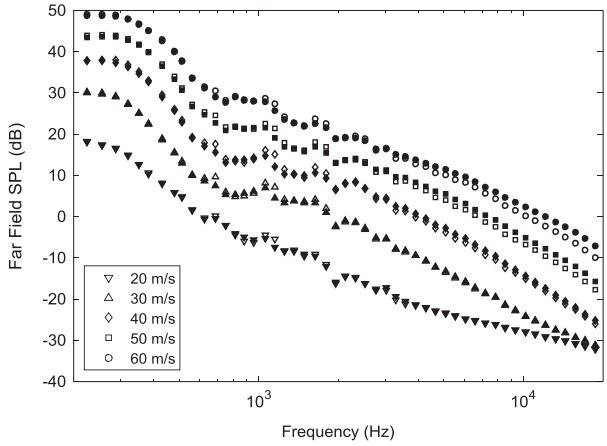

Fig. 25. Measurements of far-field noise showing the difference in levels between the canopy-covered sandpaper (solid symbols) and canopy without sandpaper (open symbols).

The application of the above conditions allows us to eliminate the amplitudes A, B, C, D and derive a nonlinear dispersion relation for complex k. The two conditions at $y = 0$ give

$$B + C = \gamma A, \tag{5.7}$$

$$B(U_s - \omega\delta) + C(U_s + \omega\delta) = \omega\delta A. \tag{5.8}$$

The conditions at $y=\delta$ give

$$Be^{-k\delta}+Ce^{k\delta}=De^{-k\delta}, \tag{5.9}$$

$$Be^{-k\delta}(U_s-\delta(\omega-kU_s))+Ce^{k\delta}(U_s+\delta(\omega-kU_s))=\delta De^{-k\delta}(\omega-kU_s). \tag{5.10}$$

On eliminating the amplitudes in Eqs. (5.7)–(5.10), we arrive at the following dispersion relation, which we express in terms of the non-dimensional quantities $K=k\delta$ and $\Omega=\omega\delta/U_s$,

$$d(\Omega,K,\gamma)=2(1+\gamma)\Omega^2-\{(1+\gamma)(1-2K)-(1-\gamma)e^{-2K}-2\gamma\}\Omega+\gamma(2K-1+e^{-2K}). \tag{5.11}$$

Complex solutions K of $d(\Omega,K,\gamma)=0$ are found via Newton iteration. Unstable solutions of this equation exist in the range $0<\Omega<\gamma/(1+\gamma)$. We plot instability curves for various γ in Fig. 26.

The theoretical framework presented above is now used to reproduce, as far as possible, the experimentally observed SPL attenuation curves induced by unidirectional canopy 1 from Fig. 23(a). In order to do this, we will make sensible choices for some of the parameters in our model which can be estimated, such as the jet speed. However, other parameters are harder to estimate, and instead we will try to tune the free parameters in order to try and fit the results. Therefore, we are not attempting, at this stage, to make a complete quantitative prediction without the need for any fitting. Rather, we wish to determine whether the instability model is capable of recovering the features seen in experiment.

En route to determining a comparison to the SPL data, we derive an expression for the pressure drop across the mixing layer. Using our expressions for the wall-normal eigenfunctions above, we arrive at the following relation

$$\frac{p(\delta)}{p(0)}=\frac{2\gamma(K-\Omega)^2e^{-K}}{\Omega(2(K-\Omega)-1+e^{-2K})}. \tag{5.12}$$

We then suppose that due to the wall-normal, exponential decay effect of the unstable wave, the SPL attenuation is related to the linear instability in the following manner

$$\Delta\mathrm{SPL}=20\log_{10}\left(e^{-\mathrm{Im}\{K\}D}\left|\frac{p(\delta)}{p(0)}\right|\right). \tag{5.13}$$

The constant D in Eq. (5.13) is the pressure instability length scale, i.e. the height above the canopy where the least stable linear wave is located in order to fix the level of attenuation observed in the experiment.

Experimental results indicate the velocity just above the canopy to be about one third of the total jet velocity. Identifying fluid velocity at the lower part of the mixing layer ($y=0$) with the velocity just above the canopy, and assuming that in the turbulent dynamics shear layers exist which shear from the maximum jet velocity we choose the velocity drop across the mixing layer to be $U_s=U_{\mathrm{jet}}/3$. Frequencies f in Hertz can then be mapped to non-dimensional frequencies using the relation

$$\omega=\frac{2\pi f\delta}{U_s}. \tag{5.14}$$

We use the experimentally observed frequency range to determine the layer thickness δ for each jet velocity. Results of fitting SPL attenuation and the layer thicknesses are included in Figs. 27 and 28.

The good agreement between the experimental and theoretical attenuation curves presented in Fig. 27 suggests that the canopy instability model is capable, for suitably chosen parameter values, of capturing aspects of the pressure attenuation, specifically at higher jet velocities. The parameter values of the model are reported in Fig. 28, where we see a trend of approximately constant layer thickness δ, and decreasing length scale $D\delta$ with increasing jet velocity. From these results we

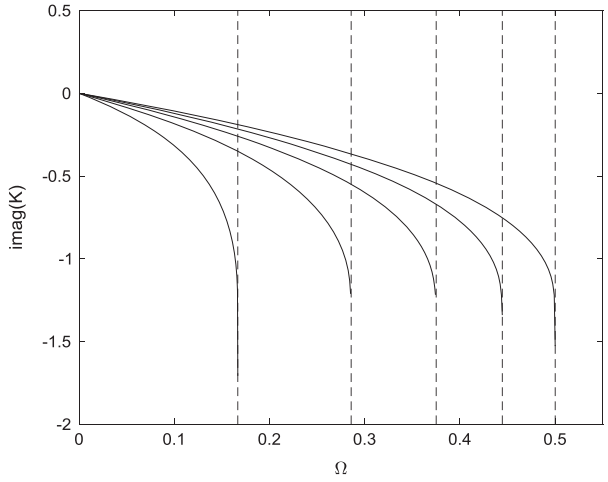

Fig. 26. Mixing layer instability growth rates, for γ = 0.2, 0.4, 0.6, 0.8, 1. The dashed curves are $\Omega=\gamma/1+\gamma$.

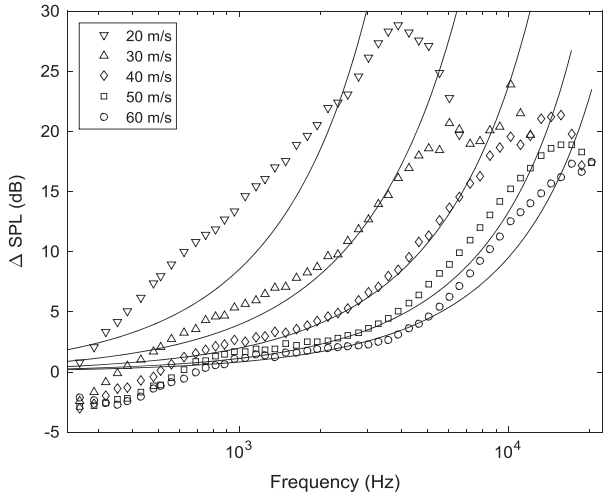

Fig. 27. Comparison of experimentally measured surface pressure attenuation and theoretical prediction.

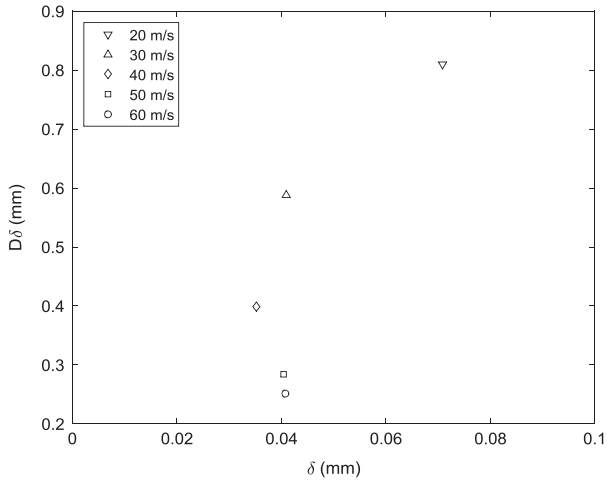

Fig. 28. Plots of dimensional model parameters δ and $D\delta$ for given jet speeds. There is an approximate trend of constant layer thickness δ, and decreasing length scale $D\delta$ with increasing jet velocity.

can conclude that a finely structured mixing layer instability approximates the attenuation trend until a maximum reduction is reached at high frequency and any attenuation is shut off by some other mechanism. Elucidation of this latter mechanism is a matter for further research.

6. Conclusions

Many species of owl are able to hunt in effective silence, a feat which is believed to be linked to three unique physical attributes: a comb of evenly-spaced bristles along the wing leading-edge; a compliant and porous fringe of feathers at the trailing-edge; and a velvety down material distributed over the upper wing surface. This paper has focused on the last of these mechanisms which is being investigated through experiments made on surfaces that mimic some geometrical features of the owl-down, as well as theoretical analysis of the aeroacoustics of canopy coverings and of flexible hairs.

Microscope photographs of the down show that it consists of hairs that form a structure similar to that of a forest. The hairs initially rise almost perpendicular to the feather surface but then bend in the flow direction over to form a canopy with an open area ratio of about 70 percent. Experiments have been performed to examine the aeroacoustic effects of vertical filaments and by the large open area ratio fabric canopy suspended above a surface. The canopy is found to dramatically reduce pressure fluctuations on the underlying surface, in a manner that is found to be consistent the theory of flows over and through vegetation. While the canopy can produce its own sound, particularly at high frequencies, the reduction in surface pressure fluctuations can reduce the noise scattered from an underlying rough surface, particularly in the mid-frequency range. The use of a canopy with fibers oriented only in the flow direction does not produce the high-frequency self-noise of the fabric canopies, but surface pressure fluctuations are still suppressed. The effectiveness of the

canopies in reducing the surface pressure fluctuations and far-field noise is primarily dependent on the physical spacing between the fibers of the canopy, with more closely spaced fibers producing more signal attenuation.

Acknowledgments

The authors would like to thank the Office of Naval Research, in particular Drs. Ki-Han Kim and Woei-Min Lin, for their support under grants N00014-13-1-0244, N00014-14-1-0242, and N62909-12-1-7116 (NICOP). IAC and JWJ are grateful to Prof. Raymond Goldstein for access to his photography equipment to examine the structure of owl down barbules. The assistance of Mr. Nathaniel Ross, Mrs. Katelyn McCormick, Mr. Daniel Grohol, and Mr. Jeffrey Gomes in the preparation of the surfaces for wind tunnel testing and in the performance of those tests is much appreciated.

References

[1] R.R. Graham, The silent flight of owls, *Journal of the Royal Aeronautical Society* 38 (1934) 837–843.
[2] R.A., Kroeger, H.D., Gruschka, T.C., Helvey, Low speed aerodynamics for ultra-quiet flight, Tech. Rep. AFFDL-TR-71-75, Air Force Flight Dynamics Laboratory, Wright-Patterson AFB, 1972.
[3] A.S. Hersh, P.T. Soderman, R.E. Hayden, Investigation of acoustic effects of leading-edge serrations on airfoils, *Journal of Aircraft* 11 (4) (1974) 197–202.
[4] J.W. Jaworski, N. Peake, Aerodynamic noise from a poroelastic edge with implications for the silent flight of owls, *Journal of Fluid Mechanics* 723 (2013) 456–479.
[5] J. W. Jaworski, N. Peake, Parametric guidance for turbulent noise reduction from poroelastic trailing edges and owls, *Proceedings of the 19th AIAA/CEAS Aeroacoustics Conference*, Berlin, AIAA-2013-2007, 2013.
[6] G.M. Lilley, A study of the silent flight of the owl, *Proceedings of the 4th AIAA/CEAS Aeroacoustics Conference, Toulouse*. AIAA Paper 1998-2340, 1998.
[7] T. Bachmann, S. Klan, W. Baumgartner, M. Klaas, W. Schroder, H. Wagner, Morphometric characterization of wing feathers of the barn owl Tyto alba pratincola and the pigeon Columba livia, *Frontiers in Zoology* 4 (23) (2007).
[8] T. Bachmann, *Anatomical, Morphometrical And Biomechanical Studies of Barn Owls' and Pigeons' Wings, Ph.D. dissertation*, RWTH Aachen University, Aachen, Germany, 2010.
[9] K. Chen, Q. Liu, G. Liao, Y. Yang, L. Ren, H. Yang, X. Chen, The Sound Suppression Characteristics of Wing Feather of Owl (Bubo bubo), *Journal of Bionic Engineering* 9 (2012) 192–199.
[10] S. Klan, T. Bachmann, M. Klaas, H. Wagner, W. Schroder, Experimental analysis of the flow field over a novel owl based airfoil, *Experiments in Fluids* 46 (2009) 975–989.
[11] S. Klan, S. Burgmann, T. Bachmann, M. Klaas, H. Wagner, W. Schroder, Surface structure and dimensional effects on the aerodynamics of an owl-based wing model, *European Journal of Mechanics B/Fluids* 33 (2012) 58–73.
[12] W.N. Alexander, *Sound from Rough Wall Boundary Layers, Ph.D. dissertation*, Virginia Polytechnic Institute and State University, Blacksburg, Virginia, USA, 2011 avail ⟨http://scholar.lib.vt.edu/theses/available/etd-10112011-085924/⟩.
[13] W.J. Devenport, D.L. Grissom, W.N. Alexander, B.S. Smith, S.A.L. Glegg, Measurements of roughness noise, *Journal of Sound Vibration* 330 (17) (2011) 4250–4273.
[14] I. Wygnanski, Y. Katz, E. Horev, On the applicability of various scaling laws to the turbulent wall jet, *Journal of Fluid Mechanics* 234 (1992) 669–690, http://dx.doi.org/10.1017/S002211209200096X.
[15] M. Awasthi, B. Bryan, W. Devenport, S. Glegg, Sound Radiation from Rounded Steps and Gaps, *Proceedings of the 19th AIAA/CEAS Aeroacoustics Conference*, Berlin. AIAA-2013-2048, 2013.
[16] E. De Langre, Effects of wind on plants, *Annual Review of Fluid Mechanics* 40 (2008) 141–168.
[17] J. Finnigan, Turbulence in plant canopies, *Annual Review of Fluid Mechanics* 32 (2000) 519–571.
[18] M.R. Raupach, J.J. Finnigan, Y. Brunet, Coherent eddies and turbulence in vegetation canpies: the mixing-layer analogy, *Boundary-Layer Meteorology* 78 (1996) 351–382.

Chapter 4

Bioinspired Trailing-Edge Noise Control

This chapter presents the development and testing of a new method of trailing edge noise control which followed from the work of the previous chapter. The work is published as "Bioinspired Trailing-Edge Noise Control" in the AIAA Journal (2017 55(3):740-754, DOI 10.2514/1.J055243).

The paper is reproduced with permission from AIAA.

AIAA JOURNAL
Vol. 55, No. 3, March 2017

Bioinspired Trailing-Edge Noise Control

Ian A. Clark,* W. Nathan Alexander,† and William Devenport‡
Virginia Polytechnic Institute and State University, Blacksburg, Virginia 24061
Stewart Glegg§
Florida Atlantic University, Boca Raton, Florida 33431
Justin W. Jaworski¶
Lehigh University, Bethlehem, Pennsylvania 18015
and
Conor Daly** and Nigel Peake††
University of Cambridge, Cambridge, England CB3 0WA, United Kingdom

DOI: 10.2514/1.J055243

Strategies for trailing-edge noise control have been inspired by the downy canopy that covers the surface of exposed flight feathers of many owl species. Previous wind-tunnel measurements demonstrate that canopies of similar characteristics can reduce pressure fluctuations on the underlying surface by as much as 30 dB and significantly attenuate roughness noise generated by that surface. In the present work, surface treatments are designed to replicate the effects of the canopy in a form suitable for application to an airfoil. These treatments are installed directly upstream of the trailing edge to modify the boundary-layer turbulence before acoustic scattering by the edge. Over 20 variants of these designs have been tested by performing aeroacoustic wind-tunnel measurements on a tripped DU96-W180 airfoil at chord Reynolds numbers of up to 3 million. Compared with the unmodified airfoil, the treatments provided up to 10 dB of broadband attenuation of trailing-edge noise. The effectiveness of the treatment is not highly dependent on a particular geometry, but there appears to be strong potential for optimization. The surface treatments remain effective over an angle-of-attack range that extends over 9 deg from zero lift. Aerodynamic impact of the treatment appears minimal.

I. Introduction

THIS paper describes an experimental study aimed at trailing-edge noise control strategies inspired by the unique features found on the wings of owls that use acoustic stealth while hunting prey [1–3]. These features include a comb of evenly spaced bristles along the wing leading edge, a porous and elastic trailing-edge fringe, and fine downy hairs that coat the exposed surfaces of the flight feathers. Geyer et al. [4] sought to relate the fine downy coating to porosity of the wing by performing experiments involving aerodynamic and acoustic testing of airfoils manufactured entirely of porous material. Their results showed that porous airfoils can be effective for trailing-edge noise reduction. However, the amount of noise reduction seemed to be a complex function of the resistivity of the material, and the aerodynamic performance suffered as resistivity decreased (i.e., as porosity increased). Jaworski and Peake [5,6] analyzed the trailing-edge condition and found that both porosity and flexibility weaken the well-known fifth-power dependency of the radiated acoustics of a trailing edge, with the greatest reduction in edge amplification occurring when these characteristics are combined. However, Jaworski and Peake [5,6] did not consider the effect of the downy hairs on the upper-wing surface. The purpose of this study is to investigate the importance of the downy hairs on the radiated noise and to develop noise control strategies that are inspired by their features.

The work described in this paper follows up on the study of Clark et al. [7], which considered the potential of a hairy surface to suppress noise generated by roughness lying underneath. It was shown that the downy hairs of the owl grow nearly perpendicular from the feather surface, but then lean over to form a canopy suspended about 0.5 mm above the feather substrate, with an open area ratio of about 70% (Fig. 1). Wall-jet wind-tunnel experiments were performed to examine the aeroacoustic effects of artificial canopies designed to mimic the effects of a canopy of this open area ratio on the surface pressure fluctuations and roughness noise generated by an underlying rough surface. Efforts included shrouding surfaces using canopies constructed from materials of the type used for wedding veils (Fig. 2a) and a series of canopies constructed using large numbers of parallel fibers, oriented in the flow direction just above the flow surface (Fig. 2b).

Measurements of surface pressure fluctuations underneath these canopies and of the roughness noise generated by surfaces shrouded by these canopies produced some surprising results. Even though the canopies had high open area ratios of about 70%, they attenuated surface pressure fluctuations underneath them by as much as 30 dB. The canopies were also found to attenuate broadband roughness noise, presumably because roughness noise is caused by the surface pressure fluctuations [8].

These unexpected findings spawned a new line of inquiry when it was realized that such a large reduction in surface pressure fluctuations might also serve to attenuate trailing-edge noise if a treatment replicating the effects of the canopy could be designed that was suitable for application to an airfoil. This paper describes an experimental study of a series of treatments inspired by this idea. An extensive series of wind-tunnel tests have been performed on a wind turbine airfoil at Reynolds numbers comparable to full scale. Measurements of the sound radiated by the airfoil trailing edge have been made both for the clean airfoil and with an extensive series of

Received 31 March 2016; revision received 29 July 2016; accepted for publication 5 September 2016; published online 9 December 2016.

*Graduate Student, Department of Aerospace and Ocean Engineering, Center for Renewable Energy and Aerodynamic Testing. Student Member AIAA.

†Assistant Professor, Department of Aerospace and Ocean Engineering, Center for Renewable Energy and Aerodynamic Testing. Member AIAA.

‡Professor, Department of Aerospace and Ocean Engineering, Center for Renewable Energy and Aerodynamic Testing. Associate Fellow AIAA.

§Professor, Department of Ocean and Mechanical Engineering. Associate Fellow AIAA.

¶Assistant Professor, Department of Mechanical Engineering and Mechanics. Senior Member AIAA.

**Research Associate, Department of Applied Mathematics and Theoretical Physics.

††Professor, Department of Applied Mathematics and Theoretical Physics. Member AIAA.

Fig. 1 Close-up view of a flight feather of a Great Gray Owl (Strix nebulosa) showing the canopy structure formed by the hairs.

trailing-edge treatments inspired by the owl down and the results of Clark et al. [7]. The effects of a broad range of treatment parameters were studied. We find that the treatment produces a broadband reduction in trailing-edge noise levels of up to 10 dB. The treatment remains surprisingly effective throughout a wide parameter range and is not highly dependent on a particular geometry, but there appears to be strong potential for optimization. The treatment is effective over an angle-of-attack range that extends to over 9 deg from the zero-lift condition.

II. Apparatus and Instrumentation

A. Stability Wind Tunnel

All tests were performed in the Virginia Tech Stability Wind Tunnel. This facility is a continuous, single return, subsonic wind tunnel with 7.3-m-long removable rectangular test sections of square cross section, 1.85 m on edge. The general layout is illustrated in Fig. 3.

The tunnel is powered by a 0.45 MW variable-speed dc motor, driving a 4.3 m-diam propeller that provides a maximum speed in the test section (with no blockage) of about 80 m/s. Ahead of the test section, flow is directed into a 5.5×5.5 m^2 settling chamber containing seven turbulence-reducing screens, each with an open area ratio of 0.6 and separated by 0.15 m. Flow exits this chamber through the 9:1 contraction nozzle, which further reduces turbulence levels and accelerates the flow to test speed as it enters the test section (Fig. 4).

Flow through the empty test section is both closely uniform and of very low turbulence intensity. Table 1 shows measurements from 2006 of freestream turbulence levels as a function of flow speed. Turbulence levels are as low as 0.016% at 12 m/s and increase gradually with flow speed. Choi and Simpson [9] measured the lateral integral scales of the streamwise velocity in both the horizontal L_z and vertical L_y directions. They found $L_z = 56$ mm for 15 m/s and 28 mm for 37.5 m/s, and $L_y = 122$ mm for 15 m/s and 25 mm for 37.5 m/s.

Figures 4 and 5 detail the stability wind-tunnel aeroacoustic test section used in the present study. This test section has acoustically treated lower and upper walls, consisting primarily of Kevlar-covered metal perforate panels backed by 0.45 m sound-absorbing foam wedges. The central 4.2 m length of both side walls are made from Kevlar panels placed under tension. The Kevlar contains the vast bulk of the flow and is almost transparent to sound [10]. Sound generated by a model placed at the center of the test section can therefore propagate out of the flow and into anechoic chambers placed on either side of the test section. These chambers, lined with 0.61 m foam wedges, are anechoic down to 190 Hz. The 4.2-m-long, 2.6-m-deep, and 3-m-high interior volume of the chambers allows for the

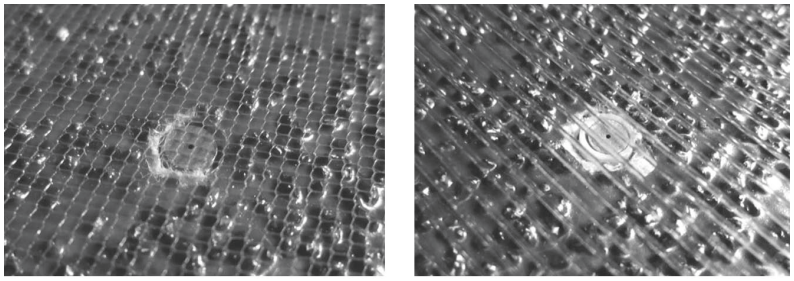

a) b)

Fig. 2 Example fabric canopy arrangements studied in the wind tunnel, shown shrouding a sandpaper-type rough surface: a) commercial wedding-veil-type fabric with multidirectional fibers; b) custom-designed unidirectional fiber fabric with fibers oriented only in the flow direction.

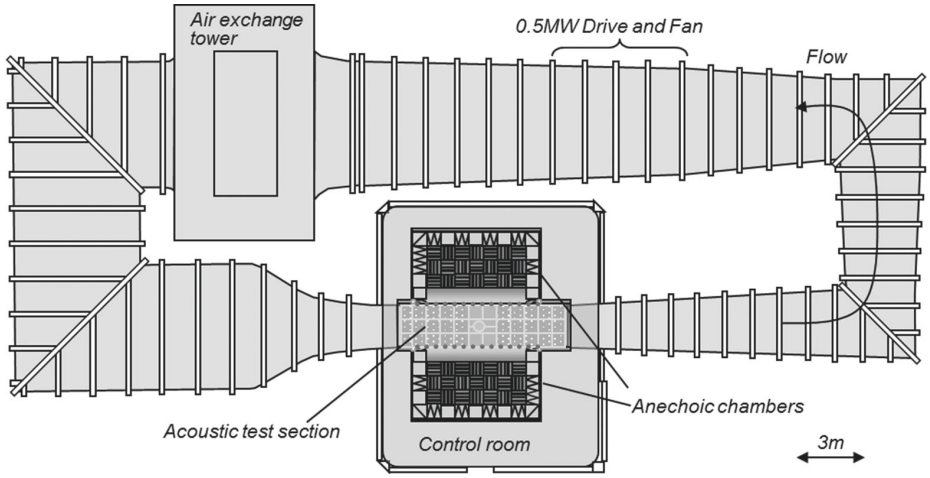

Fig. 3 Plan view schematic of the Virginia Tech Stability Wind Tunnel in anechoic configuration.

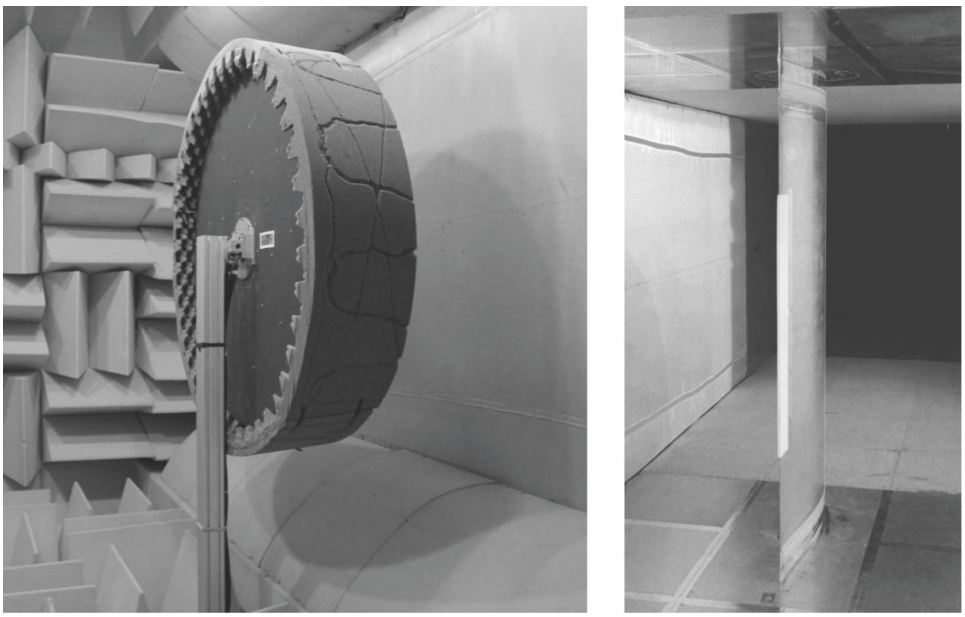

a) b)

Fig. 4 Illustrations of a) the 117 microphone phased-array system installed in the port-side anechoic chamber directed at the suction side of b) the 0.8 m chord DU96-W180 airfoil mounted in the anechoic test section.

placement of acoustic instrumentation. This unusual arrangement has a number of advantages over a conventional free-jet tunnel. It eliminates the need for a jet catcher, reduces aerodynamic interference corrections by about a factor of 4, allows for a long test section that provides a clear separation between model-generated sound and the parasitic noise of the facility, and permits acoustic instrumentation to be placed close to the model, yet out of the flow. Further details of the facility and its calibration are given in [10]. Acoustic and aerodynamic corrections applied to measurements made in this test section are also described in [10].

B. Airfoil Model, Boundary-Layer Tripping, and Lift Measurement

The 0.8 m chord airfoil model used for the experiments is illustrated in Fig. 4, as installed in the test section. The model has a DU96-W180 section (a standard wind turbine blade profile with a maximum thickness of 18% chord). The model was assembled from 50.8-mm-thick laminates, each cut with the airfoil profile. The laminate construction allows for easy installation of internal instrumentation, whereas careful alignment and accurate machining of the laminates ensures a smooth and continuous airfoil surface.

Serrated tape (Glasfaser-Flugzeug-Service, GmbH 3-D Turbulator Tape) of thickness 0.5 mm was used to trip the airfoil boundary layers. The tape was applied at the 5 and 10% chord locations of the suction and pressure sides of the airfoil, respectively.

Pressure distributions and lift on the model were measured using some 80 1 mm pressure taps distributed around the profile. Pressures were sensed using Esterline 9816/98RK pressure scanners with a range of ± 2.5 psi (rated accuracy of $\pm 0.05\%$ full scale) connected to the pressure taps through 1.6 mm Tygon tubing.

Table 1 Freestream turbulence levels

Freestream velocity, U_∞, m/s	Root mean square streamwise fluctuations, u'/U_∞
12	0.016%
21	0.021%
30	0.024%
48	0.029%
57	0.031%

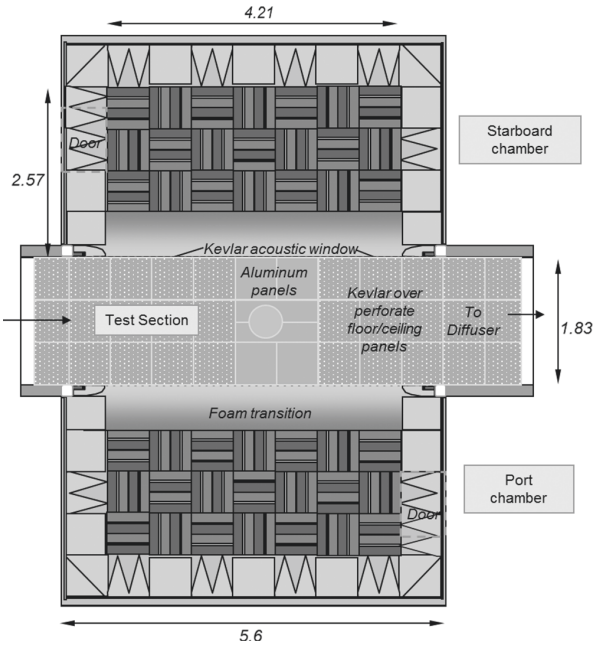

Fig. 5 Plan view cross section of the anechoic system as installed, showing the test section flanked by the two anechoic chambers. Dimensions in meters.

C. Measurement of Drag and Reference Conditions

Tunnel freestream velocity was monitored using the pressure difference between static taps located in the walls of the wind-tunnel settling chamber and contraction, sensed using the Esterline 9816/98RK pressure scanner system. Temperature in the test section was monitored using an Omega thermistor type 44004 (accuracy ± 0.2°C) and the ambient absolute pressure was determined using a Validyne DB-99 digital barometer (resolution 0.01 in. hg).

For some conditions, a rake of pitot and static probes was used to measure profiles through the airfoil wakes and infer the drag using a

momentum balance approach. The rake consists of 113 1.6-mm-diam pitot probes and 7 pitot-static probes distributed over a 1.8 m length. Mounted on the rake system are four DTC Initium ESP-32HD 32 channel pressure scanners with a range of ±2.5 psi and a rated accuracy of ±0.03% to which the tubes are connected. The rake is acoustically noisy and was therefore not used during sound measurements.

D. Sound Measurement

Airfoil trailing-edge noise was measured using a phased-array system located in the port-side anechoic chamber, facing the suction side of the airfoil (Fig. 4a). The array has 117 Panasonic electret microphones type WM-64PNT arranged in nine spiral arms, mounted on a solid 1.1-m-diam carbon-fiber disk. These microphones have a flat frequency response from 20 to 16,000 Hz. The array was calibrated to within ±5 deg phase and 0.4 dB amplitude from 500 to 16,000 Hz. The array was mounted in the port-side chamber, which was the suction side of the airfoil, slightly upstream of the quarter-chord position. Boundary-layer refraction effects, convective effects, pressure doubling due to the microphones being mounted on a solid surface, and attenuation through the Kevlar cloth have all been accounted for in postprocessing. Data were recorded simultaneously at 51,200 Hz for 32 s with two 64 channel peripheral component interconnect-based data acquisition cards. The signals were processed through an antialiasing filter with a cutoff frequency of 20 kHz. Spectral quantities were computed by averaging the Fourier transform of blocks of 8192 samples. The diagonal of the cross spectrum was removed to omit uncorrelated noise in the beamformed maps. Integrated spectra were computed by integrating the beamformed results over a selected region.

E. Trailing-Edge Noise Treatments

Two different treatment designs were developed with the goal of replicating the effects of a canopy on reducing surface pressure fluctuations, seen in the wall-jet tunnel measurements of Clark et al. [7], in a form suitable for application to an airfoil in external flow. The designs are illustrated in Fig. 6 and are referred to as finlet fences and finlet rails. A total of 20 variants on these designs were fabricated using rapid prototyping. All design variants involved either the rail or fence treatment, beginning 101.6 mm upstream of the trailing edge (87.3% chord), and in all cases, the treatment was supported on a thin sheet of material (the substrate) glued to the airfoil, with its leading edge placed 114.3 mm upstream of the airfoil trailing edge (85.7% chord). Only the middle half-span of the airfoil was treated (see Fig. 4b). The leading edge of the substrate was, in all cases, faired to the airfoil surface by covering it with 0.1-mm-thick metal tape.

The upper edges of finlet fences (Fig. 6a) are designed to present the same geometry to the airfoil boundary-layer flow as the unidirectional canopy of Fig. 2b. A total of 14 such fence configurations were tested, including variations in finlet spacing, height, thickness, extension past the trailing edge (TE), and substrate thickness. The rails (Fig. 6b) more explicitly replicate the fiber geometry of the canopy in Fig. 2b, with streamwise cylindrical elements mounted from the surface using periodic swept supports. A total of six such configurations were tested. Table 2 shows the full test matrix for both types of configurations. The table also includes the control cases, including the untreated tripped airfoil and two cases in which only substrate layers were applied to the airfoil surfaces.

As a final point, an important distinction should be emphasized here to differentiate the present treatment from "riblets," which have some shape similarities to finlets used for viscous drag reduction [11,12]. Riblets act on the very near wall boundary-layer structure and have a typical height and spacing of 10–15 wall units. Finlets are of a different scale altogether (10–100% of the boundary-layer thickness) and are designed to reduce noise by acting on the boundary-layer turbulence as a whole.

III. Results and Discussion

Measurements were made at flow speeds of 50 and 60 m/s, corresponding to chord Reynolds numbers of 2.5 and 3.0 million, respectively. We present here only results for Reynolds number 3.0 million, because those measured at 2.5 million are almost identical. For all cases, the airfoil boundary layers were fully turbulent, having been tripped as described in Sec. II.B. For all finlet fence and finlet rail configurations tested, far-field sound and mean surface pressure (and therefore lift) measurements were made with the airfoil pitched from −4 to 16 deg geometric angle of attack in approximately 2 deg increments. This range encompasses zero lift ($\alpha \approx -2.5$ deg) as well as stall ($\alpha \approx 11$ deg). Aerodynamic corrections [10] were used to calculate the effective angle of attack corresponding to each geometric angle of attack. All data will be presented in terms of these effective angles. In all cases, a measurement sequence with a treated condition was immediately followed or preceded by a measurement of the untreated condition to minimize the experimental uncertainty between the two and to establish (by comparing the many untreated-condition measurements) the repeatability of the results. Thus, the wind-tunnel entry included many repeat measurements of configuration C0, which will be referred to as the "clean condition." Configuration F8 was also repeated so that drag measurements could be made with the rake system without interference of the acoustic measurement. Because the majority of noise reduction was observed in the frequency range of 1500–5000 Hz, Table 3 shows overall levels in this frequency range for each configuration for which spectra are presented.

A. Noise Measurements Made with the Clean Airfoil

Figures 7 and 8 summarize the trailing-edge noise measurements made with the clean airfoil at $Re = 3$ million. Figure 7 shows sample beamform maps at 3 kHz. All acoustic source maps are shown in

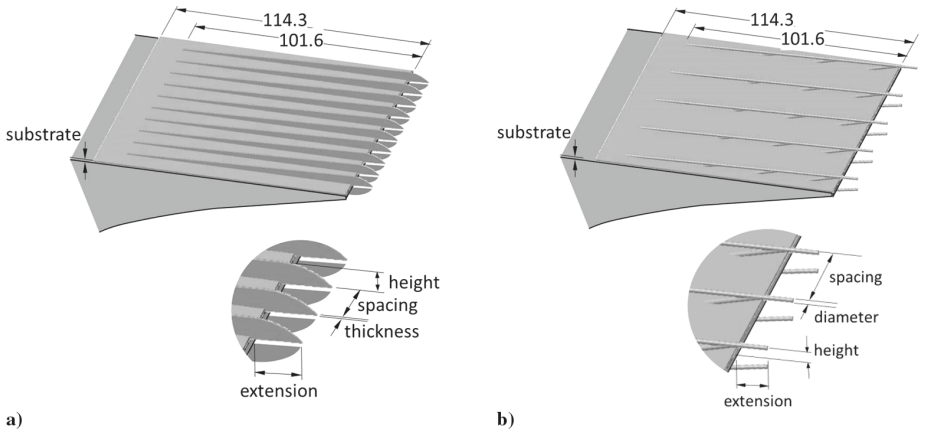

Fig. 6 Treatment designs tested on the DU96-W180: a) finlet fence; b) finlet rail. Diagrams show finlets attached to the trailing-edge portion of the airfoil. Dimensions in millimeters.

Table 2 List of finlet cases with dimensions in millimeters

Configuation no.	Height	Spacing[a]	Thickness/rail diameter	TE extension	Substrate	Suction only
			Control cases			
C0	— —	— —	— —	— —	— —	— —
C1	— —	— —	— —	— —	0.5	— —
C2	— —	— —	— —	— —	0.75	— —
			Fence cases			
F0	4	4	0.5	10	0.5	— —
F1	4	1	0.5	0	0.5	— —
F2	4	1	0.5	10	0.5	— —
F3	4	6	0.5	10	0.75	— —
F4	4	10	0.5	10	0.5	— —
F5	2	1	0.5	10	0.75	— —
F6[b]	4	1	0.5	10	0.5	— —
F7[c]	4	1	0.5	10	0.75	— —
F8	8	4	0.5	10	0.5	— —
F9	4	4	2	10	0.75	— —
F1S	4	1	0.5	0	0.5	Y
F2S	4	1	0.5	10	0.5	Y
F8S	8	4	0.5	10	0.5	Y
F10S	16	4	0.5	0	0.5	Y
			Rail cases			
R0	4	2.5	1.25	10	0.75	— —
R1	4	2.5	1.25	0	0.75	— —
R2	8	2.5	1.25	10	0.75	— —
R3	4	5	2.5	10	0.75	— —
R4	8	10	1.25	10	0.75	— —
R5[b]	4	2.5	1.25	10	0.75	— —

[a]Spacing was measured as the width of the open gaps between the finlets, not as the center-to-center spacing of the finlets. This preserves the spacing parameter when varying finlet thickness/diameter.
[b]Fence/rail length upstream of the trailing edge varied periodically in the spanwise direction with one period being the sequence 101.6, 12.7, 25.4, 12.7, 50.8, 12.7, 25.4, and 12.7 mm.
[c]Fence length upstream of the trailing edge varied periodically as in configuration 6, but with fence height scaled to 4, 2.5, 3, 2.5, 3.5, 2.5, 3, and 2.5 mm in the same periodic sequence, respectively.

Table 3 Overall sound levels in decibels, in the frequency range of 1500–5000 Hz

	Angle of attack			
Config no.	−2.5 deg	−0.5 deg	3.0 deg	6.9 deg
		Control cases		
C0	57.3	55.8	53.8	54.6
C1	58.2	56.5	54.0	54.5
C2	58.4	57.2	54.4	54.7
		Fence cases		
F0	53.3	53.0	52.2	54.1
F1	52.0	51.3	51.6	54.0
F2	50.3	50.4	51.0	54.0
F3	54.0	53.6	52.5	53.8
F4	54.7	54.2	53.2	54.6
F8	51.9	51.6	51.5	53.6
F9	52.8	52.4	52.0	53.7
F8s	54.7	53.3	51.7	53.3
		Rail cases		
R0	53.4	52.8	51.8	53.3
R1	53.3	52.6	52.2	53.8
R2	53.2	52.3	51.6	53.4
R3	53.4	53.1	52.6	54.5

terms of sound pressure level (SPL) on a decibel scale with a 10 dB range, using a reference pressure of 20 μPa. Figure 8 compares noise spectra integrated over the central 25% of the blade span, as indicated by the dashed box shown in Fig. 7a. Starting at the zero-lift angle of attack (Fig. 7a), the trailing-edge noise is clearly detectable at this frequency and is seen to form a clean uniform band along the trailing edge. At 3 kHz, as the angle of attack is increased, the trailing-edge noise actually decreases slowly (note the change in the absolute level of the color scales in Fig. 7) so that, once the quietest angle of attack of 3 deg is reached, the spurious lobes associated with the background noise levels generated by the facility appear more prominently. The trailing-edge noise is still easily distinguished, however, and remains so through 6.9 deg angle of attack until the airfoil stalls. At stall, airfoil-generated noise levels greatly increase (e.g., Fig. 7e) and a stall pattern with two spanwise cells is formed, clearly visible in the beamform map. Note that the weak source near the leading edge in Figs. 7c and 7d is believed to be background facility noise scattered from the leading edge.

One-twelfth octave band integrated spectral levels for angles of attack of −2.5, −0.5, 3.0, 6.9, and 14.8 deg are compared in Fig. 8. The area of integration for this and subsequent similar figures is shown by the black box drawn on Fig. 7a. Results are presented only up to 5 kHz because, above this frequency, background noise makes it difficult to distinguish trailing-edge noise. The difference in trailing-edge noise levels for varying angles of attack only becomes distinguishable above about 1500 Hz. This difference may be partly due to the beamwidth of the phased array, which becomes comparable to the integration area at this frequency, as discussed subsequently. Above 1500 Hz, the sound spectra are seen to be broadband in all cases. The sound level variations with angle of attack observed at 3 kHz in the beamform maps are seen to be representative of the whole frequency range, with spectral levels lowest at 3 deg angle of attack where they are up to 7 dB lower than those seen at zero lift.

B. Effects of the Baseline Fence Treatment

We examine first the effects of the baseline airfoil treatment, which we take as configuration F0. The treatment, shown in Fig. 9, consists of 0.5-mm-thick fences with a maximum height of 4 mm, spaced every 4 mm across the span. The fences extend by 10 mm past the trailing edge and are attached to the airfoil via a 0.5-mm-thick substrate. The treatment was placed on both sides of the airfoil and covered the center half-span of the model, so that direct comparisons could be drawn with the untreated regions at the ends of the airfoil. Figure 10 shows measurements of the lift on the airfoil as a function of angle of attack. There appear to be no detrimental effects of the treatment on the lift, and indeed, it appears that the lift is slightly

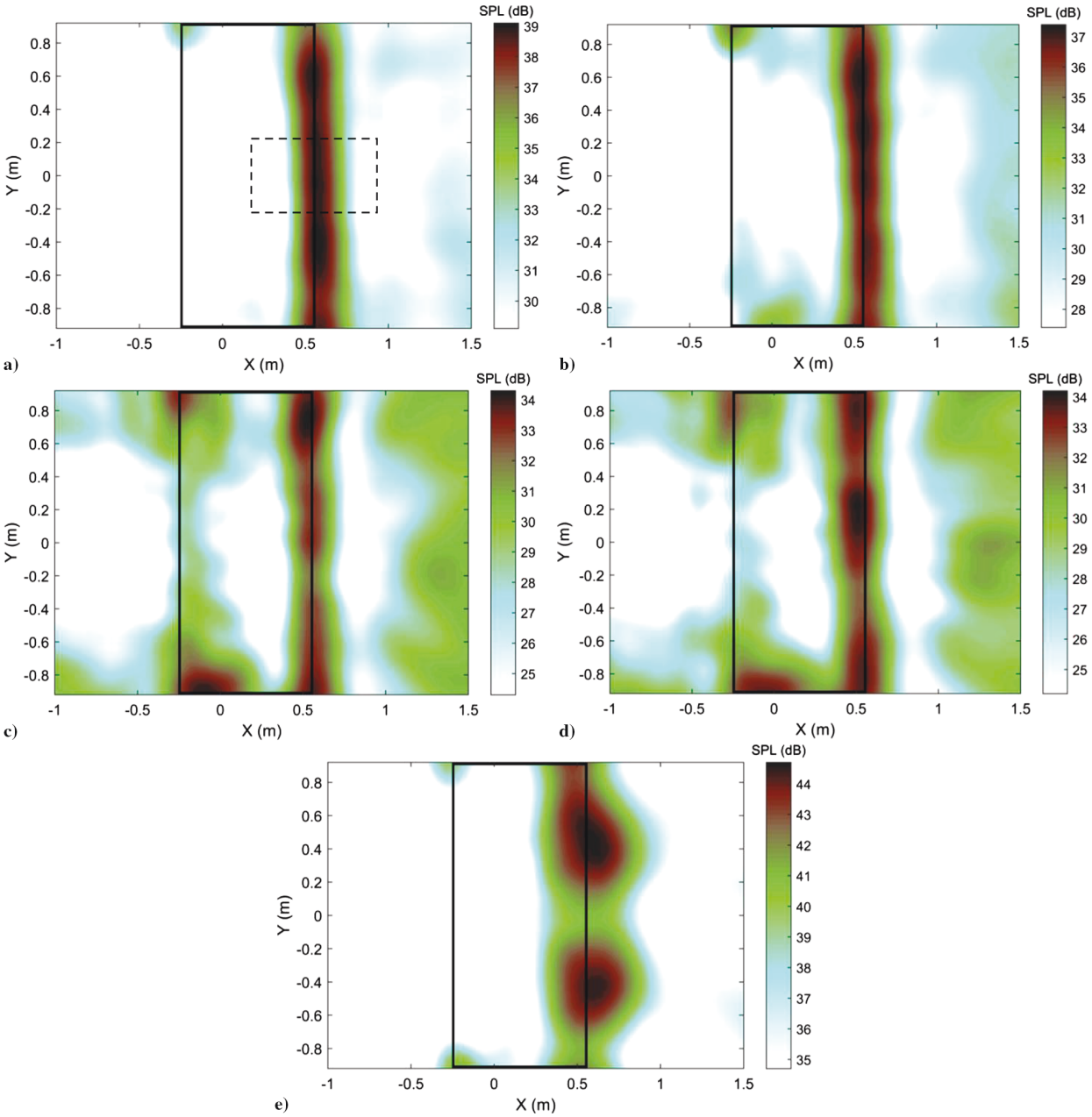

Fig. 7 Beamform maps showing the trailing-edge noise radiated by the untreated DU96-W180 airfoil at 3 kHz at angles of attack of a) −2.5, b) −0.5, c) 3.0, d) 6.9, and e) 14.8 deg; $Re = 3$ million.

enhanced poststall. Note that lift measurements were integrated using pressure distributions measured over the first 85% of the airfoil chord, extrapolated around the trailing edge using the Kutta condition requirement, because the last 15% of the chord was covered by the treatments when they were applied. This methodology was checked by comparing integrated lift results from the untreated airfoil using both the full set of pressure taps and the taps on the first 85% of chord (as if the airfoil were treated). No significant difference was found between the results obtained by using the two different sets of pressure taps.

Figure 11 shows beamform maps for the treated airfoil at $Re = 3$ million for the unstalled angles of attack (the treatment had no discernable influence on the airfoil sound, either positive or negative, poststall). Integrated spectra for the treated and untreated airfoil are compared for the zero-lift angle of attack in Fig. 12 and for other sample angles of attack in Fig. 13. At the zero-lift angle of attack (Fig. 11a), the beamform map shows no discernable trailing-edge noise coming from the treated portion of the airfoil, whereas the untreated portions appear almost unaltered from the results shown in Fig. 7a. This indicates about a 10 dB attenuation at 3 kHz for this condition. It should be noted here that, because of the significant attenuation of the noise in the trailing-edge region by the finlets, it is possible that some remaining noise in this region is actually due to side lobes of other nearby sources, such as the untreated portion of the airfoil, or to background noise from the facility. As such, the 10 dB attenuation seen here could be considered a conservative estimate. As the angle of attack increases (Figs. 11b–11d), the effectiveness of the treatment diminishes but is still substantial at −0.5 and 3 deg angle of attack and is certainly still detectable at 6.9 deg.

Figure 12 shows the effectiveness of the treatment over a broader range of frequencies at the zero-lift condition ($\alpha = -2.5$ deg). The attenuation achieved by the treatment is clearly broadband with

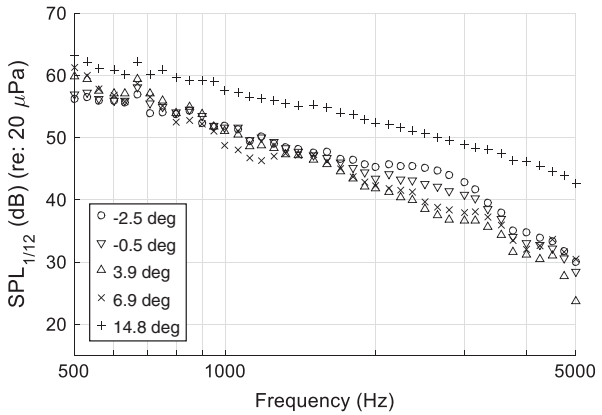

Fig. 8 Noise spectra for the untreated DU96-W180 at $Re = 3$ million, as a function of angle of attack obtained by integrating phased-array results over the central 25% of the airfoil span, as indicated by the dashed region in Fig. 7a.

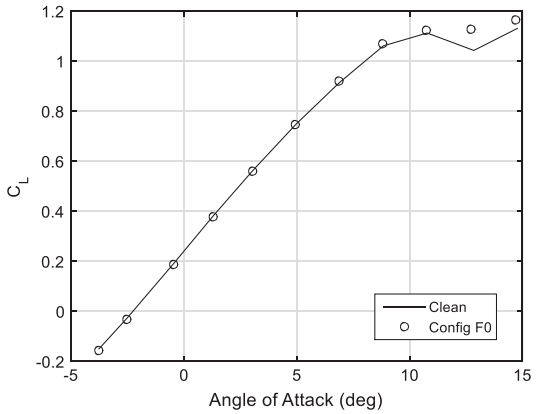

Fig. 10 Lift coefficient plotted against angle of attack for the untreated (clean) and baseline treated (Config F0) DU96-W180 at $Re = 3$ million.

reductions between 5 and 10 dB for frequencies between 2 and 5 kHz. For frequencies below 2 kHz, the effectiveness of the treatment appears to diminish, ultimately disappearing at about 1400 Hz. However, this is at least partly an artificial effect of the diminishing ability of the array to focus as the frequency is reduced. To illustrate this, Fig. 12 includes thumbnail images showing beamform maps of the treated airfoil sound field at different frequencies. Each thumbnail has been centered on the frequency to which it refers. At about 1500 Hz, the beamwidth of the array, defined as the width of the area 3 dB below the maximum of the main lobe of the point spread function, is approximately 0.5 m. This is comparable to the width of the treated portion of the airfoil span, and thus the lobes associated with the untreated portions at the two ends of the airfoil have begun to merge. There still appears to be some attenuation of the sound between the untreated regions, but this attenuation is largely obscured by blurring of the beamform map. As the frequency is reduced to 1 kHz, the ability of the array to distinguish features on the scale of the treated portion of the span has been completely lost. In an effort to reduce the ambiguity of low-frequency results due to the array characteristics, the CLEAN-SC deconvolution algorithm [13] was used in an attempt to extract information at low frequencies without success. CLEAN-SC works well for incoherent isolated sources, but performs poorly for a distributed line source like considered here, therefore, results were obscured by misplaced sources and facility noise.

The broadband effectiveness of the treatment is illustrated for a set of unstalled angles of attack in Fig. 13. At −0.5 deg angle of attack, the attenuation achieved with the treatment above 2 kHz is between about 3 and 7 dB. At 3 deg, the effectiveness of the treatment is somewhat diminished at frequencies below about 3.5 kHz, but is enhanced at higher frequencies, reaching about 12 dB near 4 kHz. At 6.9 deg angle of attack, the effectiveness of the treatment is noticeably reduced, but significant reductions in sound, of up to about 3 dB, are still visible at frequencies over 2.5 kHz. At no angle of attack is the treatment seen to have any detrimental effect on the radiated sound.

It is important to recognize that the substrate is not an inactive component of the treatment. Figure 14 shows the effect on integrated acoustic levels of adding only a 0.5- and a 0.75-mm-thick substrate to the airfoil, as compared with the clean case. (Note that configuration F0 is mounted on the thin 0.5 mm substrate.) At $\alpha = -2.5$ and -0.5 deg, the substrate adds to the trailing-edge noise at around 1500 and 1800 Hz for the 0.75 and 0.5 mm thicknesses, respectively, quite possibly because of vortex shedding enhanced because of the substrate adding to the trailing-edge thickness. At the same time, sound levels with the substrates are somewhat lower (by up to 5 dB for the 0.5 mm and 7 dB for the 0.75 mm) at higher frequencies. This could be because of a nonlinear redistribution of energy into the lower frequency vortex shedding motions. At $\alpha = 3$ and 6.9 deg, the increased levels ascribed to vortex shedding are smaller or absent. At the same time, the noise reductions are also smaller and do not appear until higher frequencies.

At the very least, the fences are clearly suppressing the detrimental effects of the substrate at low frequencies, while enhancing the noise reduction at high frequencies. One possible explanation is that the finlets suppress the surface pressure fluctuations at the airfoil trailing edge, and also coherent vortex shedding here, by breaking up the spanwise correlation length scale of the boundary layer. One can imagine the unidirectional canopy of [7] reducing wall pressure fluctuations by a similar mechanism.

C. Effects of the Fence Parameters

In this section, we examine the effects of varying the fence parameters. Note that all the treated cases produced lift characteristics that are almost identical to those of configuration F0 (i.e., the same as, or slightly better than, the untreated airfoil). Figure 15 shows the effects of changing the fence spacing by comparing integrated sound levels from configurations F2, F0, F3, and F4, representing spacings

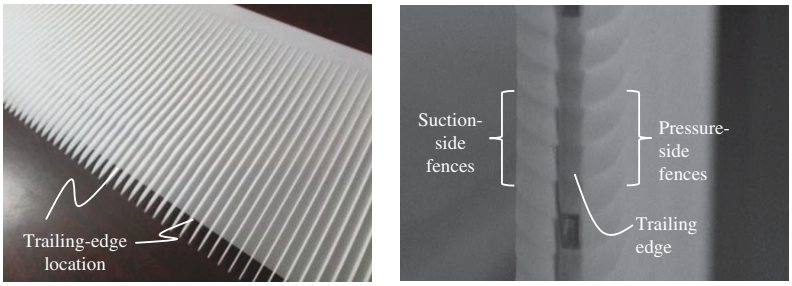

a) b)

Fig. 9 Finlet configuration F0: a) before attachment to the airfoil and b) after attachment to both sides of the airfoil (view seen looking upstream at the trailing edge). Note the gap between the fence extensions on either side of the trailing edge.

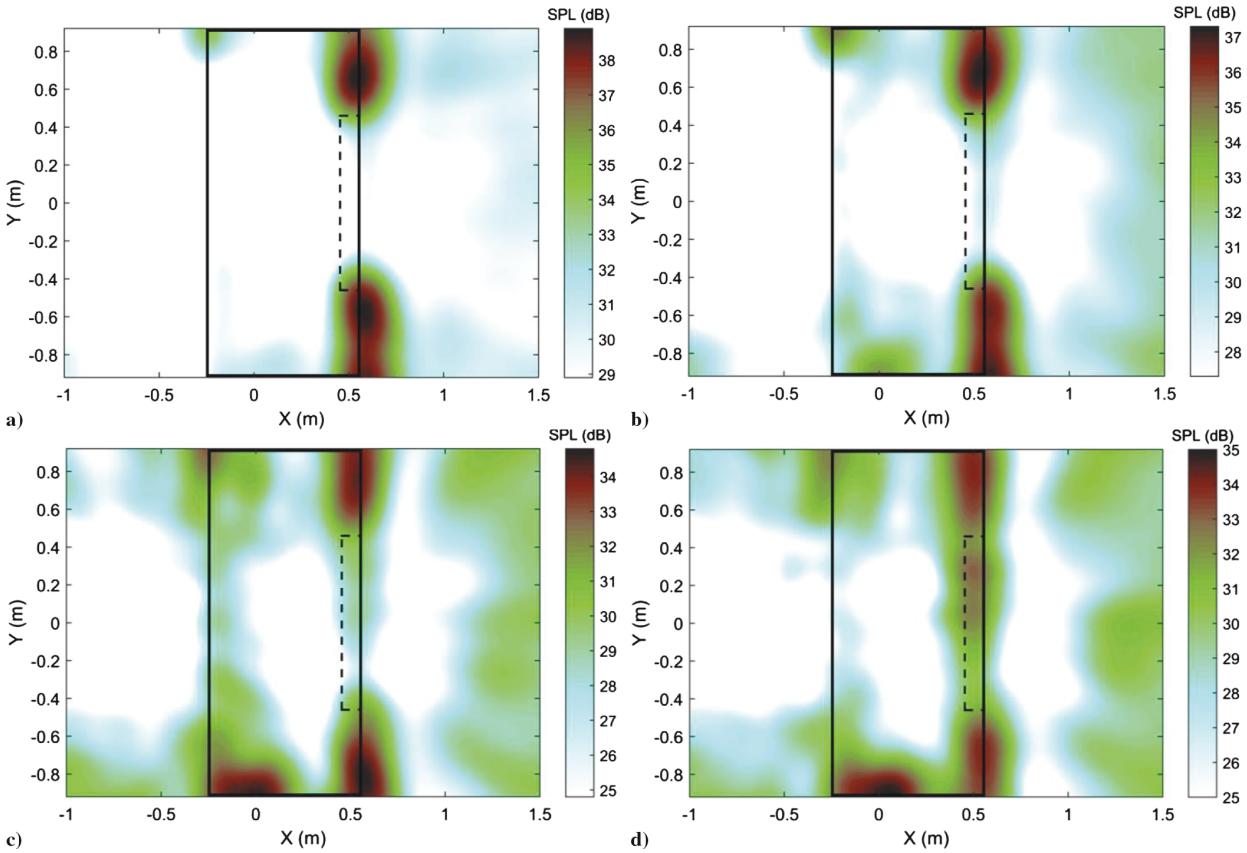

Fig. 11 Beamform maps showing the trailing-edge noise radiated by the DU96-W180 at 3 kHz at angles of attack of a) −2.5, b) −0.5, c) 3.0, and d) 6.9 deg with the baseline (configuration F0) treatment applied across the central half-span (as indicated by the dashed rectangle); $Re = 3$ million.

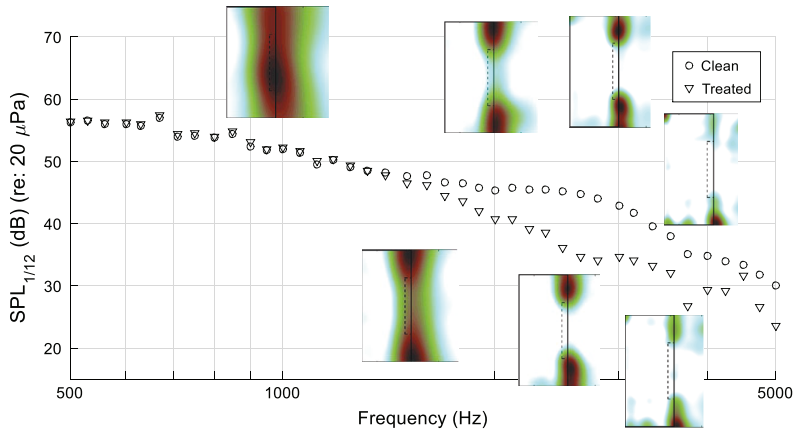

Fig. 12 Noise spectra for configuration F0 treatment compared with results for the clean case; $Re = 3$ million, −2.5 deg angle of attack. Inset images show beamform maps of the treated airfoil noise to illustrate the blurring effects of the large spot size at frequencies below about 2 kHz.

of 1, 4, 6, and 10 mm. Photographs showing three of these four treatments are shown in Fig. 16.

Overall, the noise spectra appear to show a clear progression with fence spacing for angles of attack $\alpha = -2.5, -0.5$, and 3 deg. At these conditions, the 6 mm spacing produces similar noise reductions to the 4 mm spacing described earlier. Reductions with the 10 mm spacing are less, particularly at frequencies over 3.5 kHz. Reductions with the 1 mm spacing are greater, by 1–4 dB over almost all the frequency range. This dependence appears consistent with the fences limiting the spanwise correlation length scale: The smaller the spacing, the smaller the maximum correlation scale that can survive to the trailing edge. There is clearly a limit to the beneficial effect though, in the form of the intense spike that appears in the spectra for the 1 mm spaced fence at around 650 Hz. At 60 m/s, this frequency corresponds to a distance scale of about 18 mm (at a Strouhal number of 0.2), which is of the same order as the sum of the trailing-edge thickness (2.5 mm), both substrate layers (1 mm), and two fence heights (8 mm). The implication is that, below a certain minimum spacing, somewhere between 1 and 4 mm in this case, the fences start to behave like a solid, much thicker, blunt trailing edge. At $\alpha = 6.9$ deg, the noise reductions are smaller in all cases and the dependence on fence spacing less apparent. Acoustic levels at this angle of attack are slightly lower at high frequencies with the 6 mm spaced fence (configuration F3), perhaps because the substrate used

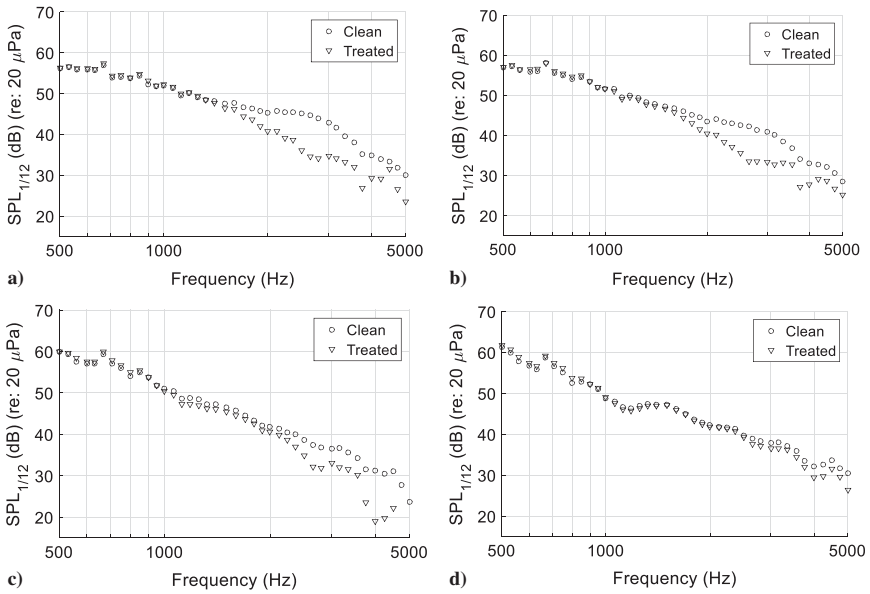

Fig. 13 Noise spectra for configuration F0 treatment compared with results for the clean case at angles of attack of a) −2.5, b) −0.5, c) 3.0, and d) 6.9 deg; $Re = 3$ million.

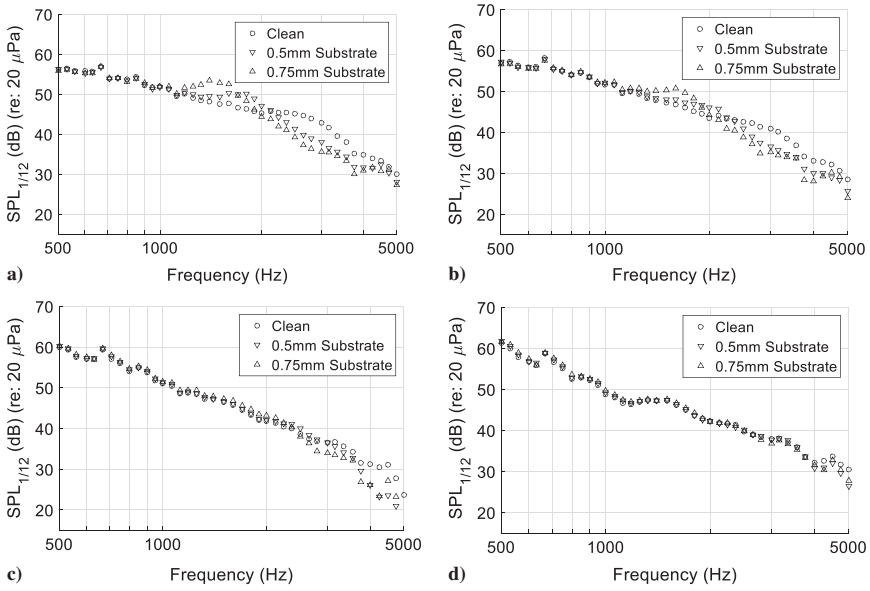

Fig. 14 Noise spectra for configurations C1 and C2 showing substrate-alone effects at angles of attack of a) −2.5, b) −0.5, c) 3.0, and d) 6.9 deg compared with the clean case; $Re = 3$ million.

with this configuration was slightly thicker than for the other cases in this comparison (0.75 versus 0.5 mm).

The effects of extending the treatment past the trailing edge are examined in Fig. 17. This compares integrated noise spectra for case F2 (1 mm spaced, 4-mm-high fences extending 10 mm past the trailing edge) to case F1 (identical geometry, but shortened so that the fences end at the trailing edge). At lower angles of attack, $\alpha = -2.5$ and -0.5 deg both configurations produce almost identical acoustic results, including the intense vortex shedding peak associated with the 1 mm spacing. The results are also quite similar at 3 and 6.9 deg angles of attack, except that high-frequency noise levels (>3 kHz) are noticeably lower without the extension. It appears, therefore, that the extension offers little if any benefit and, indeed, comes at a price at higher angles of attack. This implies that the fence "finlets" are, as hypothesized, manipulating the boundary-layer structure as it reaches the trailing edge, rather than altering the scattering efficiency by reshaping the trailing edge, as is accomplished by a trailing-edge serration or comb. This suggests it may be possible to maximize noise attenuation by combining both control strategies.

Figure 18 examines the effect of fence height on the acoustic signature of the airfoil. Here results for configuration F0 (4-mm-high, 4 mm spaced fences) are compared with those of configuration F8 (8-mm-high, 4 mm spaced fences) and the clean airfoil. At all angles of attack and at almost all frequencies, noise levels are reduced by 1 to 2 dB by a doubling of the fence height. This effect can be understood in the context of the boundary-layer thickness at the trailing edge. XFOIL [14] calculations suggest displacement thicknesses, for the tripped DU96 at $Re = 3$ million, of 0.9, 1.2, 1.8, and 3.1 mm for the suction side and 0.7, 0.5, 0.3, and 0.2 mm for the pressure side at $\alpha = -2.5$, -0.5, 3, and 6.9 deg, respectively.

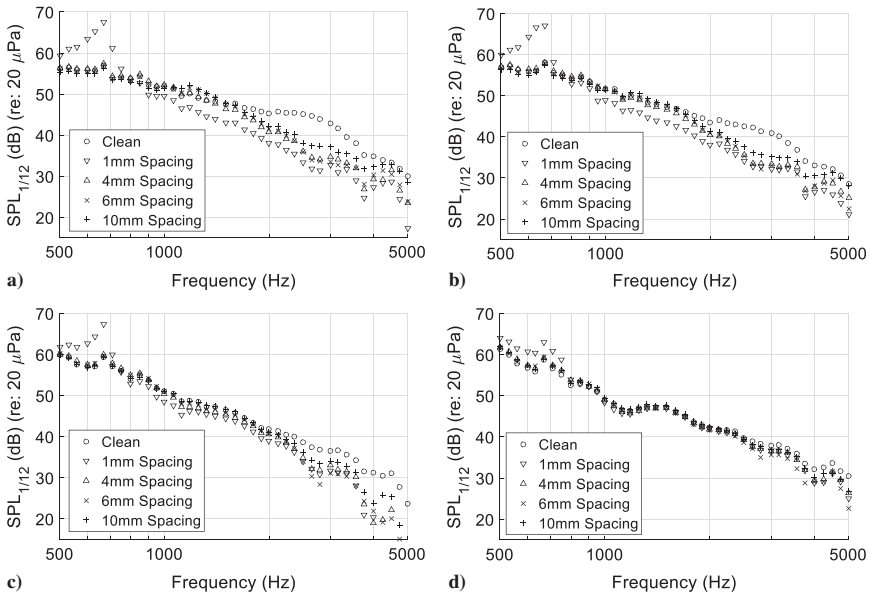

Fig. 15 Noise spectra for configurations F2, F0, F3, and F4 showing the effects of fence spacing on noise radiation at angles of attack of a) −2.5, b) −0.5, c) 3.0, and d) 6.9 deg compared with the clean case; $Re = 3$ million.

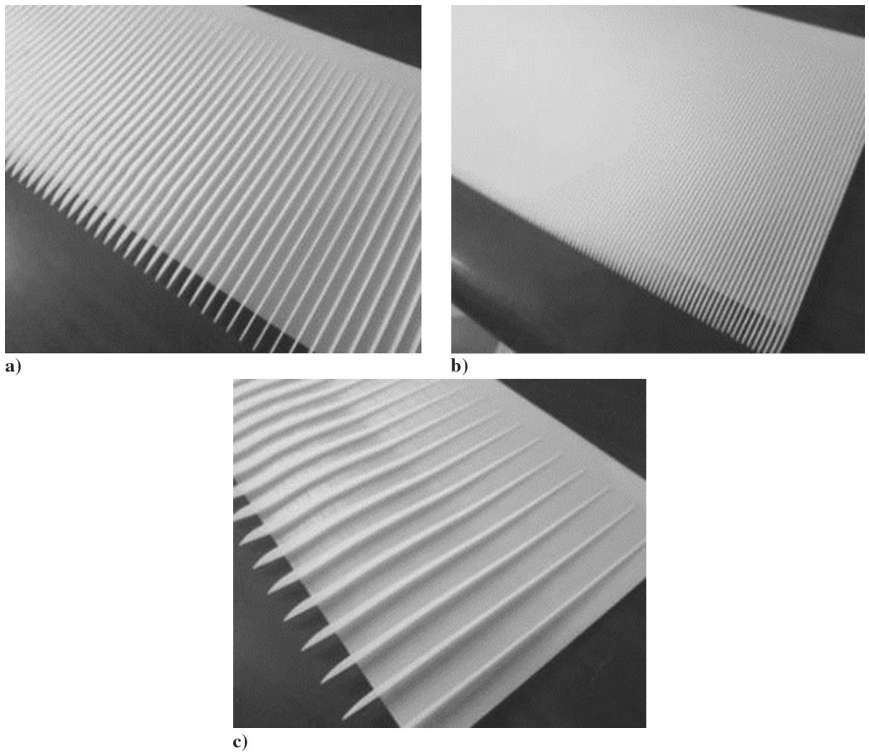

Fig. 16 Photographs of treatments F2, F0, and F4, fence treatments with a) 1, b) 4, and c) 10 mm spacing, respectively, before application to the airfoil.

Assuming overall boundary-layer thicknesses 3–5 times these values, it is clear that increasing the fence height from 4 to 8 mm would cause the fences to cut substantially more of the boundary layer, particularly on the suction side, and thus have a greater impact on the spanwise correlation length scale and thus the radiated noise. This conceptual model implies that further noise reductions at high angle of attack could be achieved by increasing the height of the suction-side fences, in accordance with the increase in boundary-layer thickness.

Unlike other configurations, the 8-mm-high fence treatment of configuration F8 was tested twice, the second time with the drag rake system in place. Figure 19 compares the drag on the airfoil with this treatment with that of the clean case (configuration C0) and of the corresponding substrate alone case (configuration C1). The clean airfoil exhibits a drag bucket with a minimum C_d of about 0.008 near the zero-lift angle of attack of −2.5 deg. The drag then rises gradually with angle of attack through an angle of attack of 8 deg, after which the airfoil stalls, resulting in erratic fluctuations in the

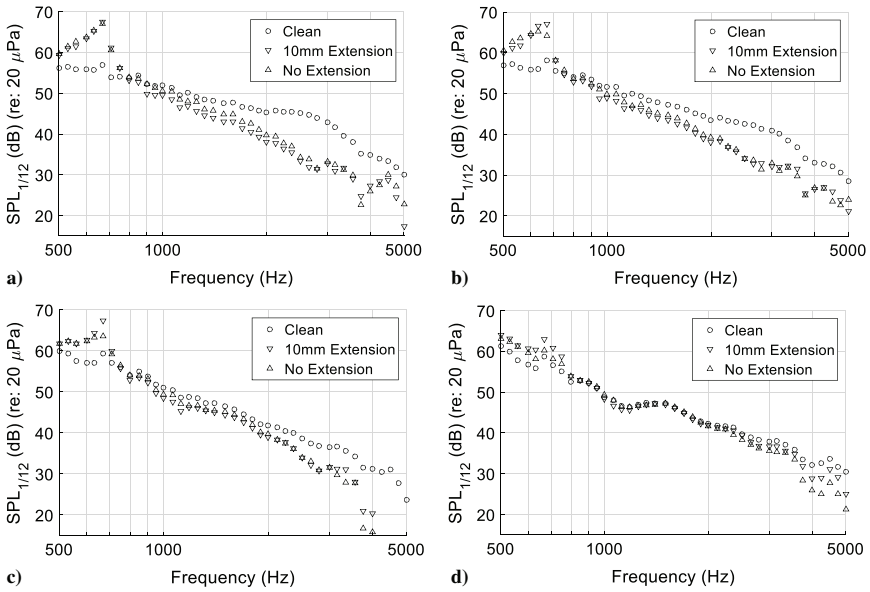

Fig. 17 Noise spectra for configurations F2 and F1 showing the effects of fence extensions over the trailing edge on noise radiation at angles of attack of a) −2.5, b) −0.5, c) 3.0, and d) 6.9 deg compared with the clean case; $Re = 3$ million.

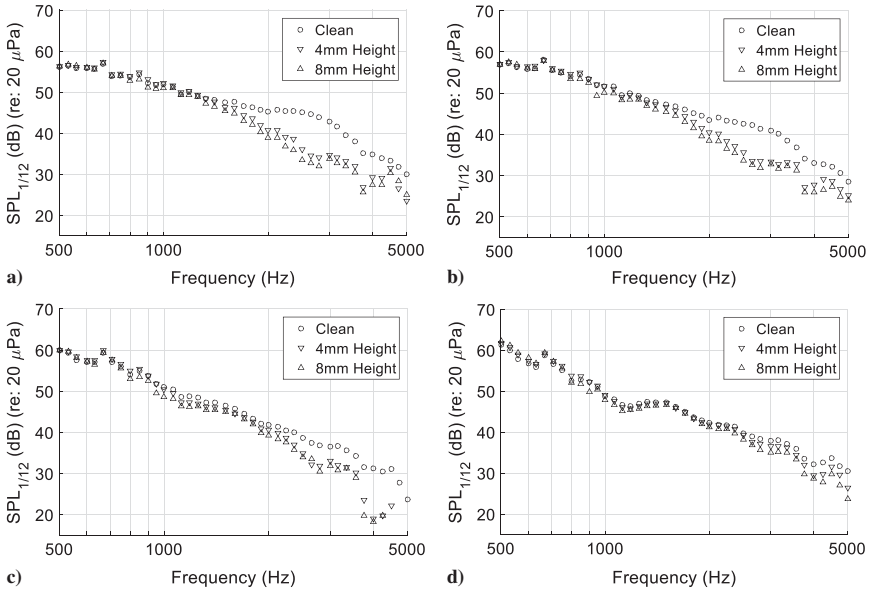

Fig. 18 Noise spectra for configurations F0 and F8 showing the effects of fence height on noise radiation at angles of attack of a) −2.5, b) −0.5, c) 3.0, and d) 6.9 deg compared with the clean case; $Re = 3$ million.

drag curve and overall a sudden rise. (Note that the slight reduction in C_d between 8 and 11 deg is a consequence of basing the drag on a wake measurement at a single spanwise station; three-dimensional flow at the initiation of stall can result in a local thinning of the wake, despite its overall dramatic growth.) Adding the substrate to the airfoil (configuration C1) has no significant impact on the unstalled drag. Adding the 8-mm-high fences of configuration F8 increases the drag by about 10%. The airfoil has a surface area of some 6400 mm^2 for every 4 mm of span. The fences add about 500 mm^2 to this total, or about 8%, indicating that, to the accuracy of its measurement, the increase in wetted surface area associated with the fences accounts for the drag increase.

Configuration F9 replicates the fence geometry of configuration F0, but with 2-mm-thick fences in place of 0.5-mm-thick fences and with a 0.75-mm-thick substrate in place of a 0.5 mm thickness, as shown in Fig. 20. The effects of these changes on the sound measured above the suction side of the airfoil are shown in Fig. 21. Above 1.5 kHz, the effects of these geometry changes is a slight reduction (up to about 3 dB) of acoustic levels. Some fraction of these could, perhaps, be ascribed to the substrate effect (Fig. 14), but at the very least, we see that the thicker fences are not detrimental to the acoustic performance of the treatment. The results below 1.5 kHz are less clear. At the lower angles of attack, acoustic levels appear suppressed by the thicker treatment around 1100 Hz, but these levels are increased by the treatment at around 700 Hz, perhaps indicating that the fences initiate some organized turbulent motion at these low frequencies.

Figure 22 shows the effects of only using the configuration F8 treatment on the suction side of the airfoil (configuration F8S) versus the treatment on both sides (configuration F8). In both cases, the

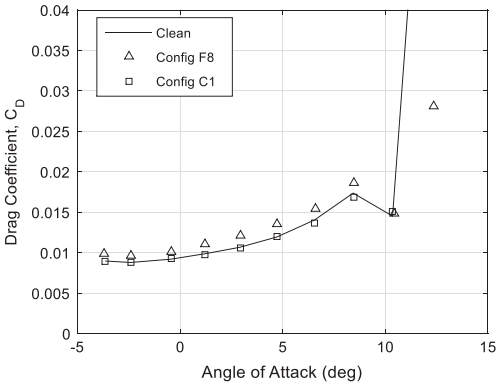

Fig. 19 Drag coefficient as a function of angle of attack measured for the clean airfoil, with configuration F8, and with the substrate alone (configuration C1); $Re = 3$ million.

treatment is 8-mm-high fences with a spacing of 8 mm. At angles of attack of −2.5, −0.5, and 3 deg, the effect of removing the pressure-side treatment is, to a good approximation, to halve the decibel attenuation produced by the treatment. It is difficult to draw a solid quantitative inference from this result, because it is unclear how much of the sound is generated by the suction- and pressure-side boundary layers and by the interaction between them. However, if we assume equal contributions from both boundary layers and no interaction effect, then a complete elimination of the sound from the suction-side boundary layer would be observed as a broadband 3 dB reduction relative to the clean airfoil. At 6.9 deg angle of attack, the removal of the pressure-side treatment has no effect on the sound radiated from the foil. This suggests that, either the pressure-side treatment is ineffective at large angles of attack or, as seems more probable, the suction-side boundary layer is the dominant contributor to the far-field sound at such conditions.

D. Effects of the Rail Treatments

In addition to the finlet designs discussed earlier, a series of tests were carried out on rails that extend from the surface, as shown in Fig. 6. These shapes are more like the hairs on the owl wing discussed in Sec. I. Figure 23 shows the first rail case, configuration R0, installed on the trailing-edge portion of the airfoil trailing-edge region. This configuration uses 1.25-mm-diam rails rising to 4 mm above the airfoil surface and spaced at 2.5 mm intervals across its span. The rails extend 10 mm downstream of the trailing edge. In terms of aerodynamic performance, all the rail cases produced lift curves almost indistinguishable from those of configuration F0, shown in Fig. 10. Drag measurements were not made with the rail cases.

The geometric parameters of configuration R0 do not exactly match any of the fence cases but fall somewhere between configuration F2 (4-mm-high fences with 1 mm spacing) and configuration F0 (4-mm-high fences with 4 mm spacing). Noise measurements made with configurations R0, F2, and F0 are compared with those for the clean airfoil in Fig. 24. At angles of attack of −2.5, −0.5, and 3 deg, the rail treatment produces almost identical noise attenuation to the 4 mm spaced fences, and unlike the 1 mm spaced fences, there is no evidence of low-frequency vortex

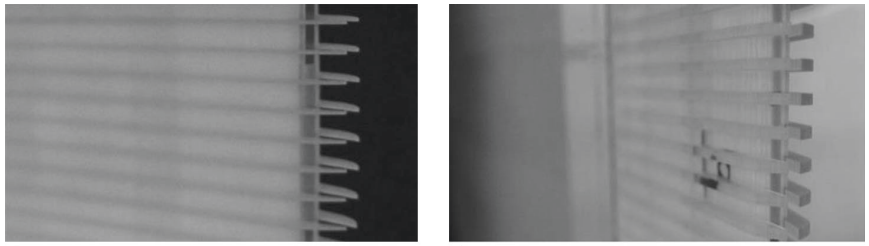

Fig. 20 Comparison of configurations a) F0 and b) F9 illustrating the difference in fence thickness. Pictures are looking upstream from the trailing edge.

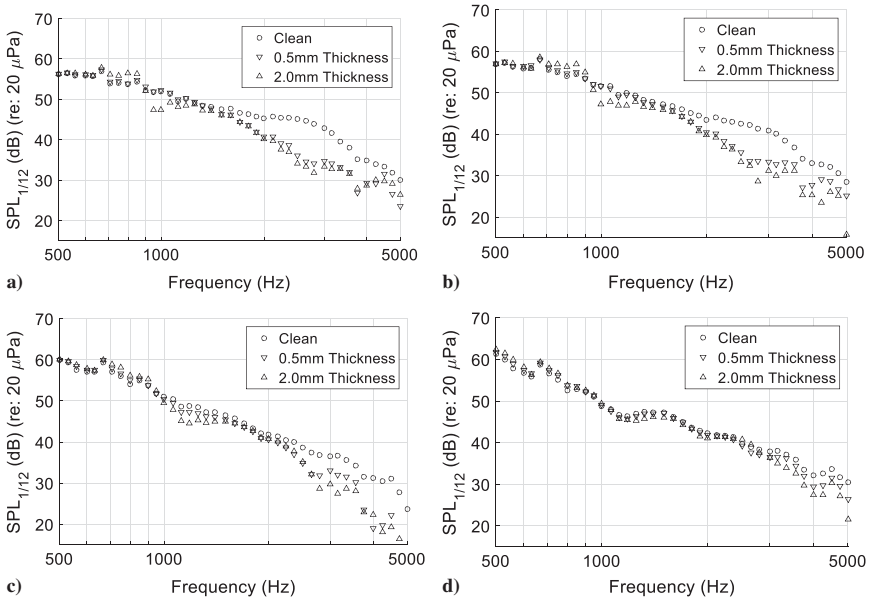

Fig. 21 Noise spectra for configurations F0 and F9 contrasting the effects of fence thickness at angles of attack of a) −2.5, b) −0.5, c) 3.0, and d) 6.9 deg compared with the clean case; $Re = 3$ million. Note that configurations F0 and F9 have different substrate thicknesses of 0.5 and 0.75 mm, respectively.

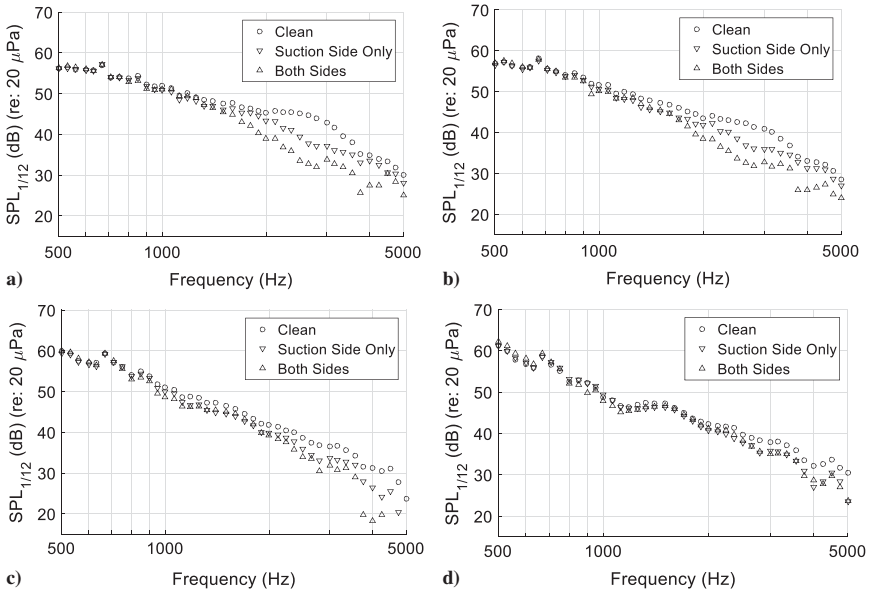

Fig. 22 Noise spectra for configurations F8 and F8S contrasting the effects of applying the treatment to both sides of the airfoil (F8) and just the suction side (F8S), at angles of attack of a) −2.5, b) −0.5, c) 3.0, and d) 6.9 deg compared with the clean case; $Re = 3$ million.

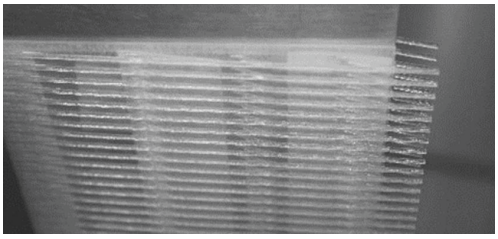

Fig. 23 Side view of configuration R0 applied to both sides of the airfoil, showing the rail geometry.

shedding associated with an effective increased trailing-edge thickness. Close to stall, however, at an angle of attack of 6.9 deg, the rails perform significantly better than the fences, producing detectable attenuation at frequencies down to 2 kHz and doubling the decibel attenuation at higher frequencies.

The acoustic performance of a selection of the other rail cases is plotted in Fig. 25. This includes elimination of the trailing-edge extension (configuration R1), doubling of the maximum rail height to 8 mm (configuration R2), and doubling of the diameter and spacing to 2.5 and 8 mm, respectively (configuration R3). The change that has the least effect appears to be the elimination of the trailing-edge extension, which has no impact on the sound attenuation compared with configuration R0, other than perhaps a slight reduction in attenuation at the very highest frequencies. As with the fence configurations, increasing the spacing (configuration R3) reduces the attenuation achieved by the treatment by a few decibels above about 2500 Hz. Contrary to what was seen with the fences, doubling the maximum height of the rails to 8 mm (compare configurations R0 and R3) is actually counterproductive, particularly at the highest angle of

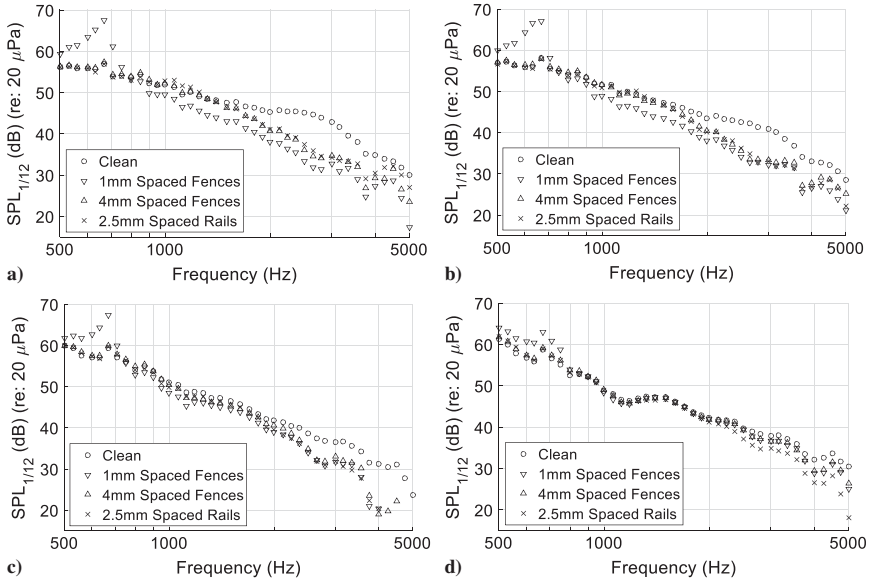

Fig. 24 Noise spectra for configurations F2, F0, and R0 contrasting the effects of fence and rail treatments of similar scale, at angles of attack of a) −2.5, b) −0.5, c) 3.0, and d) 6.9 deg, compared with the clean case; $Re = 3$ million.

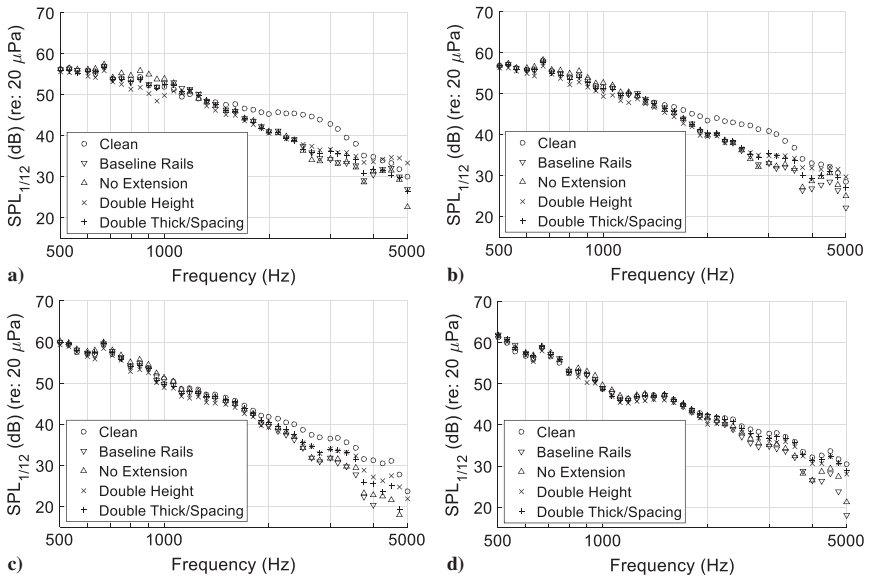

Fig. 25 Noise spectra for configurations R0, R1, R2, and R3 contrasting the effects of different rail treatments, at angles of attack of a) −2.5, b) −0.5, c) 3.0, and d) 6.9 deg compared with the clean case; $Re = 3$ million.

attack (6.9 deg) where the additional height might expect to be beneficial in penetrating the thicker suction-side boundary layer. It may be that, if made too large, the space under the rails may permit reconnection of spanwise coherent structures and thus limit the reduction in spanwise correlation length scale that can be achieved.

IV. Conclusions

Airfoil treatments to reduce trailing-edge noise, inspired by the downy canopy found to coat the flight feathers of some owls, have been developed. These treatments were designed to replicate the surface-pressure-attenuating effects of the canopy in a form suitable for application to an airfoil.

Over 20 variants of these designs have been tested by performing aeroacoustic wind-tunnel measurements on a tripped DU96-W180 airfoil at chord Reynolds numbers up to 3 million. Variations include treatment thickness, density, length, position relative to the trailing edge, and the effectiveness of treating only one side of the trailing edge. Compared with the untreated airfoil, the treatments were found to be effective at providing broadband attenuation of trailing-edge noise of up to 10 dB. Treatments were found to be effective over an angle-of-attack range that extends to over 9 deg from the zero-lift condition. Airfoil treatments were observed to have no detrimental effect on the lift performance of the airfoil. Drag is slightly increased but only by an amount commensurate with the increase in wetted surface area associated with the treatment.

The acoustic level attenuation is found to be robust to changes in nondimensional flow parameters, and there appears to be good potential for tailoring the treatment to suit engineering system design requirements. The changes in noise attenuation in response to changes in geometric parameters of the finlet fence treatment provide the best clues about how this could be accomplished. From decreased performance with increased finlet spacing, along with increased performance with increased finlet height, it is reasonable to conclude that the extent to which the finlets can cut, deform, or otherwise decorrelate the turbulent structures in the boundary layer is the primary driver in the noise attenuation mechanism. However, it is important to limit the effect of the treatment on the mean flow, as demonstrated by the increased low-frequency noise produced by the 1 mm spaced finlets attributed to vortex shedding. The assertion that the finlets are acting to modify the scattering edge in a manner similar to serrations or combs is refuted by the observation of improved performance when the finlets do not extend past the trailing edge. This observation suggests some possibilities for improved performance. One option is to shift the finlets upstream of the trailing edge, in which case finlets of a given size will encompass a higher portion of the boundary layer and therefore have a greater effect on the turbulence there. Alternatively, the use of smaller finlets upstream could lead to decreased drag compared with the use of larger finlets near the trailing edge due to the decreased additional wetted area. It should be noted here that this option assumes the decorrelation of spanwise turbulent structures by the finlets persists over a significant portion of the chord of the airfoil downstream of the finlets, and that this length is more than that between the end of the finlet and the trailing edge. The second possibility is to combine the finlet treatment with modifications to the trailing-edge geometry, such as the aforementioned serrations or combs, with the intent of combining both boundary-layer pretreatment and decreased efficiency of the scattering edge.

The finlet rail performance trends offer additional clues about the relevant flow physics around the treatments. Doubling the height of the rails appeared to decrease performance, particularly at higher frequencies where the sound is produced by smaller turbulent eddies in the boundary layer. This trend may suggest that the increased open area beneath the rails prevents the smaller scale turbulent fluctuations from being decorrelated (one could imagine the open space allowing pressure and velocity fluctuations to be communicated or propagated beneath the rails). The additional high-frequency noise above that of the untreated case may be caused by increased turbulence levels generated by the flow past the rails (which have a cylindrical cross section).

In contrast to the information provided by changing geometric parameters of the treatment, the acoustic effects of adding the substrate only serve to complicate and obscure the effects of the treatment itself. However, it can be reasonably concluded that, although the substrate has a significant influence on the acoustics when placed on its own, the effect of the finlets dominates over this influence when the full treatment is applied. The additional noise (compared with the untreated airfoil) observed at some frequencies due to the substrate is completely eliminated by the finlets. At frequencies where the substrate showed a noise reduction compared with the untreated airfoil, the finlets improved and increased this noise reduction even further. The only remaining concern is whether or not the finlets might be somehow dependent on the substrate for most of the noise reduction. One could imagine the upstream step of the substrate exerting an influence on the boundary layer such that a certain flow pattern was set up, perhaps featuring an additional bias toward larger, more spanwise-oriented turbulent eddies. The finlets

might then have a greater influence on this new flow than, say, the unmodified boundary layer over the clean airfoil. This seems unlikely, however, considering the difference in scales between the substrate thickness (0.5 mm), finlet height (4 or 8 mm), and the boundary-layer thickness (on the order of 10–20 mm on the airfoil's suction side).

Acknowledgments

The authors would like to thank the Office of Naval Research, in particular, Ki-Han Kim and Woei-Min Lin, for their support under grants N00014-13-1-0244, N00014-14-1-0242, and N62909-12-1-7116 (Naval International Cooperative Opportunities in Science and Technology Program). The assistance of Aurelien Borgoltz and Tim Meyers over the course of the wind-tunnel testing, and the support of the College of Engineering at Virginia Polytechnic Institute and State University in performing that testing, are gratefully acknowledged. Thanks also go to Daniel Grohol, for his assistance in performing computer aided design of the trailing-edge treatments, and Scott Patrick, for his help with their manufacture. The support of AVEC, Inc. in providing the phased-array system and related assistance is gratefully acknowledged. The authors would like to sincerely acknowledge the late Geoffrey Lilley, whose long-standing interest in and insight into the aeroacoustics of the owl has been a source of great inspiration.

References

[1] Graham, R. R., "The Silent Flight of Owls," *Journal of the Royal Aeronautical Society*, Vol. 38, No. 286, 1934, pp. 837–843. doi:10.1017/S0368393100109915

[2] Kroeger, R. A., Gruschka, H. D., and Helvey, T. C., "Low Speed Aerodynamics for Ultra-Quiet Flight," U.S. Air Force Flight Dynamics Lab. Technical Rept. AFFDL-TR-71-75, Wright–Patterson AFB, OH, 1972.

[3] Sarradj, E., Fritzsche, C., and Geyer, T., "Silent Owl Flight: Bird Flyover Noise Measurements," *AIAA Journal*, Vol. 49, No. 4, 2011, pp. 769–779. doi:10.2514/1.J050703

[4] Geyer, T., Sarradj, E., and Fritzsche, C., "Measurement of the Noise Generation at the Trailing Edge of Porous Airfoils," *Experiments in Fluids*, Vol. 48, No. 2, 2010, pp. 291–308. doi:10.1007/s00348-009-0739-x

[5] Jaworski, J. W., and Peake, N., "Aerodynamic Noise from a Poroelastic Edge with Implications for the Silent Flight of Owls," *Journal of Fluid Mechanics*, Vol. 723, May 2013, pp. 456–479. doi:10.1017/jfm.2013.139

[6] Jaworski, J. W., and Peake, N., "Parametric Guidance for Turbulent Noise Reduction from Poroelastic Trailing Edges and Owls," *Proceedings of the 19th AIAA/CEAS Aeroacoustics Conference*, AIAA Paper 2013-2007, May 2013.

[7] Clark, I. A., Devenport, W. J., Jaworski, J. W., Daly, C., Peake, N., and Glegg, S., "The Noise Generating and Suppressing Characteristics of Bio-Inspired Rough Surfaces," *Proceedings of the AIAA/CEAS 20th Aeroacoustics Conference*, AIAA Paper 2014-2911, June 2014.

[8] Glegg, S., and Devenport, W., "The Far-Field Sound from Rough-Wall Boundary Layers," *Proceedings of the Royal Society of London, Series A: Mathematical, Physical and Engineering Sciences*, Vol. 465, No. 2106, 2009, pp. 1717–1734. doi:10.1098/rspa.2008.0318

[9] Choi, K., and Simpson, R. L., "Some Mean Velocity, Turbulence and Unsteadiness Characteristics of the VPI & SU Stability Wind Tunnel," Department of Aerospace and Ocean Engineering, Virginia Polytechnic Institute and State Univ. Rept. VPI-Aero-161, Blacksburg, VA, 1987.

[10] Devenport, W. J., Burdisso, R. A., Borgoltz, A., Ravetta, P. A., Barone, M. F., Brown, K. A., and Morton, M. A., "The Kevlar-Walled Anechoic Wind Tunnel," *Journal of Sound and Vibration*, Vol. 332, No. 17, 2013, pp. 3971–3991. doi:10.1016/j.jsv.2013.02.043

[11] Walsh, M. J., "Riblets as a Viscous Drag Reduction Technique," *AIAA Journal*, Vol. 21, No. 4, 1983, pp. 485–486. doi:10.2514/3.60126

[12] Choi, H., Moin, P., and Kim, J., "Direct Numerical Simulation of Turbulent Flow over Riblets," *Journal of Fluid Mechanics*, Vol. 255, Oct. 1993, pp. 503–539. doi:10.1017/S0022112093002575

[13] Sijtsma, P., "CLEAN Based on Spatial Source Coherence," *Aeroacoustics*, Vol. 6, No. 4, 2007, pp. 357–374. doi:10.1260/147547207783359459

[14] Drela, M., "XFOIL: An Analysis and Design System for Low Reynolds Number Airfoils," *Low Reynolds Number Aerodynamics*, Vol. 54, Lecture Notes in Engineering, Springer–Verlag, Berlin, 1989, pp. 1–12. doi:10.1007/978-3-642-84010-4_1

L. Ukeiley
Associate Editor

Chapter 5

Understanding Trailing Edge Noise Control Using Finlets

This chapter is comprised of the draft manuscript to be submitted to AIAA Journal which describes detailed computations and experiments performed to improve scientific understanding of the fluid mechanics of finlets. The present author is named as first author of this manuscript, while Dr. William Devenport and Dr. W. Nathan Alexander are named as co-authors.

5.1 Abstract

Recent work has developed a novel technique for trailing edge noise control through the manipulation of boundary layer turbulence upstream of the trailing edge by finlets. Although the finlets have been proven to reduce trailing edge noise over a wide frequency range, previous studies have not explained the flow phenomena responsible for this noise reduction. The present work takes a two-part approach to developing this explanation through a Reynolds-Averaged Navier-Stokes flow simulation and a near-full-scale experiment in the Virginia Tech Stability Wind Tunnel. Simulation results were used to analyze the effect of finlets on the flow near the trailing edge, while unsteady surface pressure and trailing edge noise results characterized the influence of finlets on turbulence near the trailing edge. The results suggest that the suction side finlets attenuate noise by suppressing the magnitude of surface pressure fluctuations responsible for trailing edge noise through retardation of the flow between the finlets. In contrast, the pressure side finlets attenuate noise by decorrelating spanwise-organized turbulent structures through the formation of boundary layers on the finlets themselves. A theoretical analysis of the unsteady surface pressure as it relates to trailing edge noise concludes the study.

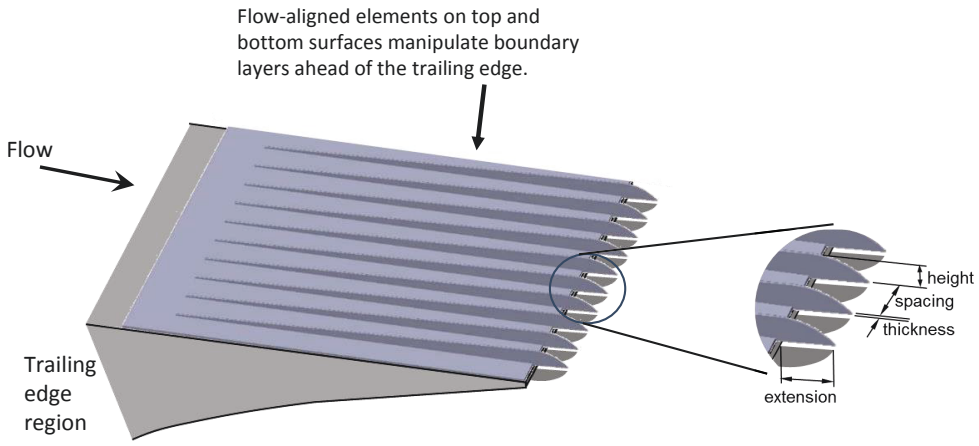

Figure 5.1: Finlet concept of Clark *et al.* [19].

5.2 Introduction

The aerodynamic noise generated by wind turbines is a source of annoyance for those living near wind farms [1, 2]. Noise regulations in some areas force wind turbines to run more slowly (and therefore more quietly) than would be possible without such regulations, leading directly to decreased power output and increased energy costs. A dominant source of noise from wind turbines is the trailing edge of the blade [3]. Trailing edge noise is investigated in many experimental and theoretical works [4, 5, 6, 7, 8, 9] and is understood to be caused by the scattering of unsteady pressure in the turbulent boundary layer by the trailing edge. Numerous methods have been investigated to control and reduce this noise, primarily through airfoil design or by modifying the geometry of the trailing edge of an existing airfoil using serrations [10, 11] or trailing edge brushes [12]. However, novel solutions to the trailing edge noise problem may be inspired by the anatomy of silently-flying [13] owls, which have three unique feather characteristics as identified by Graham [14]: a comb of evenly-spaced bristles along the wing leading edge, investigated by Kroeger *et al.* [15], a porous and elastic trailing edge fringe, investigated by Jaworski and Peake [16], and fine downy hairs that coat the exposed surfaces of the flight feathers, investigated by Clark *et al.* [17]. Although it has been thought that the leading and trailing edge traits of the owls' feathers are responsible for most of the flow noise attenuation, the work of Lilley [18] posited by process of elimination that the downy hairs are likely responsible for a significant fraction of the total noise attenuation by modifying the boundary layer turbulence before it is scattered by the trailing edge. This work in particular suggests that new methods of trailing edge noise control may be possible through manipulation of the boundary layer flow, as opposed to previous methods which focused on the trailing edge geometry.

The work described in this paper follows on from the study of Clark *et al.* [19], in which the authors developed this new type of trailing edge treatment after Clark *et al.* [17] showed

that a sparse layer of fibers suspended above a surface (and which therefore resembled the downy coating of the owls' feathers) could reduce pressure fluctuations on that surface by up to three orders of magnitude. The new trailing edge technology consisted of long, thin streamwise elements, termed "finlets," spaced evenly on both sides of the airfoil near the trailing edge (Fig. 5.1). Acoustic wind tunnel experiments of this trailing edge treatment applied to a DU96-W180 airfoil at a Reynolds number of 3 million showed that trailing edge noise was reduced over a wide frequency range, with attenuation levels of up to 10 dB. It was shown that results were improved when the finlets did not extend downstream of the trailing edge, which supported the theory that they were modifying the turbulence in the boundary layer in a manner similar to that described by Lilley [18] in reference to owls' feathers. A number of other geometric parameters were investigated, including finlet height, spacing, and thickness. However, the experiment was limited to far-field acoustics and mean surface pressure data over the untreated portion of the airfoil, and the conclusions regarding the finlet effects on lift and drag were therefore limited by the data available.

As a result of the limited data from that study, the work of Clark *et al.* [19] could best be described as a "proof of concept" study in which the main result was the demonstration of noise reduction by the finlets. However, little discussion was devoted to an explanation of the fluid mechanics behind the noise reduction. Afshari *et al.* [20] performed flow and surface pressure measurements around finlets. They found that the finlets reduced the magnitude of pressure fluctuations and spanwise correlation lengthscale near the trailing edge. Millican *et al.* [21] measured velocity and turbulence intensity profiles between finlets in a wall-jet wind tunnel and found that a significant velocity deficit occurred in the channel between the finlets. They hypothesized that the noise reduction was due to a mechanism known as shear sheltering, which prevents large turbulent eddies from scattering off of the trailing edge as noise. This is consistent with the noise reduction model of Clark *et al.* [17]. While these studies yield some insight into the flow near finlets, their test environments were limited to finlets on flat plates at modest Reynolds numbers.

To fill the need for more insight into the flow and the function of finlets on a high Reynolds number airfoil, the present work takes a two-part approach to further investigation. The first part of this study comprised a Reynolds-Averaged Navier Stokes (RANS) flow simulation of a DU96-W180 airfoil with and without finlets in flow conditions similar to those in the Virginia Tech Stability Wind Tunnel. Due to the difficulties in producing a mesh for the "finlet rails" of Clark *et al.* [19], the present work focuses only on the "finlet fences." The data obtained from this simulation showed the influence of the finlets on the flow near the trailing edge. For the second part of the investigation, the experiment of Clark *et al.* [19] was redesigned to include more instrumentation which would yield a more varied data set for use in analysis. In particular, surface pressure microphones were installed near the trailing edge of the airfoil to examine the relationship between surface pressure fluctuations and far-field noise in the presence of the finlets. Improved mean surface pressure instrumentation was also included to obtain data in the treated portion of the airfoil, addressing one of the shortfalls of the study of Clark *et al.* [19]. This two-part approach allowed for the buildup of a more

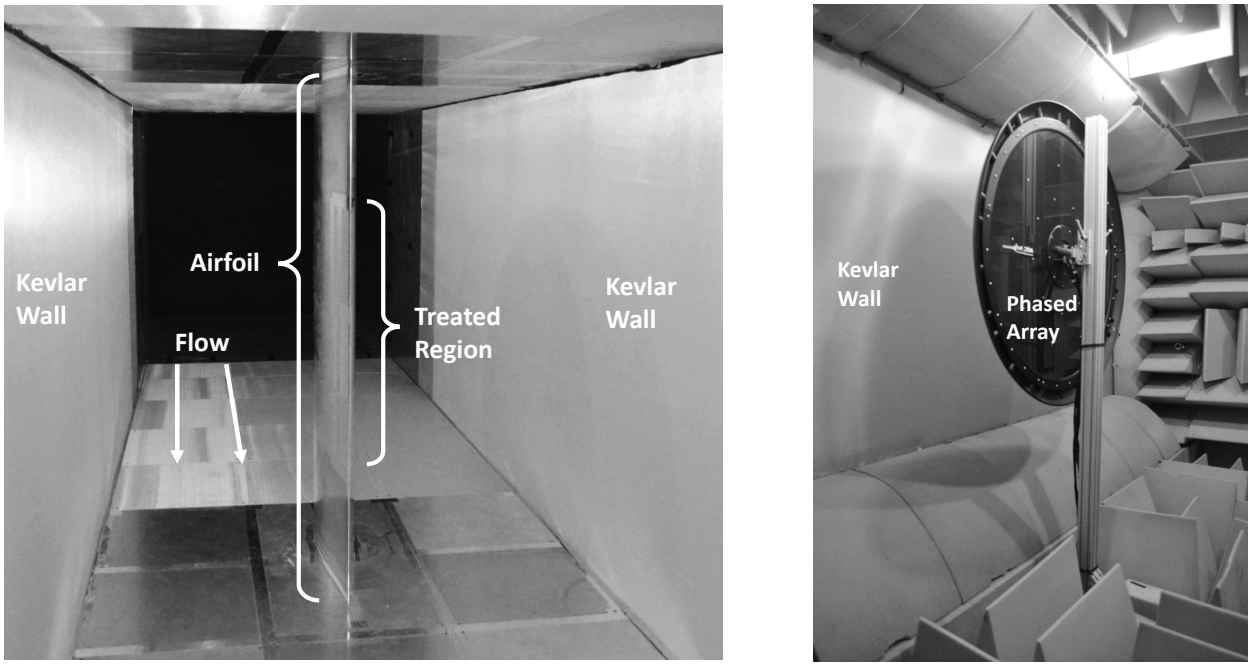

(a) (b)

Figure 5.2: Views of a) the 0.8-m chord DU96-W180 airfoil mounted in the anechoic test section and of b) the 117-microphone phased array system installed in the starboard side anechoic chamber directed at the suction side of the airfoil.

complete picture of the fluid mechanics of finlets, from flow velocity and turbulence levels to fluctuating surface pressure to trailing edge noise, while considering the influence of the finlets on lift and drag.

5.3 Experimental and Computational Methods

5.3.1 Wind Tunnel, Airfoil Model, Tripping, and Lift Measurement

The Stability Wind Tunnel at Virginia Tech was used for the experimental portion of the investigation. This facility features a test section specifically designed for aeroacoustic measurements shown in Fig. 5.2. Aerodynamic and acoustic corrections used for this facility are based on those in Devenport *et al.* [22], with updated parameters specific to the particular Kevlar used for this experiment. The aerodynamic corrections include those for blockage by the airfoil model, deflection of the Kevlar walls, and flow transpiration through the Kevlar, among other effects. For more detail on the flow facility and associated corrections, see

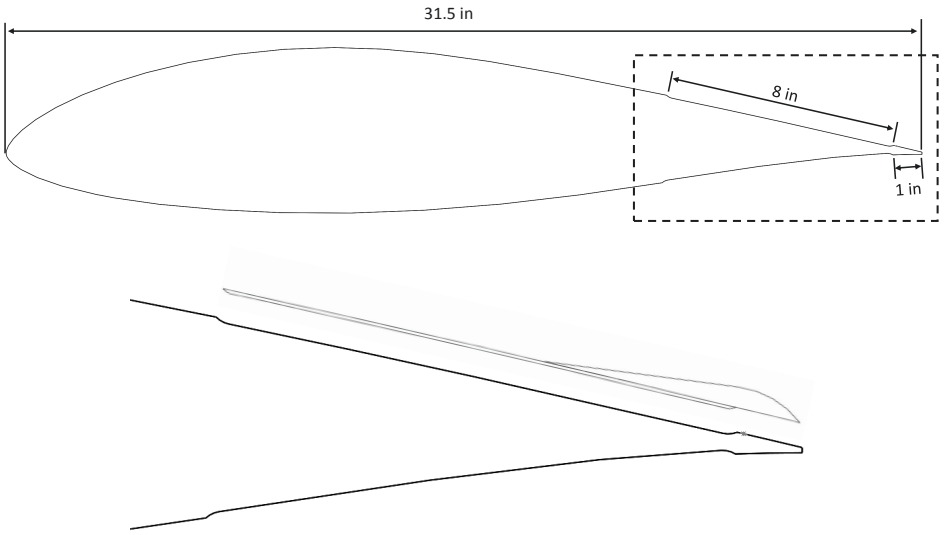

Figure 5.3: Schematic views of entire DU96 airfoil and detailed view of dashed region with "pocket" for treatment.

references [19, 22].

A 0.8-m chord DU96-W180 airfoil was used for this experiment. The airfoil model extended the full height of the test section and was manufactured by cutting 50.8-mm thick laminates with the airfoil profile and joining them together using pins inserted into precisely drilled holes of adjacent laminates. The use of this method allows for easy integration of instrumentation into the center of the airfoil model, and precise machining and careful alignment of each laminate preserves a smooth and hermetically sealed surface.

To prevent any of the trailing edge treatment substrate from protruding above the model surface, a shallow pocket with a depth of 1.6 mm was cut into the suction and pressure side surfaces of the laminates near the trailing edge in which the treatment substrate fit flush, preserving a smooth surface. The pockets extended 203 mm in the streamwise direction along the surface of the airfoil and were placed such that the downstream edge of the pocket was 25.4 mm upstream of the trailing edge. The airfoil and pockets are shown in Fig. 5.3. A narrow "ridge" which preserved the original DU96 geometry was incorporated into one airfoil laminate, and so as to allow placement of mean surface pressure taps in the treated region (Fig. 5.4). To obtain control measurements of flow parameters and noise levels without finlets, "blank" substrate panels were placed in the pockets to restore the smooth, unmodified airfoil shape.

Pressure distributions and lift on the model were sensed by 81 1-mm pressure taps distributed around the airfoil model as shown in Fig. 5.5. Pressures were measured using Esterline 9816/98RK pressure scanners with a range of $\pm$ 2.5 psi (rated accuracy of $\pm$ 0.05% full scale) connected to the pressure taps through 1.6 mm Tygon tubing.

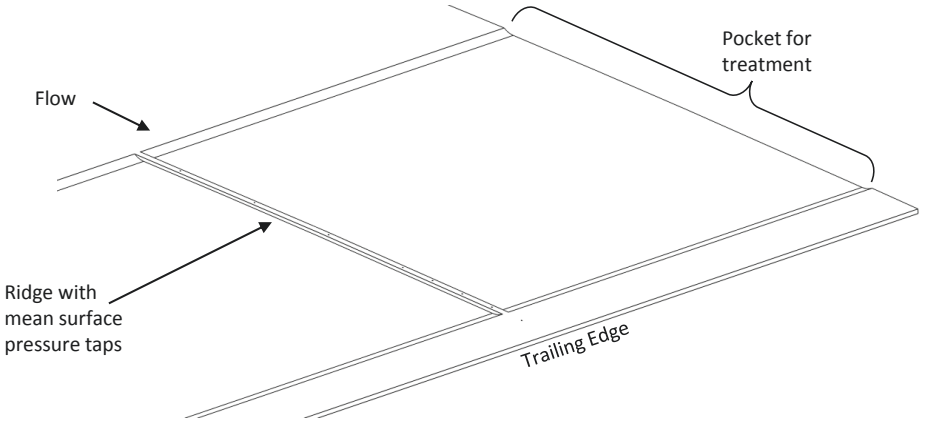

Figure 5.4: Schematic view of pocket with "ridge" of unmodified DU96 surface geometry featuring mean surface pressure taps.

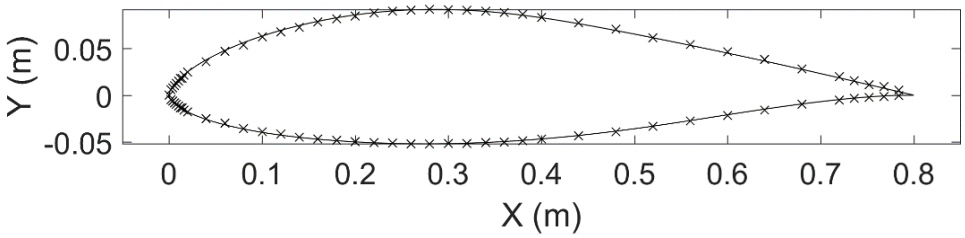

Figure 5.5: Schematic of mean pressure tap locations around airfoil.

The airfoil boundary layer was tripped in some cases using 0.5-mm high serrated tape (Glasfaser-Flugzeug-Service GmbH 3D Turbulator Tape). The tape was applied at the 5% and 10% chord locations of the suction and pressure sides of the airfoil, respectively.

5.3.2 Measurement of Drag and Reference Conditions

To measure the free-stream conditions in the test section, a series of static pressure taps are located in the walls of the tunnel settling chamber and contraction. The pressures were sensed by the same Esterline pressure scanners used for the airfoil model. The temperature in the test section was measured by an Omega Thermistor type 44004 with an accuracy of $\pm 0.2^{\circ}$ C. Finally, the ambient absolute pressure was measured by a Validyne DB-99 digital barometer with a resolution of 0.01" Hg.

Drag measurements were accomplished using a momentum balance approach with data from a rake of 113 1.6-mm diameter Pitot probes and seven Pitot-static probes distributed over a

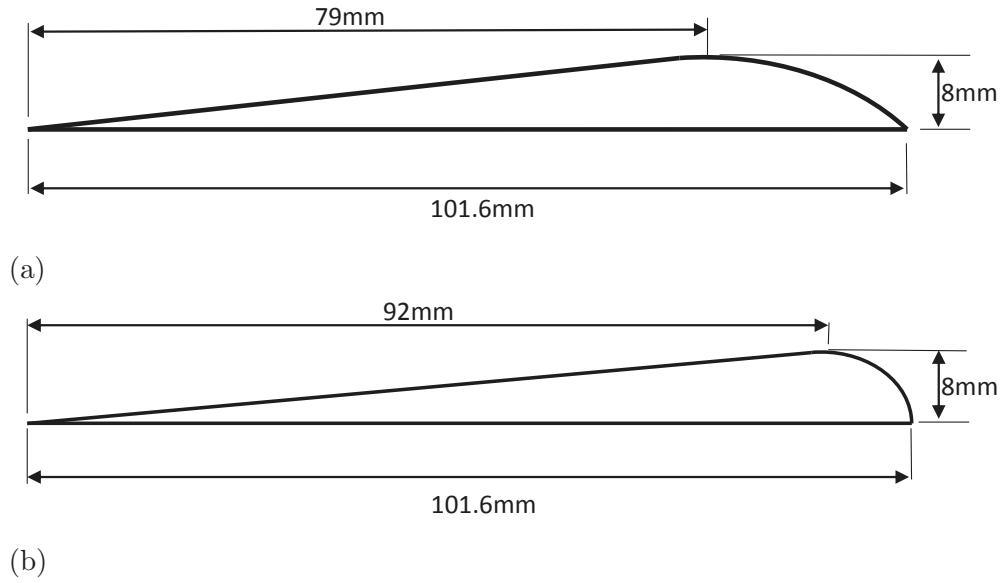

Figure 5.6: Schematic side-views of a) experimental and b) simulation finlets.

1.8-m span (encompassing almost the entire width of the test section). The rake was located downstream of the model to measure the wake of the airfoil. Four DTC Initium ESP-32HD 32-channel pressure scanners were mounted directly on the rake. These have a range of ± 2.5 psi and a rated accuracy of $\pm 0.03\%$. Uncertainty in drag coefficient measurements was estimated during prior experiments by comparing repeated measurements on different days at nominally identical conditions, and was found to be approximately 5% of the measured value. Parasitic noise from this rake will easily overwhelm any sound generated by an airfoil model, so acoustic measurements were only performed once the rake was removed.

5.3.3 Trailing Edge Treatment

The finlets used for this study were similar in shape to the "finlet fences" of Clark *et al.* [19], with some modifications to the geometry. Figure 5.6 shows a side view profile of the finlets used in the computational and experimental studies. The finlets featured a leading edge consisting of a simple straight line, followed by a circular arc which was tangent to the leading edge line and which curved back to the surface of the airfoil at the trailing edge. The simulation finlets, which more closely matched an equivalent configuration from the previous study [19], featured a circular arc with a vertical constraint at the trailing edge. This constraint was relaxed for the experimental configuration in order to place the location of maximum finlet height above microphones embedded in the surface (described in Section 5.3.5), as the location of the microphones was constrained by the thickness of the trailing edge region.

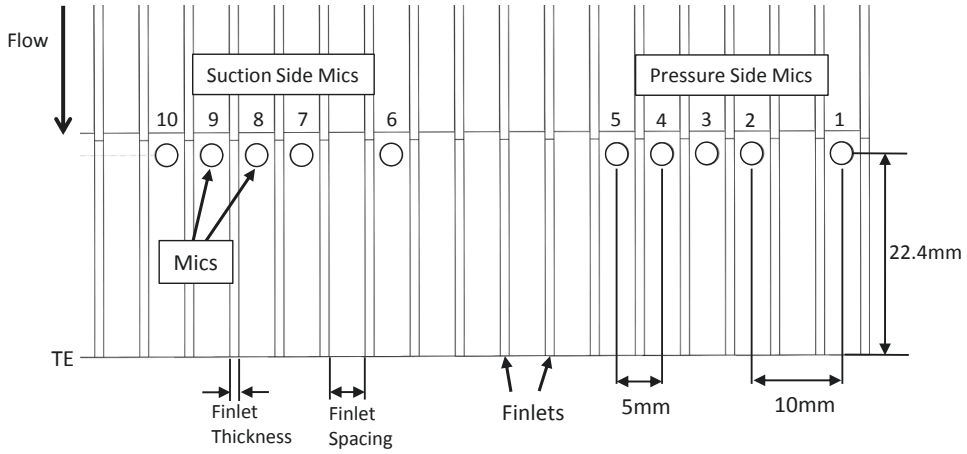

Figure 5.7: Schematic top/bottom view of finlets on airfoil with surface pressure microphone locations.

Figure 5.7 shows a schematic of the finlets applied to the airfoil and defines the geometric parameters which describe the finlet design. Both the simulation and experimental finlets featured an effective thickness of 1 mm, a maximum height of 8 mm, and a spacing of 4 mm. The thickness was chosen for structural reasons, as the last 25 mm of the finlets would not be supported by substrate material (this was necessary to allow for surface pressure fluctuation measurements). The height and spacing dimensions were chosen after the previous results [19] showed that 8 mm high finlets with 4 mm spacing yielded the best noise reduction. The Reynolds number of the finlets themselves, based on the free-stream velocity and chordwise extent of the finlets, was approximately 3×10^5, but transition was expected to occur early on the finlets due to the high turbulence levels in the airfoil's boundary layer which represents the true inflow condition to the finlets themselves.

5.3.4 Phased Microphone Array

Far-field sound produced by the trailing edge of the airfoil model was measured using a 117-microphone phased array system located in the starboard-side anechoic chamber and pointed towards the suction side of the airfoil with the projected center point of the array at the quarter-chord, mid-span point on the airfoil, as shown in Fig. 5.2. The microphones are Panasonic electret microphones of type WM-64PNT and are arranged in 9 spiral arms on a solid 1.1-m diameter carbon-fiber disk. Each microphone has a flat frequency response in the range of 20-16000 Hz, and the array was calibrated to within $\pm 5^\circ$ phase and 0.4 dB amplitude in the frequency range of 500-16000 Hz. The array's spot size, defined here as twice the distance from the center of a monopole source to the edge of the main lobe where the sound power drops to 10 dB below the maximum, is approximately 1 m at a frequency of 1 kHz, 0.5 m at 2 kHz, and 0.2 m at 5 kHz. The various effects of the flow and facility,

including boundary layer refraction on the Kevlar wall, convective effects, pressure doubling due to the solid surface on which the microphones are mounted, and Kevlar attenuation have all been taken into account in post-processing of the data (see [22]).

To record the acoustic data, two 64-channel PCI-based data acquisition cards collected data at 51200 Hz for 32 seconds. The data were passed through a 20-kHz anti-aliasing filter. Spectral data was produced by averaging Fourier transforms of blocks of 8192 samples. The data processing included diagonal-removal of the cross-spectral matrix to eliminate uncorrelated noise in the beamformed maps. Integrated spectra were computed by adding the contributions of the trailing edge noise over a region encompassing the trailing edge. Only grid points with levels within 5 dB of the maximum level in the region were integrated in order to eliminate the influence of side lobes, and this sum was normalized on the integrated point spread function for a point at the center of the integrated region. The integration region was chosen to fully capture the effect of the treatment while minimizing contributions from the untreated sections of the airfoil.

5.3.5 Fluctuating Surface Pressure Instrumentation

To sense surface pressure fluctuations near the trailing edge and (when treatments were applied) between the finlets, ten Knowles electret microphones of type FG-23742-C05 were incorporated into the airfoil model. These microphones featured a circular sensing area 0.76 mm in diameter and had a flat frequency response in the range of 100-10000 Hz. Calibrations were performed for each microphone to account for the frequency response up to 20 kHz, and to determine the phase response. Data from each microphone was collected using two 6-channel Bruel and Kjaer Type 3050 24-bit LAN-XI modules sampling at 65536 Hz. Spectral data were produced by averaging Fourier transforms of blocks of 2048 samples using a Hanning window with 50% overlap between blocks. Uncertainty in these measurements, considering contributions from the microphones and the processing techniques, was approximately 1-2 dB.

All microphones were placed 22.4 mm upstream of the trailing edge at the 97% chord location. Five microphones were placed on the suction side of the airfoil, while the other five were placed on the pressure side. Four microphones on each side were spaced 5 mm apart, while the fifth microphone was placed 10 mm from the nearest adjacent microphone. The positions were chosen such that the sensing area of each microphone would be centrally located in the gaps between adjacent finlets. This arrangement is shown in Figs. 5.7 and 5.8.

5.3.6 Simulation Setup and Conditions

As the goal of the flow simulation was to compare the flow over a DU96-W180 airfoil with and without finlets, separate meshes were generated for each of these cases. Mesh generation

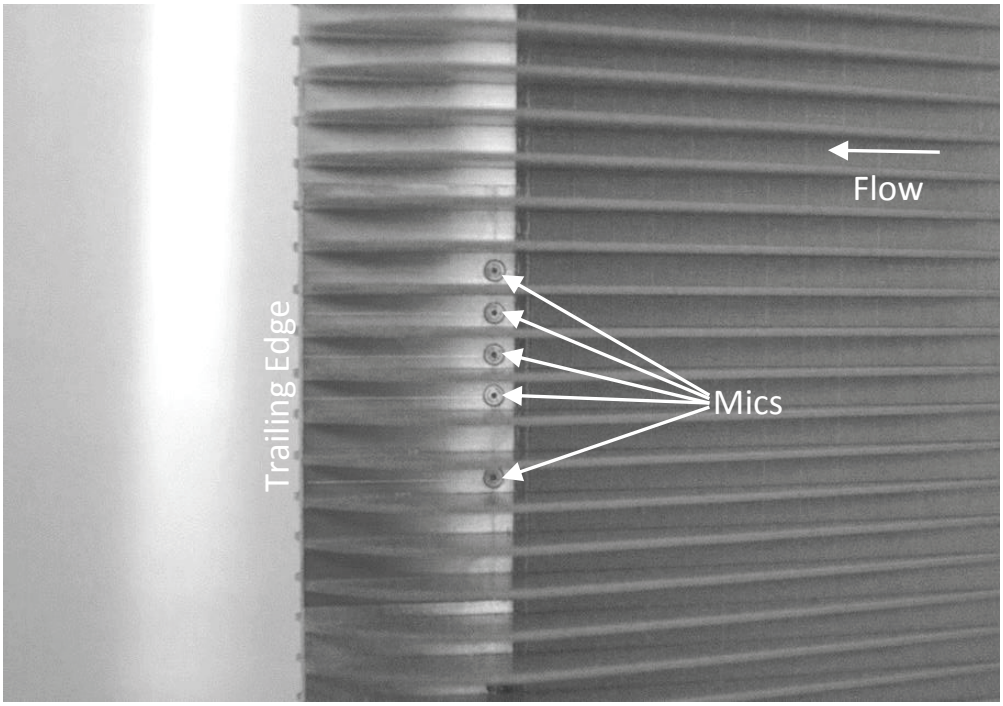

Figure 5.8: Photograph of finlets applied to the airfoil as seen from above the suction side of the airfoil, with microphones embedded in the airfoil surface between finlets.

was performed using the tools included in OpenFOAM version 2.4.0 [23]. The overall domain was chosen to have dimensions of 9 m in the streamwise direction and 6 m in the lift direction. The leading edge of the airfoil was placed 4 m downstream of the inlet of the domain and at the transverse center of the domain. These values were chosen to ensure that the influence of the presence of the airfoil would decay to a minimal amount before encountering the edge of the domain.

For the untreated airfoil, a two-dimensional mesh was generated which featured increasing numbers of cells near the trailing edge to properly resolve the flow in this region. Cells nearest the trailing edge had nominal dimensions of 0.16×0.16 mm. Far from the trailing edge, but still near the rest of the airfoil, cells had a nominal dimension of 1.25×1.25 mm with the addition of three thin viscous layers on the surface. The first viscous layer cell center was located 0.1 mm above the surface. The total number of cells in this mesh was on the order of 160,000.

For the treated airfoil, a full three-dimensional mesh was necessary to resolve the effects of the finlets. The mesh for this case is illustrated in Figs. 5.9 and 5.10. Because RANS simulations were chosen for this investigation, it was determined that simply modeling one "channel" with half of a finlet on either side would be sufficient to capture the flow phenomena of interest since time-averaged flow within the finlets was expected to be spanwise periodic. As the finlets were chosen to have a thickness of 1 mm and a spacing of 4 mm, the spanwise domain

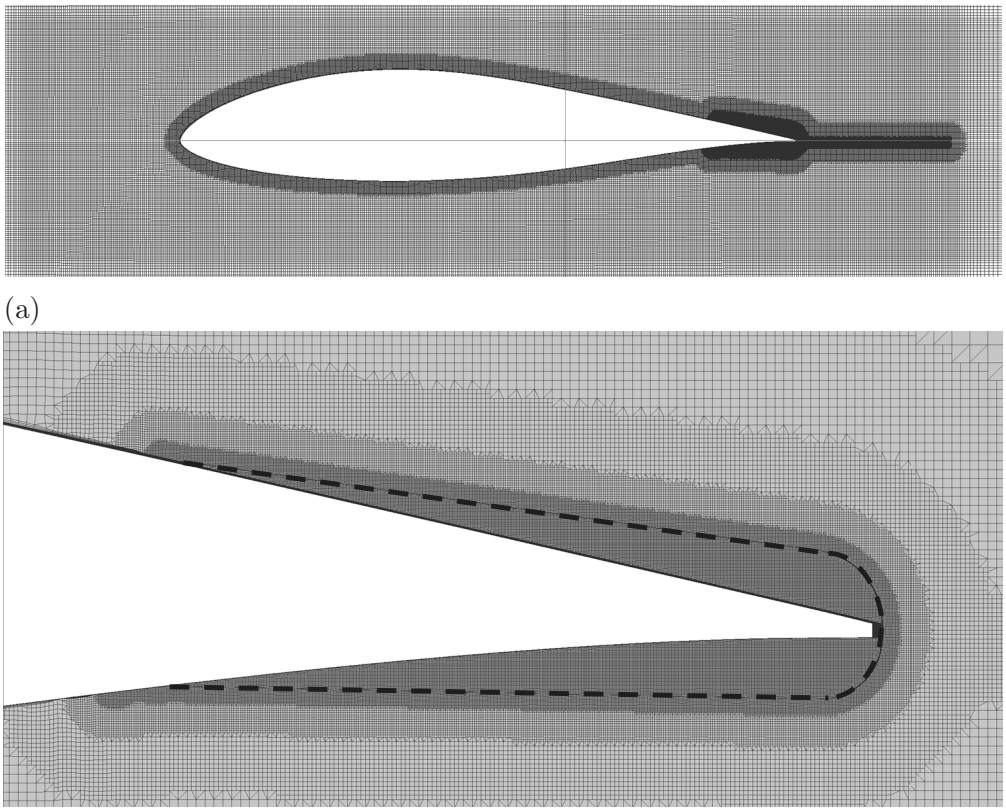

(a)

(b)

Figure 5.9: Side views of mesh. a) View of the full DU96 airfoil. The full mesh extended well beyond the view of this image as described in Section 5.3.6 b) Detailed view of the mesh near the finlets, denoted by the dashed lines.

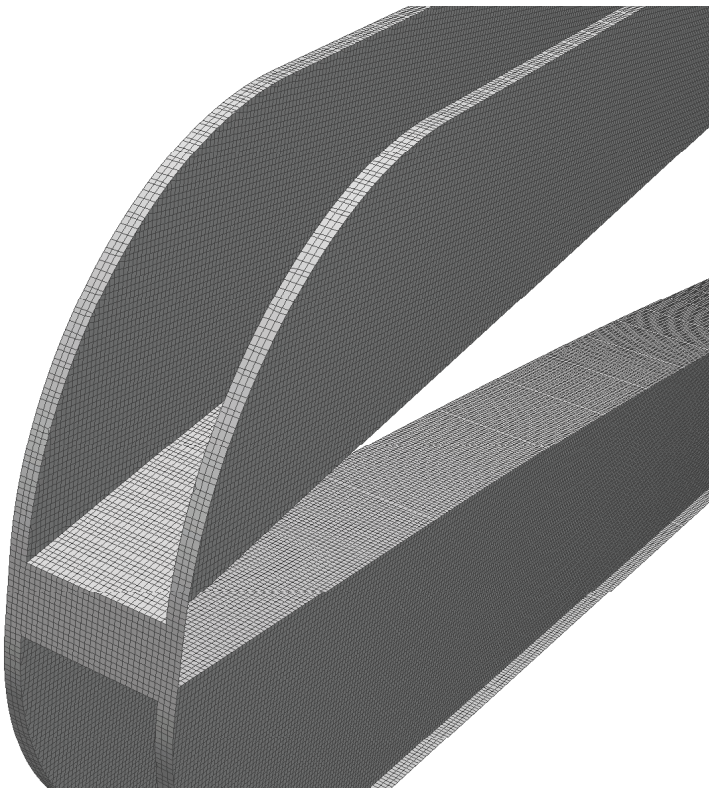

Figure 5.10: View of mesh near the finlets. The cell borders are drawn on the physical boundaries (airfoil and finlet surfaces) for visualization.

extended 5 mm. A periodic boundary condition was imposed on the spanwise boundaries. The nominal cell size in the region between and around the finlets was $0.16 \times 0.16 \times 0.16$ mm. This yielded six cells over the finlet thickness, twenty-six cells across the span in the space between the finlets, and fifty cells over the maximum height of the finlets from the airfoil surface. The total number of cells in the mesh was on the order of two million.

The simulation itself was run using OpenFOAM version 2.4.0 [23]. Flow conditions were chosen to match those of the experiment. The angle of attack of the airfoil was set at zero degrees. The free-stream velocity was chosen to be 50 m/s, and the initial/boundary turbulence kinetic energy value was chosen to correspond to a free-stream turbulence level of 0.03%. The turbulence integral lengthscale was set to an initial value of 0.1 m. For modeling of turbulence, the simulation used Menter's [24] $k - \omega$ SST model as it handles adverse pressure gradients reasonably well while avoiding over-sensitivity to free-stream conditions. The simulations were run for sufficient time to ensure residuals of all working variables were reduced below 10^{-4}.

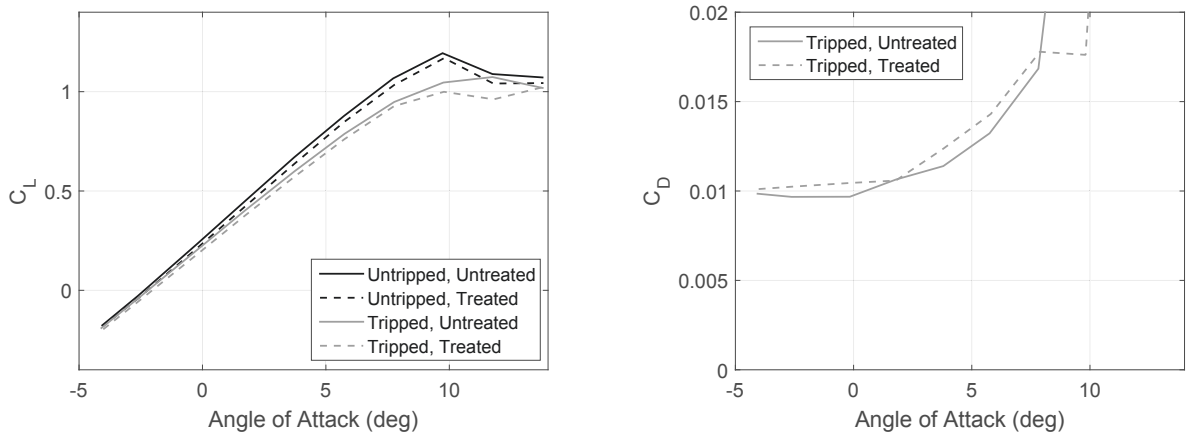

Figure 5.11: a) Lift and b) drag polars obtained from experiment.

5.4 Results and Discussion

The goal of this investigation is to build an understanding of the flow physics behind the noise reduction achieved by the finlets. The results of this study are therefore organized as follows. First, we present lift, drag, and mean pressure distributions obtained by both simulation and experiment. These integrated/steady quantities provide the best method for validating the simulation results. We then present computed boundary layer profiles and cross-sectional flow results near the trailing edge. Next we show experimentally measured surface pressure fluctuations, which can be considered to depend on the flow results just presented. Far-field noise are the final results shown, as they depend in turn on surface pressure fluctuations through the theory of Amiet [5, 25]. These results are therefore presented in comparison to those predicted using Amiet's theory with the surface pressure data collected during the experiment. All results were obtained for a free-stream velocity of 50 m/s corresponding to a Reynolds number of roughly 2.5 million and a Mach number of about 0.15. Simulation results were obtained for an angle of attack of zero degrees, while the experimental results were obtained for a tunnel-corrected angle of attack of -0.2 degrees, unless otherwise specified.

5.4.1 Lift, Drag, and Mean Surface Pressure

We first present results of lift, drag, and mean surface pressure to demonstrate the effects of the finlets on aerodynamic performance and to validate the results of the simulation by comparing with experimental results. The RANS simulation models a turbulent boundary layer over the entirety of the airfoil, but the results will nonetheless be compared to both the untripped and tripped airfoil experiments to build a complete picture of the level of agreement between the two investigative methods.

Table 5.1: Lift and drag results at zero degrees angle of attack.

	Lift			Drag	
	Simulation	Experiment (Untripped)	Experiment (Tripped)	Simulation	Experiment (Tripped)
Airfoil Only	0.243	0.26	0.225	0.0107	0.0097
Airfoil with Finlets	0.225	0.235	0.203	0.0112	0.0104

Figure 5.11 shows the lift and drag polars for the DU96 airfoil with and without finlets as measured during the experimental portion of the study. Comparing first the untreated airfoils, it is observed that the tripped airfoil generates less lift over all angles of attack. This is not unusual, as the trip strip interferes with the natural flow over the airfoil. The finlets are observed to reduce the lift curve slope for both the untripped and tripped airfoils. Due to constraints during testing, drag data was only obtained with the airfoil tripped. The finlets are seen to produce a significant (5-8%) increase in drag across the full angle of attack range.

Because the simulation was performed at an angle of attack of zero degrees only, no lift or drag polars are available. Table 5.1 shows results of the simulation for lift and drag, compared with experimental results interpolated to zero degrees angle of attack. The simulated results for lift fall within the range observed in experiment between the tripped and untripped cases. The simulation predicts a lift reduction due to the finlets of 7.4%, while the experiment shows a 9.6% decrease in lift for both the untripped and tripped cases. The simulation over-predicts the drag by approximately 8-10% relative to the experimentally measured values. Considering only the effect of the finlets, the increase in drag due to the finlets is predicted to be 4.7% while the experiment shows a drag increase of 7.2%. Overall, these values suggest that the simulation captures the dominant effect of the finlets on the flow over the airfoil.

Finally, mean pressure distributions can be considered to further isolate the effect of the finlets. Figure 5.12 shows results for the pressure distribution at zero degrees angle of attack, both for the simulation and for the interpolated experimental results. In all cases, the finlets are observed to slightly increase C_p on the suction side of the airfoil while significantly decreasing C_p on the pressure side near the trailing edge. The decrease in lift therefore comes almost entirely from the treated region of the airfoil, with some slight contribution from the area upstream of the finlets on the suction side. Again, the qualitative agreement between the computational and experimental results shows that the simulation captures the relevant flow physics affecting the flow on both sides of the airfoil. It is seen from the experimental results that the finlets have significantly different effects on the flow on the pressure and suction sides. The simulation captures this phenomenon as well, which allows for these results to be used in further analysis.

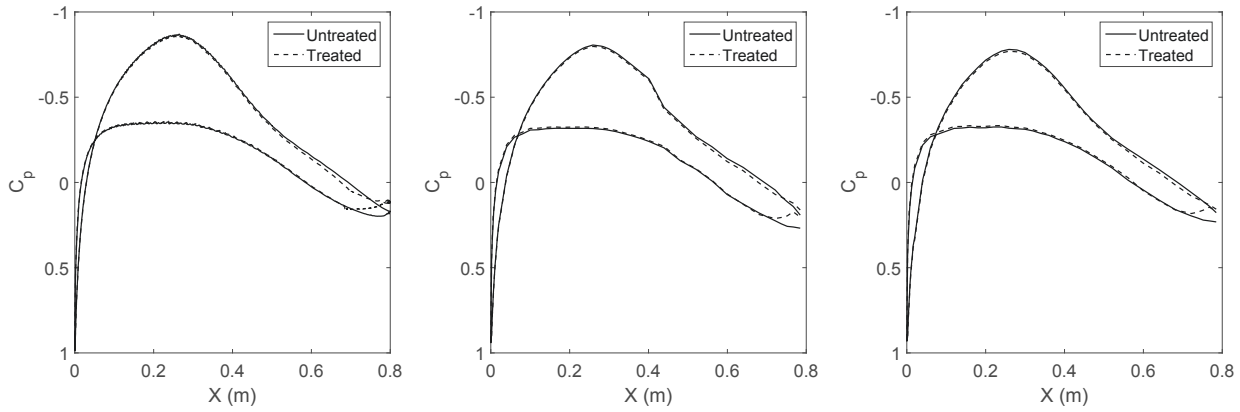

(a) (b) (c)

Figure 5.12: Mean pressure distribution as obtained from a) simulation, b) experiment with untripped airfoil, and c) experiment with tripped airfoil.

5.4.2 Computational Flow Field Results

We now shift our attention to the flow field results obtained by the simulation. We focus our attention first on boundary layer profiles near the trailing edge. In this way, we obtain a first look at the influence of the finlets on the flow most responsible for trailing edge noise. Boundary layer profiles are obtained by sampling a vertical line of points at the center of the channel at the streamwise location of maximum finlet height (see Figure 5.6).

Figure 5.13 shows profiles of both velocity and turbulence kinetic energy (TKE) normalized on free-stream velocity obtained on the suction and pressure sides of the airfoil. On the suction side, the effect of the finlet is marked by a reduction of flow velocity which extends through the majority of the boundary layer (approximately 20 mm). The velocity profile near the wall appears to be close to separation, and an inflection point is observed near approximately 3 mm above the surface. However, it is noted that no flow reversal or separation was observed at any point. Turbulence kinetic energy profiles followed a similar trend. Without finlets, the peak TKE occurred near 10 mm above the surface. With finlets, the location of maximum TKE appeared to be shifted away from the surface by approximately 4 mm. The peak level experienced a minimal reduction.

The pressure side results are quite different from those of the suction side. The finlets have almost no effect until approximately 12 mm above the surface, at which point velocity increases above the untreated level. It is hypothesized that the flow is unaffected by the finlets for two reasons. The first is the higher velocity in the lower part of the boundary layer, corresponding to a lower displacement thickness compared to the suction side. This equates to more momentum in the flow near the wall, and less time for the viscous effect of the finlet to retard the flow. The second reason is the more favorable pressure gradient present on the pressure side of the airfoil which allows the flow to maintain its momentum

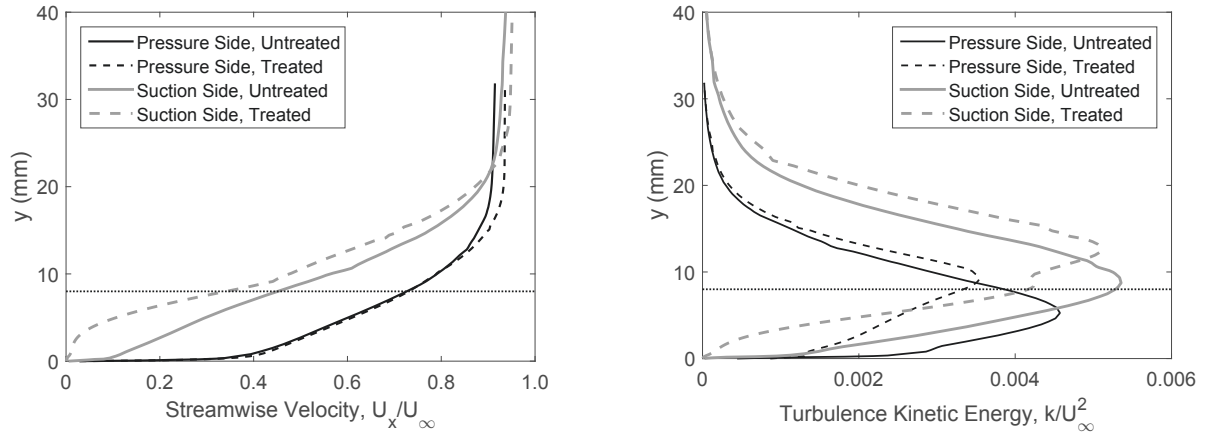

(a) (b)

Figure 5.13: Computed boundary layer profiles of a) velocity and b) turbulence kinetic energy obtained from the center of the finlet channel at the location of maximum finlet height. The dotted line at $y = 8$mm denotes the top of the finlet.

through the channel. Interestingly, even with almost no effect on velocity, the finlets appear to have a strong effect on turbulence kinetic energy. Levels of TKE are reduced by almost half in the region below the maximum finlet height. The peak value is reduced by over 20% and shifted in location to nearly double its previous height above the surface.

Figure 5.14 shows plots of the streamwise velocity and turbulence kinetic energy in the channel between the finlets on the suction and pressure sides. The plots reveal that the suction side velocity profile is relatively constant across the span, but all other quantities show significant deviation from their center values. The TKE on the suction side is clearly lower near the finlets than at the center of the channel. The streamwise velocity on the pressure side shows significant drop-off away from the channel center. The pressure side TKE displays a somewhat unusual profile. The values are relatively constant across the span in the lower half of the channel. However, high levels of TKE are observed near the finlets in the upper half of the channel, with lower values near the center.

5.4.3 Experimental Surface Pressure Results

In this section, we consider two sets of results obtained from the surface pressure microphones mounted in the airfoil. The first set comprises the surface pressure fluctuation spectra, obtained by averaging the spectra obtained by each microphone on a given side of the airfoil and for a single test condition (50 m/s, -0.2 degrees angle of attack). The second set comprises Amiet's [5] spanwise correlation lengthscales obtained using Equation 5.1.

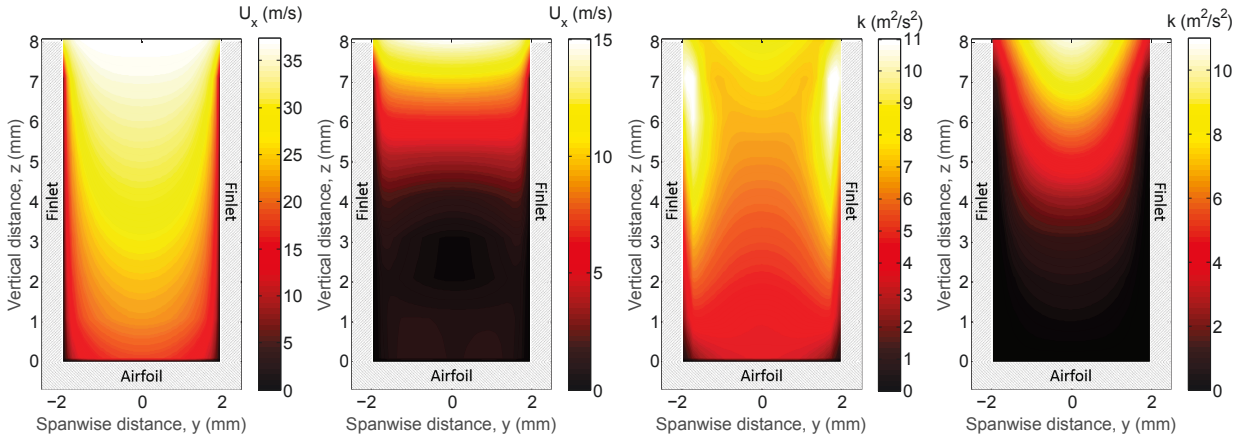

Figure 5.14: Cross-sectional views of velocity and turbulence kinetic energy in the finlet channel at the location of maximum finlet height. a) Streamwise velocity computed on pressure side. b) Streamwise velocity computed on suction side. c) Turbulence kinetic energy computed on pressure side. d) Turbulence kinetic energy computed on suction side.

$$l_y(\omega) = \frac{1}{S_{qq}(\omega, 0)} \int_0^\infty S_{qq}(\omega, y) dy \tag{5.1}$$

In this equation, $S_{qq}(\omega, y)$ represents the cross-spectra from the surface pressure microphones which depend on angular frequency and spanwise separation between microphones. Length-scales were integrated from the measured spanwise surface pressure cross-spectra at low frequencies where the integrand was well-defined and supplemented at high frequencies using Amiet's empirical relation $l_y(\omega) = aU_c/\omega$. Here, a is a constant given as 2.1 by Amiet, but this value was modified in the present work to fit the particular data set to which the model was blended. Choice of the parameter α ranged from 0.6-0.7 for cases with finlets applied, to 1-1.2 for cases without finlets. For all data sets, the model and data were blended in the range of 1-2 kHz, with pure data being used below 1 kHz and the pure model being used above 2 kHz.

Figure 5.15 shows the surface pressure spectra as described above for each of the configurations tested, and for the pressure side and suction side of the airfoil. It can be seen from these plots that there is no universal effect of the finlets. Rather, the behavior of the surface pressure spectra in response to the finlets is highly dependent on other factors, namely which side of the airfoil is considered and whether the airfoil is tripped or untripped. Considering first the pressure side, it can be seen that the finlets have a tendency to increase the magnitude of surface pressure fluctuations, an effect that is more pronounced on the untripped airfoil. In contrast, on the suction side, the finlets tend to reduce the magnitude of the fluctuations by up to 4 dB, with the exception of the low frequency fluctuations on the tripped airfoil.

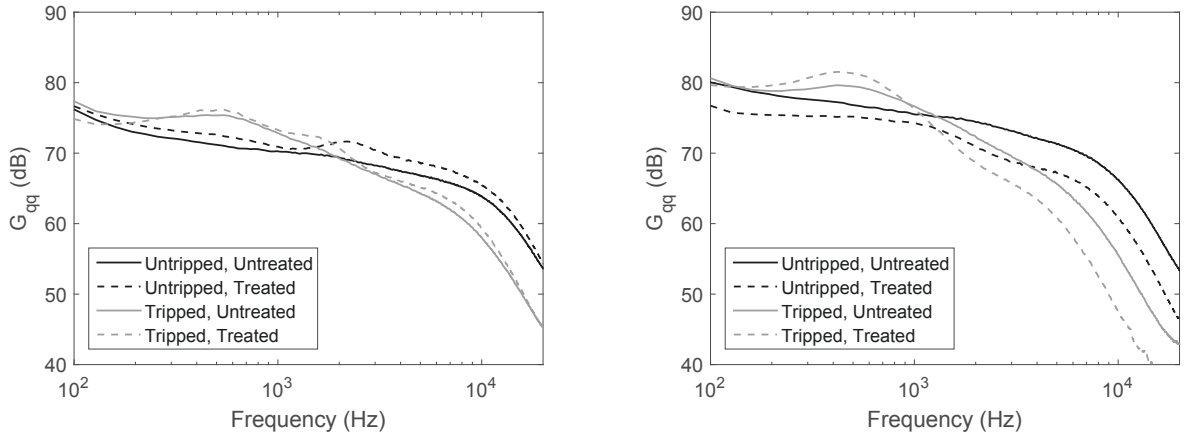

(a) (b)

Figure 5.15: Average surface pressure spectra measured on the a) pressure and b) suction sides of the airfoil.

These results, when combined with the flow field results of Section 5.4.2, suggest that the surface pressure fluctuations are influenced most significantly by the velocity deficit produced by the finlets. The suction side finlets exhibit a severe reduction in velocity in the lower boundary layer, and the corresponding pressure fluctuation magnitude is reduced over almost all frequencies. Conversely, the pressure side finlets had little to no impact on the boundary layer profile, and as such pressure fluctuations stayed the same or slightly increased. Of course, the influence of turbulence kinetic energy cannot be ignored. It is possible that the peaks in turbulence kinetic energy observed on the pressure side contribute to the increase in surface pressure magnitude compared to the untreated case.

Figure 5.16 shows spanwise correlation lengthscale results determined using the method described above. Here, the influence of the finlets appears to be more consistent. On the untripped airfoil, the lowest frequency lengthscales are largely unmodified on the pressure side but experience a strong increase on the suction side. On the tripped airfoil, the finlets cause a modest increase in the correlation lengthscale at the lowest frequencies (below 300 Hz), but yield a reduction in lengthscales at all other frequencies. The reduction observed at higher frequencies begins at about 400 Hz on the pressure side and at about 700 Hz on the suction side. Finally, it is worth noting that the shifts in location of the peaks in lengthscale may be caused by an increase in the boundary layer displacement thickness by the finlets.

At this point, several additional comments can be made regarding the effects of the finlets by combining the surface pressure results just presented with the flow results of Section 5.4.2. Considering first the suction side of the airfoil with finlets applied, it can be seen that the boundary layer profile displays a significant velocity deficit throughout much of the boundary layer compared to the untreated case. This deficit naturally leads to a decrease

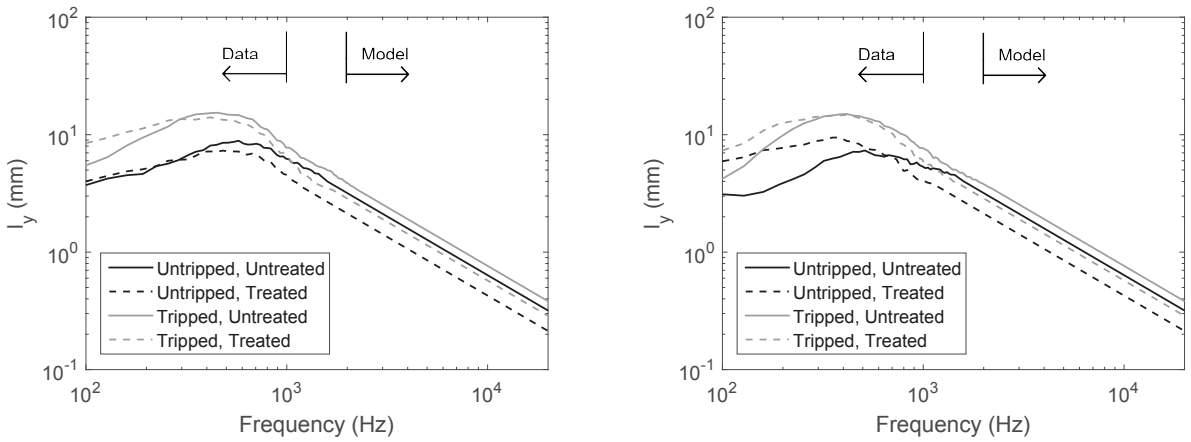

(a) (b)

Figure 5.16: Spanwise lengthscale measured on the a) pressure and b) suction sides of the airfoil.

in the convection velocity of the eddies in the lower boundary layer, particularly the small eddies near the surface which are responsible for the mid- to high-frequency fluctuations. This phenomenon was observed by Afshari *et al.* [20]. The current data suggests that the turbulent eddies which exist primarily in the channel between the finlets are damped by the decreased flow velocity (which contains less energy available for conversion to turbulence). In addition, the presence of the walls of the channels formed by the finlets likely contributes to this damping by suppressing spanwise velocity fluctuations. This leads to a reduction in surface pressure magnitude, precisely as observed in Figure 5.15, as well as a decorrelation of spanwise-organized turbulent structures, as observed in Figure 5.16.

The low-frequency differences in the untripped and tripped cases may be related to the difference in boundary layer thickness of the two cases. The boundary layer thickness would be expected to be higher for the tripped airfoil, which would increase the maximum size of eddies present in the boundary layer, as seen in Figure 5.16. The large eddies may then be at least partially contained in a region of the boundary layer not influenced by the finlets. The larger eddies in the tripped case may "override" the finlets entirely, leading to very little change in the low frequency fluctuations as observed in Figures 5.15 and 5.16. In the untripped case, however, the smaller eddies would feel more influence from the finlets, leading to larger changes in surface pressure and lengthscale as seen in Figures 5.15 and 5.16.

On the pressure side, the effect of the finlets is somewhat different. It was seen from the computational results that the finlets had little effect on the channel-center boundary layer profile. No large velocity deficit was present on the pressure side as there was on the suction side. However, the flow contours suggest boundary layers forming on the finlets themselves leading to "hot spots" of turbulence kinetic energy close to the finlets. This suggests that the

additional turbulence generated near the finlets themselves contributes to the slight increase in surface pressure fluctuations observed in Figure 5.15. However, it is expected that this additional turbulence would be correlated over a negligible spanwise distance, leading to a decrease in spanwise correlation lengthscale as observed in Figure 5.16. It is therefore expected that this additional turbulence actually contributes little to the total far-field noise from the trailing edge of the airfoil. This additional turbulence might be a source of edge noise from the tops of the finlets themselves, but no evidence of this was observed in noise measurements.

5.4.4 Trailing Edge Noise

We begin our discussion of measured noise results with acoustic beamform maps obtained from the 117-microphone phased array. Figure 5.17 shows these maps for both the untripped and tripped airfoils with and without finlets applied. The trailing edge noise is clearly visible in the acoustic source maps, shown here for 3 kHz, with levels exceeding 10 dB above the surrounding background noise. Comparing the untripped and tripped airfoils, the tripped airfoil is observed to be quieter at this frequency. Note that some noise appears to be visible at the leading edge, particularly in the tripped case where trailing edge noise levels are lower, but this is believed to be wind tunnel background noise scattered from the round leading edge, and not an airfoil source. The treatment (denoted as the dash-dot lines in Fig. 5.17) is seen to decrease the level of trailing edge noise by nearly 10 dB, or at least to the level of background noise in the facility.

Rather than presenting numerous beamform maps for every test condition and many frequencies, the maps were integrated for frequencies from 500 Hz to 5000 Hz using the methods described in Section 5.3.4 over the area shown in the dashed lines in Fig. 5.17. This range corresponds to a non-dimensional frequency range calculated from airfoil chord and free-stream velocity of $fc/U_\infty = 8$ to 80. The uncertainty of the array results is estimated to be less than 3 dB for frequencies below 4 kHz, and uncertainty rises above this level at higher frequencies due to decreasing absolute levels and background noise contamination. Figure 5.18 shows the results of this integration as 1/12th octave band spectral levels for each of the test conditions. The treatment is seen to be effective over a wide frequency range between 1 and 5 kHz. The maximum attenuation is seen to occur near 2750-3000 Hz ($fc/U_\infty = 44 - 48$), with a SPL reduction of approximately 10 dB for both untripped and tripped configurations. The treatment appears to slightly enhance trailing edge noise at the lowest frequencies below 1 kHz ($fc/U_\infty < 16$).

For further analysis, Amiet's theory [5, 25] can be used as a framework to evaluate the expected change in sound level due to the presence of the finlets and their corresponding effect on the surface pressure autospectra and spanwise correlation lengthscale. Since the quantity of interest is the change in sound pressure level on a decibel scale, many of the factors in the Amiet's theory which are common between the untreated and treated cases

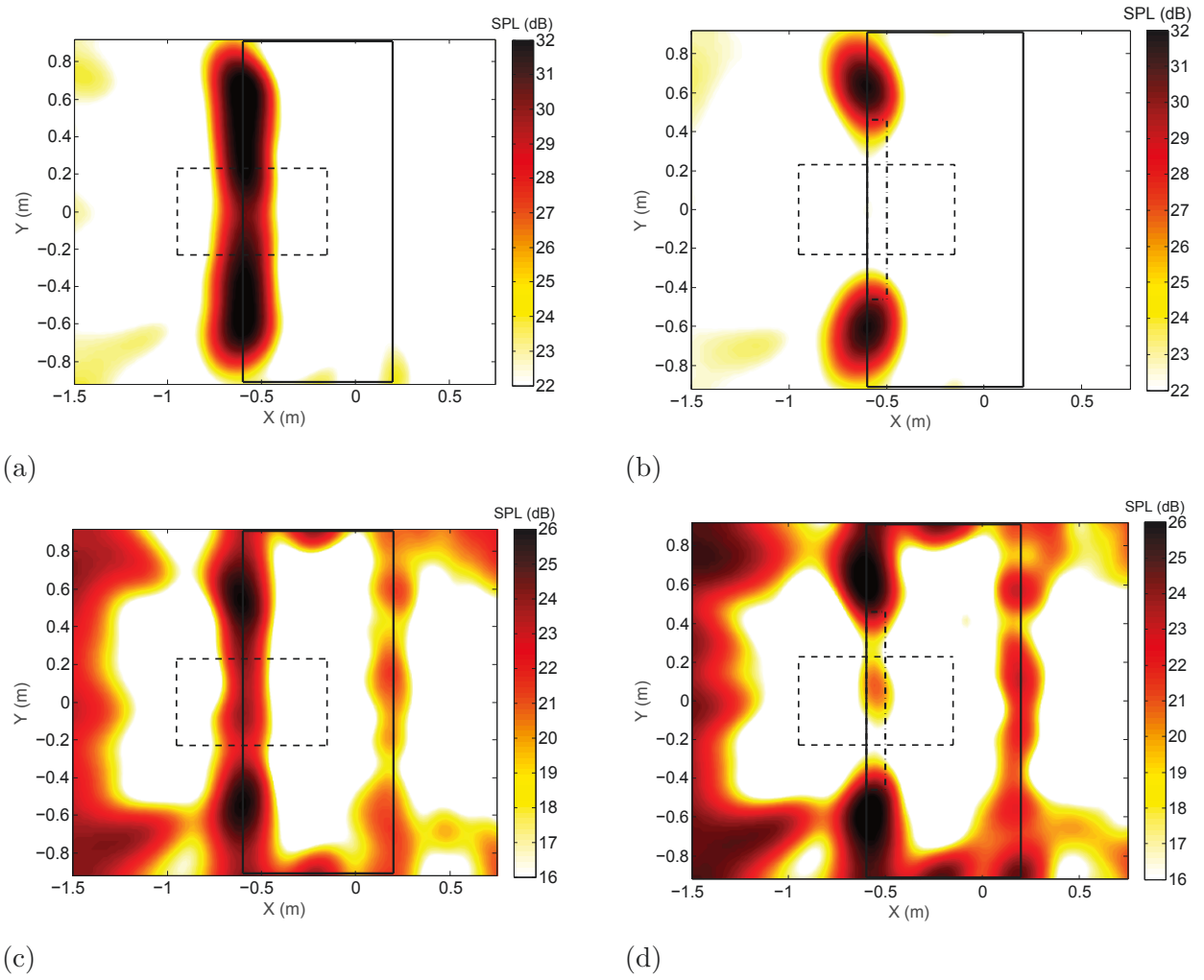

Figure 5.17: Beamform maps of 3 kHz noise measured by the phased array. Flow is from right to left. The solid rectangle denotes the location of the airfoil. The dashed rectangle denotes the integration used for subsequent analysis. The dash-dot line in subfigures b) and d) denote the location of the treatment. a) Untripped, untreated airfoil. b) Untripped, treated airfoil. c) Tripped, untreated airfoil. d) Tripped, treated airfoil.

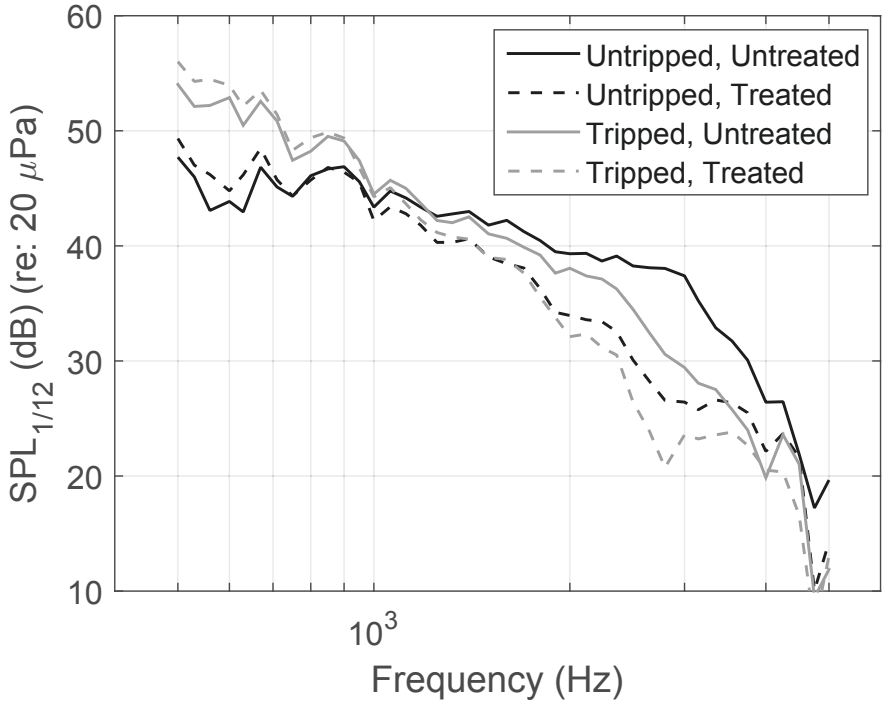

Figure 5.18: Noise spectra in 1/12th octave bands obtained by integrating over the region shown in Figure 5.17.

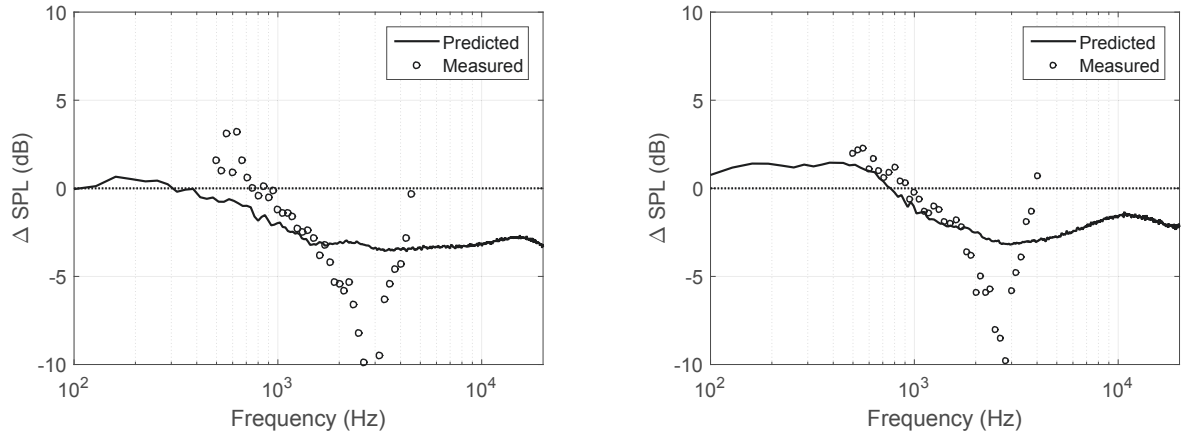

(a) (b)

Figure 5.19: The change in noise level predicted by the theory of Amiet using data from the surface pressure microphones compared to that measured by the phased array. a) Untripped airfoil. b) Tripped airfoil.

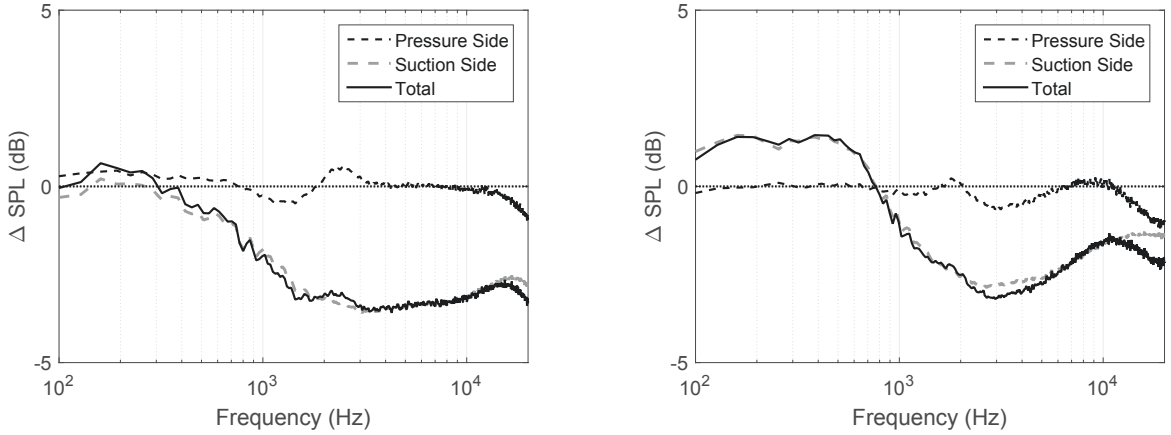

(a) (b)

Figure 5.20: The change in noise level caused by the pressure and suction side finlets predicted by the theory of Amiet using data from the surface pressure microphones. a) Untripped airfoil. b) Tripped airfoil.

cancel out, yielding equation 5.2.

$$\Delta SPL(\omega) = 10log_{10}\left(\frac{l_y^t(\omega)S_{qq}^t(\omega,0)}{l_y^u(\omega)S_{qq}^u(\omega,0)}\right) \tag{5.2}$$

In this equation, the superscripts t and u represent the treated and untreated cases, respectively. The change in measured noise level is plotted in Fig. 5.19 along with that predicted by Amiet's theory. It is observed that the trend in ΔSPL is matched between prediction and experiment at frequencies below 2 kHz ($fc/U_\infty < 32$). In both the untripped and tripped cases, Amiet's model seems to over-predict the noise reduction actually achieved by the finlets below 2 kHz. Above this frequency, measured noise reduction suddenly greatly exceeds that implied by the theory. It is worth noting that, above 2 kHz, no data is available for spanwise correlation lengthscale, and the simple model fit to the data may not capture the true extent to which spanwise correlation lengthscale is reduced by the finlets.

The use of Amiet's theory can be taken a step further by considering separately the contributions of the suction and pressure side finlets in reducing the noise. Figure 5.20 shows the results of this analysis. The pressure side finlets appear to have almost no effect on the noise generated by the untripped airfoil, but they do have a marginal effect on that generated by the tripped airfoil. The majority of the observed change comes from the suction side finlets. However, this contradicts the findings of Clark *et al.* [19] which showed that noise attenuation was significantly greater when finlets were applied to both the pressure and suction sides, compared to the suction side alone. It is believed, therefore, that the results of Amiet's model may be somewhat misleading in this case. As described in Section 5.4.3, an increase

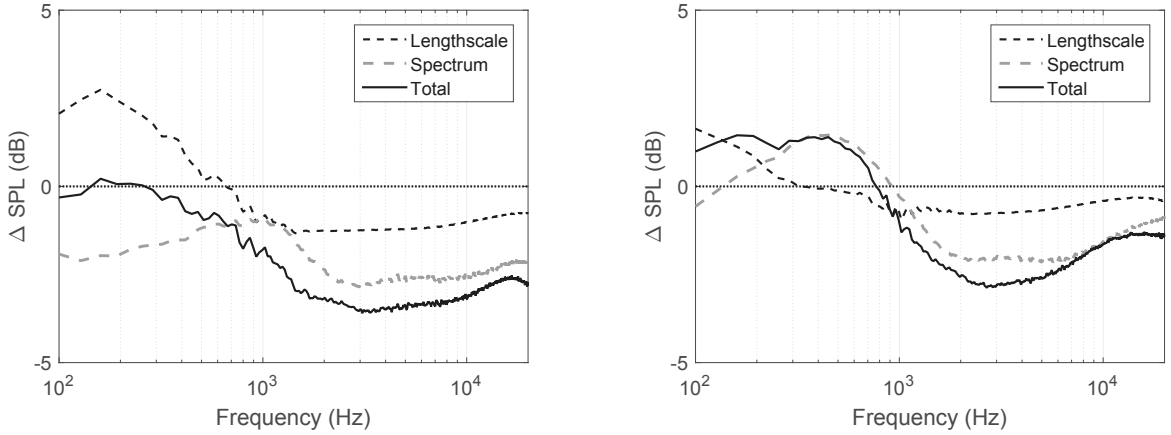

(a) (b)

Figure 5.21: The change in noise level caused by changes to the spanwise correlation lengthscale and surface pressure spectrum on the suction side finlets predicted by the theory of Amiet using data from the surface pressure microphones. a) Untripped airfoil. b) Tripped airfoil.

in magnitude of the surface pressure fluctuations was observed on the pressure side, but this was believed to be due to the formation of boundary layers on the finlets themselves. As any turbulence here would not be correlated between adjacent finlets, this would contribute little to the overall far-field noise. In addition, this turbulence may interact with the turbulence already present in the airfoil boundary layer, thereby decreasing the spanwise correlation lengthscale in the airfoil boundary layer. In this way, the pressure side finlets may significantly reduce the scattered trailing edge noise generated by the pressure side boundary layer, despite only modest indications of this in measured surface pressure data.

The final step taken with Amiet's theory is to distinguish the influence of the change in spanwise correlation lengthscale and the change in surface pressure spectrum on the far-field noise. This analysis is performed for the suction side and the results are shown in Fig. 5.21. In the tripped case, it can be seen that the increase in low frequency noise is actually caused by both components acting in separate frequency ranges. Below 200 Hz, the noise increase is due to an increase in the spanwise lengthscale of turbulent pressure fluctuations, whereas between 200 and 700 Hz, the noise increase is due primarily to an increase in the magnitude of surface pressure fluctuations. The noise reduction at higher frequencies is seen to be caused by both factors working together. In the untripped case, at frequencies below 500 Hz, the influences of the lengthscale and magnitude of fluctuations are seen to cancel out, leading to very little change in the far-field noise. As with the tripped case, both factors contribute to noise reduction at higher frequencies.

5.5 Summary and Conclusions

The present work aims to build understanding of the fluid mechanics behind noise attenuation observed with the use of finlets on a DU96-W180 airfoil. Complementary investigations were performed utilizing a RANS simulation and an experiment in the Virginia Tech Stability Wind Tunnel. The RANS simulation produced flow data in the channel between the finlets, which was used to gain insight into the results of unsteady pressure and trailing edge noise obtained in the experiment. Simulation results were validated with lift, drag, and mean pressure distribution results which were obtained by both the simulation and experiment. The theory of Amiet [5, 25] for relating trailing edge noise to unsteady surface pressure was used to gain insight into how the finlets affected the turbulence in the boundary layer of the airfoil near the trailing edge.

Clear differences in the finlets' effects were seen between the suction and pressure sides of the airfoil. The suction side finlets produced a significant velocity deficit in the boundary layer relative to the airfoil with no finlets. This corresponded to a decrease in the magnitude of surface pressure fluctuations. This suggests that the turbulent eddies in the boundary layer are suppressed between the finlets, leading to a far-field noise reduction. The pressure side finlets did not yield a significant velocity deficit, however they did show evidence of boundary layers forming on the finlets themselves. The data suggests that these boundary layers are sources of additional turbulence which increases the magnitude of surface pressure fluctuations. However, this turbulence is not correlated over the span of the airfoil and so contributes little to the far-field sound. The presence of this turbulence may influence the turbulence already present in the airfoil's boundary layer, thereby decorrelating organized turbulent structures in the flow which would otherwise contribute more significantly to the trailing edge noise. Although this yields some benefit to noise reduction, it may be possible to maximize noise attenuation by refining the design of the pressure side finlets such that they have a flow effect which is more similar to that observed on the suction side.

The measured trailing edge noise was linked to surface pressure measurements through the theory of Amiet. Analysis indicated that the theory captured the general trend of noise reduction particularly in the frequency range below 2 kHz with the model under-predicting noise attenuation at frequencies higher than 2 kHz. The theory indicated that the suction side finlets were responsible for almost all of the noise attenuation, a result contradicted by previous experimental results. It is suspected that the surface pressure measurements were influenced by uncorrelated turbulence generated by the finlets themselves, leading to this result. Finally, the theoretical results showed competing influences of reducing surface pressure magnitude and correlation lengthscale at low frequencies. At higher frequencies, both surface pressure and lengthscale were reduced and therefore contributed to the overall noise attenuation.

5.6 Acknowledgments

The authors would like to sincerely thank the Institute of Critical Technology and Applied Science at Virginia Tech for their support of this work. The authors would also like to thank the Office of Naval Research for their support under grants N00014-15-1-2721, N00014-14-1-0141, and N0001401602395. The authors acknowledge Advanced Research Computing at Virginia Tech for providing computational resources and technical support that have contributed to the results reported within this paper. The authors are grateful to Dr. Stewart Glegg for many helpful discussions over the course of this work.

References

[1] Schmidt, J. H. and Klokker, M., "Health Effects Related to Wind Turbine Noise Exposure: A Systematic Review," *PLoS ONE*, Vol. 9, No. 12, dec 2014, pp. 1–28.

[2] Doolan, C., "A Review of Wind Turbine Noise Perception, Annoyance and Low Frequency Emission," *Wind Engineering*, Vol. 37, No. 1, feb 2013, pp. 97–104.

[3] Oerlemans, S., Sijtsma, P., and Méndez López, B., "Location and quantification of noise sources on a wind turbine," *Journal of Sound and Vibration*, Vol. 299, No. 4-5, 2007, pp. 869–883.

[4] Ffowcs Williams, J. E. and Hall, L. H., "Aerodynamic sound generation by turbulent flow in the vicinity of a scattering half plane," *Journal of Fluid Mechanics*, Vol. 40, No. 4, 1970, pp. 657–670.

[5] Amiet, R. K., "Noise due to turbulent flow past a trailing edge," *Journal of Sound and Vibration*, Vol. 47, No. 3, aug 1976, pp. 387–393.

[6] Howe, M. S., "A Review of the Theory of Trailing Edge Noise," *Journal of Sound and Vibration*, Vol. 61, No. 3, 1978, pp. 437–465.

[7] Brooks, T. F. and Hodgson, T. H., "Trailing Edge Noise Prediction From Measured Surface Pressures," *Journal of Sound and Vibration*, Vol. 78, No. 1, 1981, pp. 69–117.

[8] Brooks, T. F., Pope, D. S., and Marcolini, M. A., "Airfoil Self-Noise and Prediction," Tech. rep., NASA, 1989.

[9] Howe, M., "Trailing Edge Noise at Low Mach Numbers," *Journal of Sound and Vibration*, Vol. 225, No. 2, 1999, pp. 211–238.

[10] Howe, M. S., "Aerodynamic Noise of a Serrated Trailing Edge," *Journal of Fluids and Structures*, Vol. 5, 1991, pp. 33–45.

[11] Oerlemans, S., Fisher, M., Maeder, T., and Kögler, K., "Reduction of Wind Turbine Noise Using Optimized Airfoils and Trailing-Edge Serrations," *AIAA Journal*, Vol. 47, No. 6, 2009, pp. 1470–1481.

[12] Herr, M. and Dobrzynski, W., "Experimental Investigations in Low-Noise Trailing Edge Design," *AIAA Journal*, Vol. 43, No. 6, 2005, pp. 1167–1175.

[13] Sarradj, E., Fritzsche, C., and Geyer, T., "Silent Owl Flight: Bird Flyover Noise Measurements," *AIAA Journal*, Vol. 49, No. 4, 2011, pp. 769–779.

[14] Graham, R. R., "The silent flight of owls," *The Journal of the Royal Aeronautical Society*, Vol. 38, 1934, pp. 837–843.

[15] Kroeger, R. A., Grushka, H. D., and Helvey, T. C., "Low Speed Aerodynamics for Ultra-Quiet Flight," Tech. rep., Air Force Flight Dynamics Laboratory, 1972.

[16] Jaworski, J. W. and Peake, N., "Aerodynamic noise from a poroelastic edge with implications for the silent flight of owls," *Journal of Fluid Mechanics*, Vol. 723, 2013, pp. 456–479.

[17] Clark, I. A., Daly, C. A., Devenport, W., Alexander, W. N., Peake, N., Jaworski, J. W., and Glegg, S., "Bio-inspired canopies for the reduction of roughness noise," *Journal of Sound and Vibration*, Vol. 385, 2016, pp. 33–54.

[18] Lilley, G., "A study of the silent flight of the owl," *4th AIAA/CEAS Aeroacoustics Conference*, American Institute of Aeronautics and Astronautics, Toulouse, France, jun 1998.

[19] Clark, I., Baker, D., Alexander, W. N., Devenport, W. J., Glegg, S. A., Jaworski, J., and Peake, N., "Experimental and Theoretical Analysis of Bio-Inspired Trailing Edge Noise Control Devices," *22nd AIAA/CEAS Aeroacoustics Conference*, American Institute of Aeronautics and Astronautics, Lyon, France, may 2016.

[20] Afshari, A., Azarpeyvand, M., Dehghan, A., and Szoke, M., "Trailing Edge Noise Reduction Using Novel Surface Treatments," *22nd AIAA/CEAS Aeroacoustics Conference*, American Institute of Aeronautics and Astronautics, Lyon, France, may 2016.

[21] Millican, A. J., Clark, I., Devenport, W., and Alexander, W. N., "Owl-Inspired Trailing Edge Noise Treatments: Acoustic and Flow Measurements," *55th AIAA Aerospace Sciences Meeting*, Grapevine, Texas, jan 2017, pp. 1–29.

[22] Devenport, W. J., Burdisso, R. A., Borgoltz, A., Ravetta, P. A., Barone, M. F., Brown, K. A., and Morton, M. A., "The Kevlar-walled anechoic wind tunnel," *Journal of Sound and Vibration*, Vol. 332, No. 17, 2013, pp. 3971–3991.

[23] Weller, H. G., Tabor, G., Jasak, H., and Fureby, C., "A tensorial approach to computational continuum mechanics using object-oriented techniques," *Computers in Physics*, Vol. 12, No. 6, 1998, pp. 620–631.

[24] Menter, F. R., "Two-equation eddy-viscosity turbulence models for engineering applications," *AIAA Journal*, Vol. 32, No. 8, aug 1994, pp. 1598–1605.

[25] Amiet, R. K., "Effect of the Incident Surface Pressure Field on Noise Due to Turbulent Flow Past a Trailing Edge," *Journal of Sound and Vibration*, Vol. 57, No. 2, 1978, pp. 305–306.

Chapter 6

Experimental Investigation of Bio-Inspired Finlets for the Reduction of Marine Propeller Noise

This chapter is comprised of sections of a manuscript to be submitted and presented at the 23rd AIAA/CEAS Aeroacoustics Conference in June of 2017. The work presented here is the experimental portion of the manuscript. The present author is named as first author of this manuscript. A computational study is planned for incorporation into the final manuscript, but this work is not being performed by the present author and so is not included here.

6.1 Abstract

A series of experiments has been performed to investigate the noise-reducing potential of bio-inspired finlets when applied to a 0.46 m diameter two-bladed marine propeller. Experiments were performed in the Virginia Tech Stability Wind Tunnel at inflow speeds of 10 to 20 m/s with the propeller rotating at 2000 revolutions per minute. Acoustic data was obtained using a 251-microphone phased array split in half, with each half of the array flanking the propeller during testing. Flow data was obtained using a hot-wire probe traversed just downstream of the propeller blades. Results indicate that the finlets are effective at reducing broadband noise from the propeller blades by up to 8 dB while increasing turbulence levels in the wake of the blades. This reduction in noise is attributed to the reductions in both turbulent boundary layer trailing edge noise as well as noise generated by the shedding of discrete vortices from the blunt trailing edges of the propeller blades. This combination of observations suggests that the finlets, while increasing turbulence levels overall, serve to restructure the turbulence and prevent the formation of large-scale coherent vortical structures responsible for high noise levels.

6.2 Introduction

The aerodynamic noise from fans and propellers is a significant problem for many applications and situations. At best, noisy fans are an annoyance for anyone nearby. At worst, the noise from propellers such as those on airplanes may decrease quality of life in communities surrounding airport. The noise from a fan or propeller may have several different sources depending on the particular geometry and flow involved. Two common sources of aerodynamic noise, particularly for large, slow-moving propellers (high Reynolds number, low Mach number) in relatively undisturbed inflow, are turbulent-boundary-layer-trailing-edge noise and trailing-edge-bluntness-vortex-shedding noise. The former, abbreviated TBL-TE noise or referred to simply as trailing edge noise, is caused by the interaction of turbulent eddies in the boundary layer of a propeller blade with the trailing edge of the blade which scatters the pressure fluctuations associated with these eddies into sound. The latter, abbreviated here as TEB-VS noise or referred to as bluntness noise, is caused by discrete vortices which are formed as the flow separates off of a blunt trailing edge. Both of these forms of noise have been studied experimentally by Brooks, Pope, and Marcolini [1].

Although it is certainly possible to reduce or eliminate TEB-VS noise by sharpening the trailing edge, this is not always feasible for a given application. This is particularly true of marine propellers, which must withstand heavy loading in a corrosive environment. This necessitates a structure with significant thickness along the blade trailing edge. In these situations, it becomes necessary to look for other solutions to the noise-control problem. Previous experimental and theoretical investigations have sought to modify the trailing edge in such a way as to eliminate vortex shedding and reduce TBL-TE noise. Trailing edge serrations [2, 3] are a commonly studied form of TBL-TE noise reduction. Trailing edge brushes [4] are a similar concept. Both act to modify the trailing edge geometry to reduce the efficiency of the unsteady pressure-scattering mechanism.

Novel solutions to the noise-control problem may be found by considering the anatomy of owls' wings, as these birds are known to fly silently and have therefore, through evolution, found ways to eliminate at least some of the known sources of aerodynamic noise over a wing. Graham [5] identified three unique features of owls' wings which suggests that they contribute to their ability to fly silently: a comb of evenly-spaced bristles along the leading edge of the wing investigated by Kroeger *et al.* [6], a poro-elastic trailing edge investigated by Jaworski and Peake [7], and a coating of fine, downy hairs on the suction-side surface of the feathers. Historically it has been supposed that the leading and trailing edge features are responsible for the majority of noise reduction. However, Lilley [8] determined that the leading and trailing edge features could not fully account for the low levels of noise emitted by owls' wings, and so by process of elimination the downy coating must modify the turbulence in the boundary layer of an owl's wing to reduce the source of trailing edge noise. This suggests that it may be possible to apply a similar feature to a man-made structure with the hopes of modifying the boundary layer turbulence to reduce trailing edge noise. This idea has been investigated experimentally and theoretically by Clark *et al.* [9, 10] on a stationary

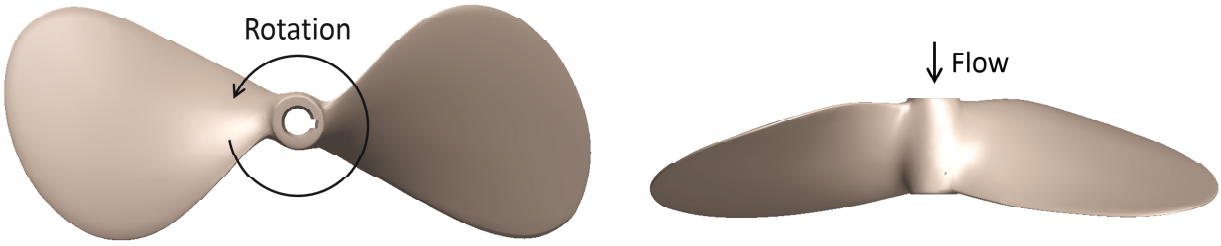

(a) Front View (b) Top View

Figure 6.1: CAD models of the propeller used in this experiment.

airfoil, and significant noise reductions of up to 10 dB have been measured.

The work described in the present paper applies the finlet concept of Clark *et al.* [9, 10] to a rotating system, specifically a marine propeller, to investigate the potential for noise reduction. Although the effectiveness of the finlets have been primarily demonstrated in the context of reducing TBL-TE noise, it is reasonable to surmise that they may also have a significant effect on TEB-VS noise by preventing the formation of large coherent vortex structures, simply due to the physical separation of flow regions by the presence of the finlets. In addition to noise measurements, detailed flow measurements are performed just downstream of the propeller in order to gather more information about the influence of the finlets on the flow.

6.3 Apparatus and Instrumentation

6.3.1 Wind Tunnel and Propeller

The experiment was performed in the Virginia Tech Stability Wind Tunnel. This facility features a test section specifically designed for aeroacoustic measurements with very low turbulence levels (0.01% to 0.02% at the speeds used in this experiment). For more detail on the flow facility and acoustic corrections, see references [10, 11].

A two-bladed Teignbridge Sailor 2 sailboat propeller (Figure 6.1) with a 0.457-m diameter and a 0.406-m pitch was selected to act as the test bed for the finlets. The propeller was chosen to be compatible with an existing drive and support system used previously by Alexander *et al.* [12]. The propeller has blades with a relatively large chord (0.185 m at maximum), which aids in growing a more well-developed turbulent boundary layer, in turn increasing the chance of measuring significant levels of TBL-TE noise. Figure 6.2 shows some sample blade sections along the span. To further increase the chance of having a well-developed turbulent boundary layer near the trailing edge, the blades were tripped for some runs using 0.5-mm high serrated tape (Glasfaser-Flugzeug-Service GmbH 3D Turbulator

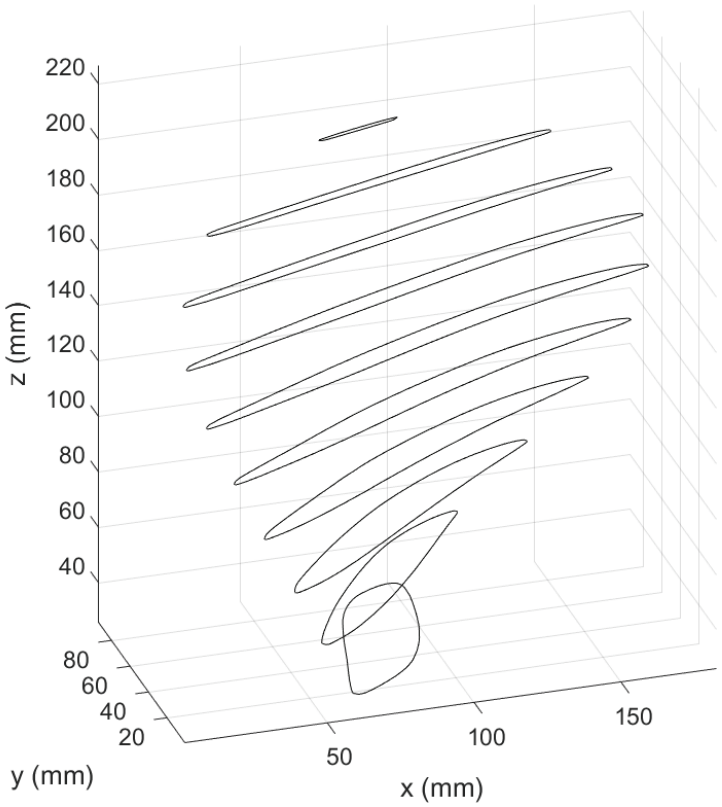

Figure 6.2: Profile slices of the propeller blade. Blade radius increases in the positive z-direction, and the blade rotates in the positive x-direction in this figure. Inflow would travel in the negative y-direction.

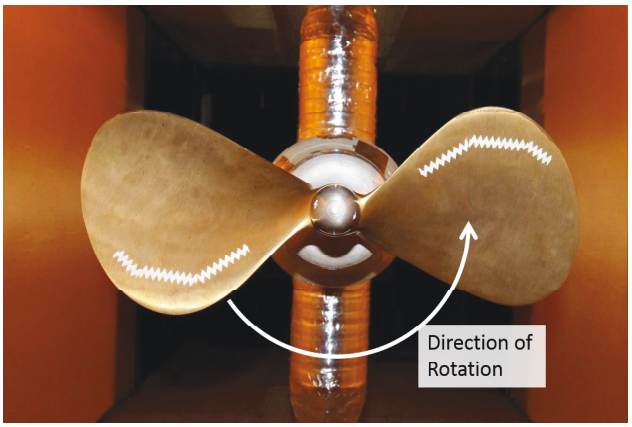

Figure 6.3: Serrated trip tape placed on propeller blades.

Tape) near the 10% chord location along the span as seen in Figure 6.3. The propeller bore was widened from its original diameter in order to accommodate the larger shaft used in the existing drive system. Although this did not affect the aerodynamics of the propeller, structural considerations dictated a maximum rotational rate of 2000 RPM. As such, all tests were run at this rotational rate, and thrust was varied by changing the inflow velocity (the free-stream velocity of the wind tunnel). The zero-thrust condition was expected to occur near an inflow velocity of 15 m/s. The Reynolds number of the outer region of the blades was calculated to be between 400,000 and 500,000 depending on radial location.

The propeller was powered by a direct drive system using a Kollmorgen AKM-64P-ACCNDA00 servomotor. The servomotor output a sawtooth signal corresponding to the instantaneous angular position of the servo. This was used to phase match hot-wire measurements as discussed in Section 6.4.3. The drive components were housed in an aerodynamically faired structure downstream of the propeller. This structure was supported from the floor and ceiling of the wind tunnel test section by a 88.9 mm diameter pipe. The center of the propeller's blade hub was located 0.724 m upstream of the center of this supporting pipe. The structure can be seen in Figure 6.4.

6.3.2 Finlets

Applying finlets to a rotating propeller presented some new challenges related to their design. Previously, finlets have only been applied to fixed airfoils, which makes it a trivial matter to align them with the expected flow direction. For this study, the flow field around the propeller was expected to be more complex. At the very least, the flow over the majority of the propeller was expected to follow a circular path when viewed in the rotating frame. Near the tips, it was expected that radial flow would lead to deviations from this circular flow path. Unfortunately, as the tips experience the maximum flow speed, they are also the region where aerodynamic noise is dominant so the finlet geometry is important here. The

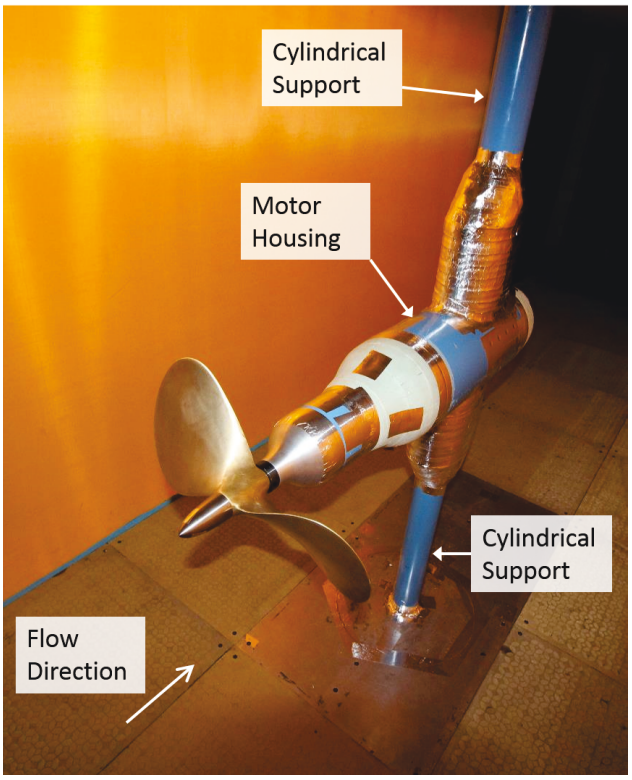

Figure 6.4: Propeller with support structure downstream.

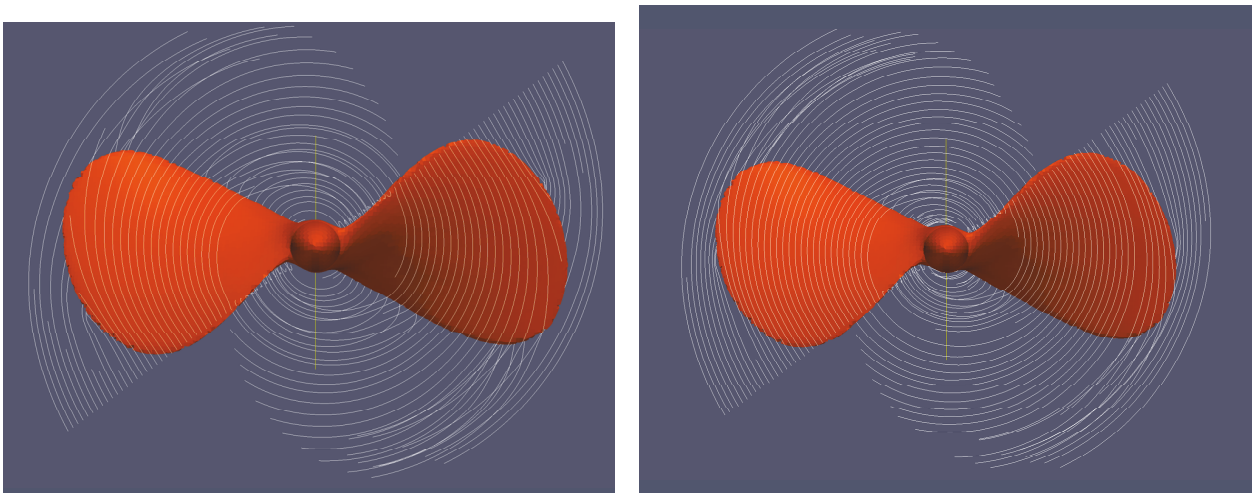

(a) 15 m/s inflow (b) 12.4 m/s inflow

Figure 6.5: Streamlines of flow around propeller at 2000 RPM.

Figure 6.6: Close-up photograph of configuration 1 finlets attached to propeller.

results of Clark *et al.* [9] suggest that finlets are tolerant of skew relative to the flow direction up to approximately 10°. Nevertheless, to maximize effectiveness, it was desired to align the finlets as closely as possible to the flow direction. As such, a simple RANS flow simulation was run in order to compute the streamlines of the flow around the blades. The propeller was laser-scanned with an expected dimensional accuracy of better than 0.2 mm in order to obtain a computer model to use with the simulation.

The flow simulation was performed using the software package OpenFOAM [13]. The simulation was run for a rotational rate of 2000 RPM to match the planned experiment, with inflow velocities of 15 m/s and 12.4 m/s, for near-zero thrust and light thrust, respectively. The results are shown in Figure 6.5.

Once the simulation was complete and the streamlines were known, the finlets could be

Table 6.1: Finlets tested and measurements taken.

Configuration	Height (mm)	Spacing (mm)	Thickness (mm)	Acoustics	Hot-Wire	Pitot
0 (No Finlets)	-	-	-	Tripped/Untripped	Tripped	Tripped
1	4	4	0.5	Tripped	No	No
2	4	2	0.5	Tripped/Untripped	Tripped	Tripped

designed to follow the flow for a given condition. Once designed, the finlets would be manufactured using a three-dimensional printing process. This allowed the finlets to be slightly flexible, but not enough such that the finlets could be molded to the shape of the propeller blades after manufacture. As such, the finlet substrate was designed to exactly match the shape of the propeller blades. Then, each finlet was designed to have a shape similar to that of Clark *et al.* [9, 10].

The final aspect of the finlet design was to choose the geometric parameters such as height, spacing, and thickness of the individual finlets. Previous experiments have suggested that the height of the finlets should occupy 25-50% of the boundary layer. XFOIL [14] calculations indicated that the boundary layer at the trailing edge would be on the order of 8 mm. As such, the finlet height was chosen to be 4 mm. It has also been shown that finlet thickness should be as small as possible to avoid disturbing the mean flow. The thickness for this experiment was chosen to be 0.5 mm, as this was the minimum thickness possible considering the manufacturing process. Finally, the optimum spacing between the finlets has been shown to be as small as possible without causing significant blockage at the trailing edge which could lead to additional vortex shedding. An open area percentage of 75% or higher has been shown to yield the best performance, although this dimension is possibly the least understood in terms of its effect on noise and aerodynamic performance. As such, two finlet configurations were designed and manufactured, one with a spacing of 2 mm and one with a spacing of 4 mm.

Table 6.1 shows a summary of the finlets tested, along with the measurements taken for each configuration. Figure 6.6 shows a close-up view of the configuration 1 finlets as they were attached to the propeller during testing. The finlet substrate was glued to the propeller surface during testing, and the edges of the substrate were faired using 0.1-mm thick aluminum foil tape.

6.3.3 Microphones

Sound produced by the propeller was measured using a 251-microphone phased array. This array was designed to cover the entire useable area of one Kevlar wall of the Virginia Tech Stability Wind Tunnel with a total area of 3.66 m×1.75 m. Each microphone in the array is a custom GRAS 40PH-S5 1/4" microphone and is held in an open frame comprised of waterjet-cut panels. This frame is supported by an outer extruded aluminum frame. The microphones in the array are normally arranged in four interlocking spirals. However, for this test cam-

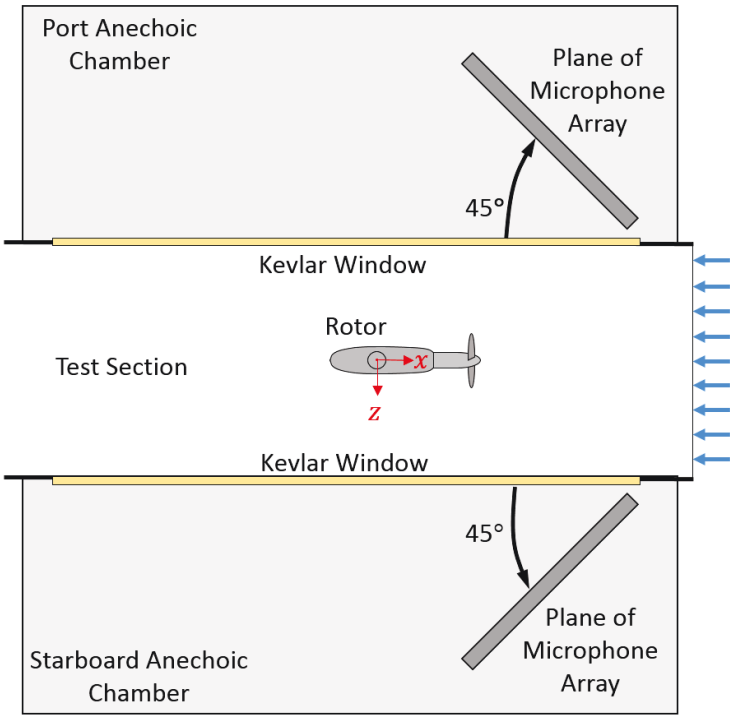

Figure 6.7: Schematic of test setup showing rotor structure in test section with 2 half-arrays in adjacent anechoic chambers.

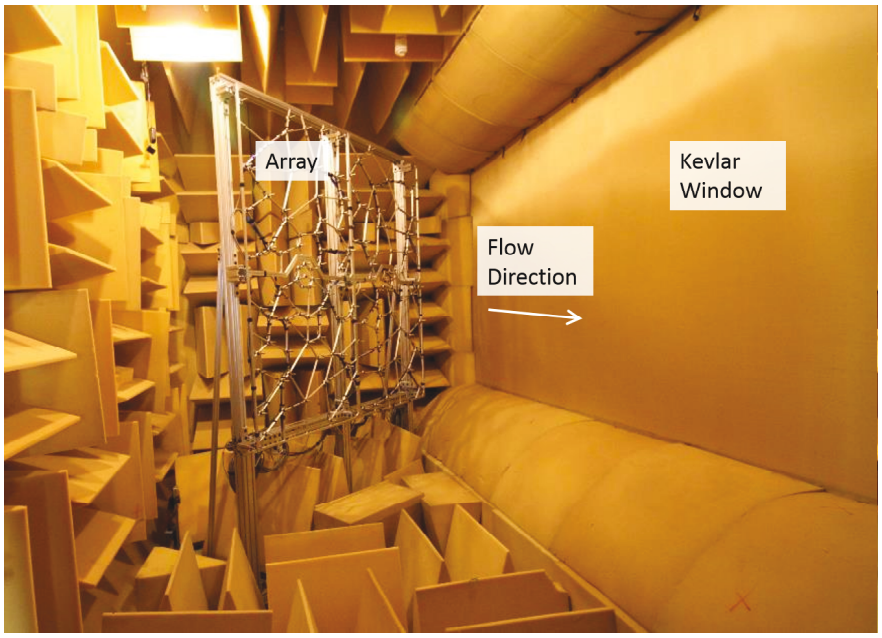

Figure 6.8: Picture of the half-array set up in the port-side anechoic chamber.

paign, the array was split in half to make two arrays with dimensions of 1.83 m×1.75 m. One half-array was placed in the port-side anechoic chamber, and the other was placed in the starboard-side anechoic chamber. Each was placed at a 45° angle relative to the direction of the free-stream flow in the test section. The center of each half-array was upstream of the propeller disk plane. A schematic view of the arrangement can be seen in Figure 6.7, and one half-array can be seen in Figure 6.8. The response of the array in this configuration was calibrated using a spark source placed at the location of the center of the propeller disk (the test section was empty at the time of calibration). Acoustic foam walls were placed at the upstream and downstream ends of the test section to eliminate acoustic reverberation around the wind tunnel circuit during calibration.

The microphone signals were sampled at 51200 Hz for 32 seconds using a custom data acquisition system. The data were passed through a 20-kHz anti-aliasing filter. The raw time series were processed by Fourier transforming blocks of 8192 samples using a Hanning window and an overlap of 50% between blocks. The diagonal elements of the cross-spectral matrix were removed to eliminate uncorrelated noise from the acoustic beamform maps.

6.3.4 Hot-Wire Probe

In order to obtain more detailed data of the flow around the propeller with and without finlets, a hot-wire probe was placed just downstream of the blades and traversed in the radial direction. Because the hot-wire system was acoustically noisy, data obtained by

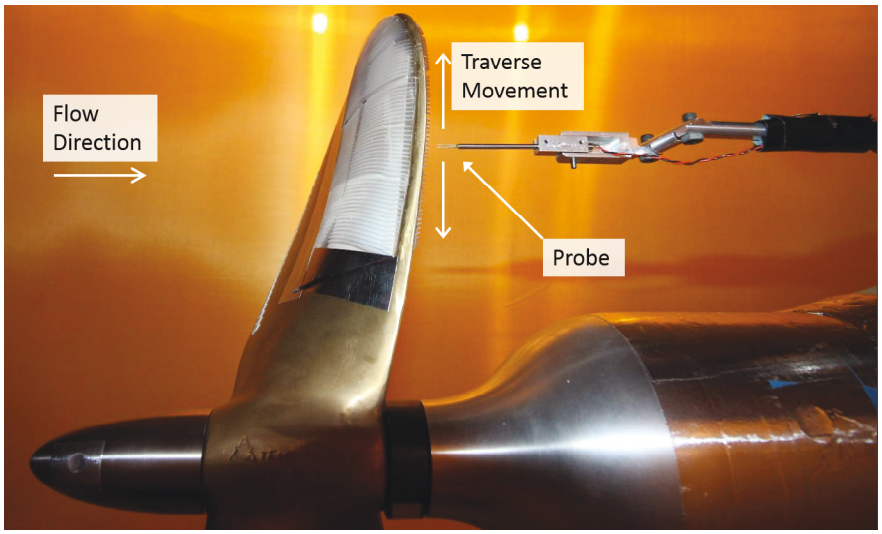

Figure 6.9: Picture of probe mounted just downstream of propeller blades with finlets attached.

the microphones were not taken when the hot-wire system was present. The traversing system was comprised of a computer-controlled Velmex single-axis traverse attached to the main structural rotor housing. A sting arm extended upstream from the traverse, and the hot-wire probe was mounted on the end. The hot-wire probe itself (Auspex Corporation model AHWU-100) was comprised of a 1-mm long sensor held between two parallel prongs. The probe was mounted in the vertical direction such that the sensor was aligned with the radius along which it was traversed (see Figure 6.9). The sensors were operated at a constant temperature using a constant temperature anemometer bridge (Dantec Dynamics StreamLine). Data was collected through a 4-channel, 24-bit National Instruments model 9239 data acquisition module sampling all channels simultaneously at 50 kHz. The probe was regularly calibrated for velocity by traversing the probe into the wind tunnel free-stream at least six inches beyond the edge of the propeller. Temperature drift was accounted for using the method given by Bearman [15].

6.4 Results and Discussion

6.4.1 Acoustics

Acoustic results were obtained for the untreated propeller in both untripped and tripped configurations, and with both finlet configurations in the tripped configuration. Configuration 2 finlets were tested with the propeller untripped as well. The propeller was tested at 2000 RPM with inflow velocities ranging from 10 m/s to 20 m/s in increments of 1 m/s. The data obtained by the microphone array were beamformed at frequencies between 500 Hz and

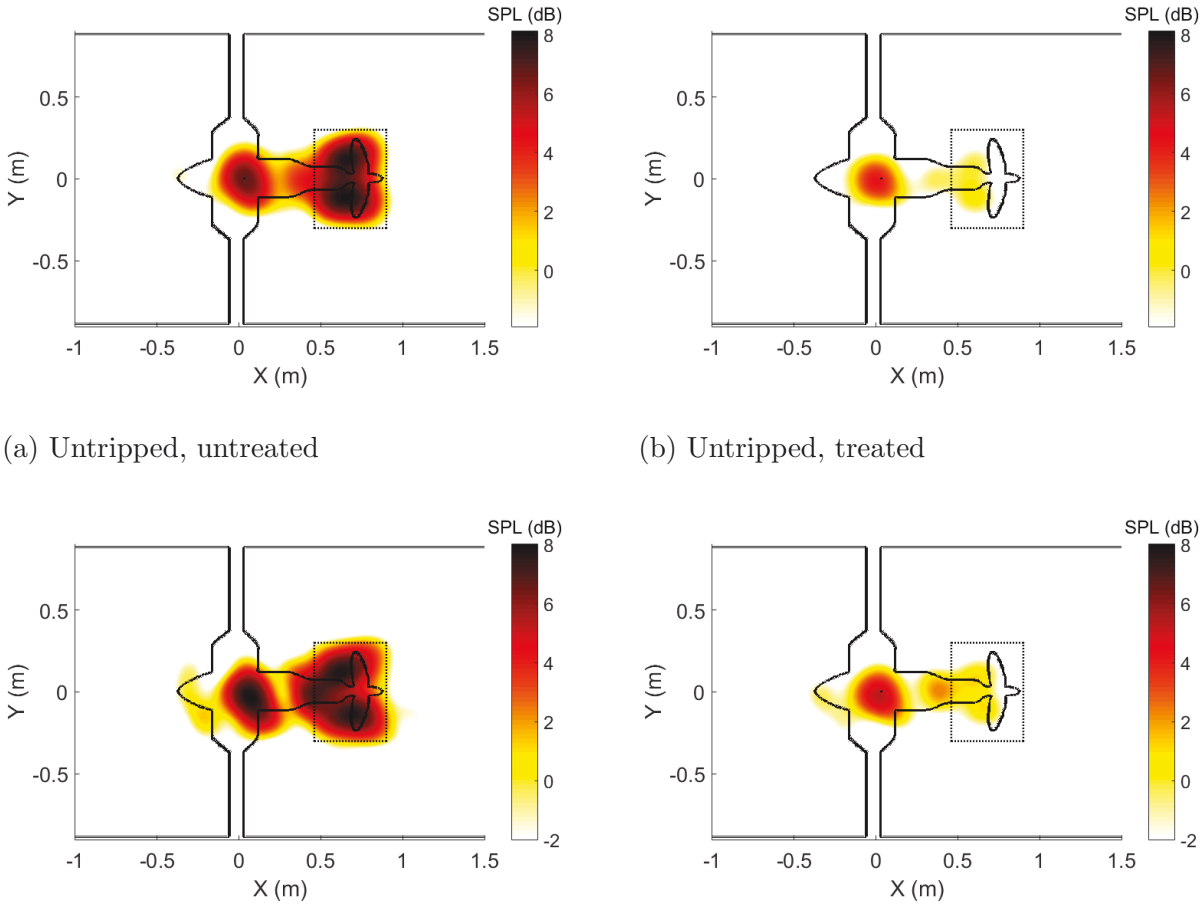

(a) Untripped, untreated

(b) Untripped, treated

(c) Tripped, untreated

(d) Tripped, treated

Figure 6.10: Acoustic beamform maps at 2500 Hz of the untripped and tripped propeller with 14 m/s inflow showing the effects of treatment by the configuration 2 finlets.

10000 Hz.

Figure 6.10 shows beamform maps from the untripped and tripped propeller with and without configuration 2 finlets applied. The beamform maps are for a single frequency (2500 Hz) only. The outline of the support structure and propeller is overlayed on the beamform images for physical reference. As seen in the maps of the untreated propeller, the noise is dominated by sources near the propeller location. The shape of the source shows two main nodes above and below the axis of rotation suggesting that the noise is indeed from the propeller blades. The treatment appears to be highly effective at reducing noise from the blades, as levels in the blade region drop by nearly 10 dB when finlets are applied. Interestingly, for the treated cases, there is also a significant drop in noise level from the source at the support structure downstream. This suggests that some of this noise may be due to acoustic reflections of

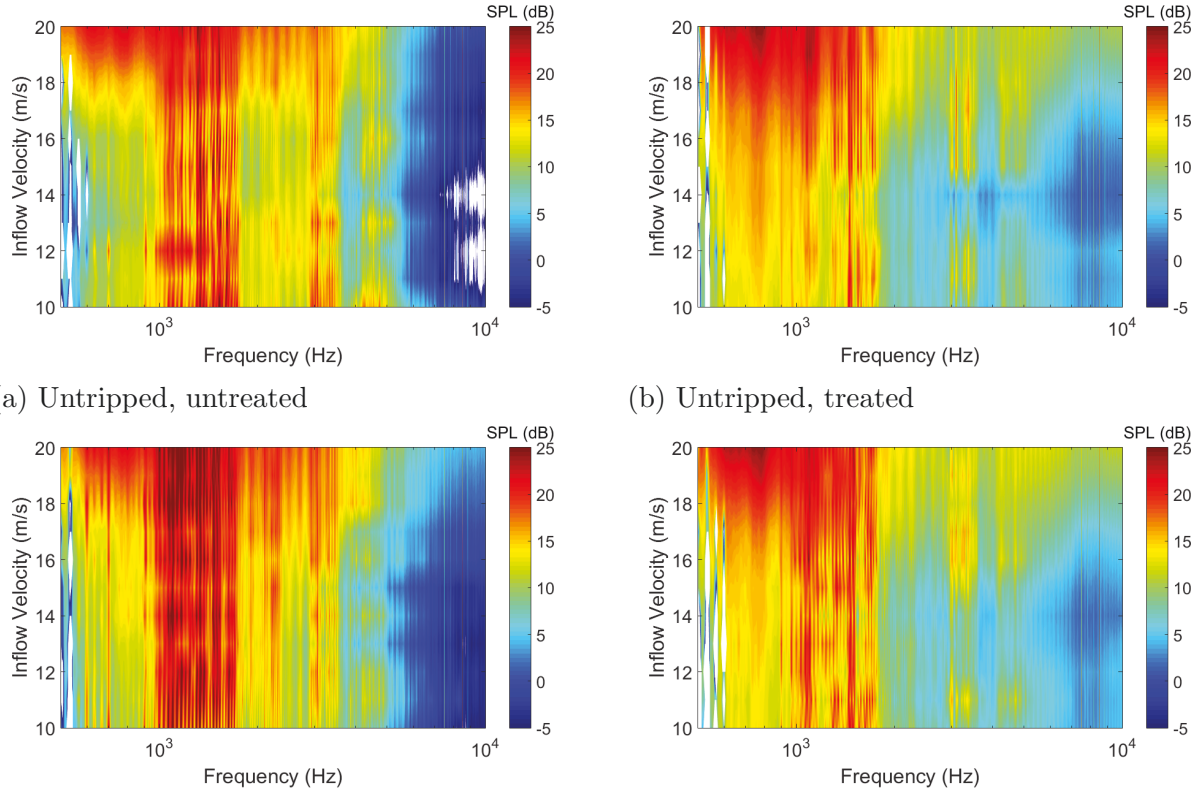

(a) Untripped, untreated

(b) Untripped, treated

(c) Tripped, untreated

(d) Tripped, treated

Figure 6.11: Contour maps showing integrated noise levels from the dashed region in Figure 6.10 across inflow velocities from 10 to 20 m/s, showing the effects of adding the finlet configuration 2 treatment to the untripped and tripped blades.

blade noise off of the irregular surface of the support structure.

The dashed box in Figure 6.10 denotes the region over which the beamform maps for each frequency were integrated to generate noise spectra. By integrating only over the region around the propeller, the mechanical noise from the motor and any background noise from the structure can be neglected from the analysis. Larger integration regions were investigated during the analysis, but these larger regions were more likely to lead to include spurious noise sources downstream which were visible at other frequencies. Regardless, moderate changes in the size of the integration region were not observed to significantly impact the conclusions drawn from the data.

The integrated noise spectra can be plotted for all inflow velocities as a contour map, as shown in Figure 6.11. Although noise levels are somewhat low at these conditions, integration of measurements taken with the support structure installed but the propeller removed yielded spectral levels below -10 dB at all frequencies above 600 Hz.

As seen in Figure 6.11, the tripped untreated blades generate more noise than the untripped

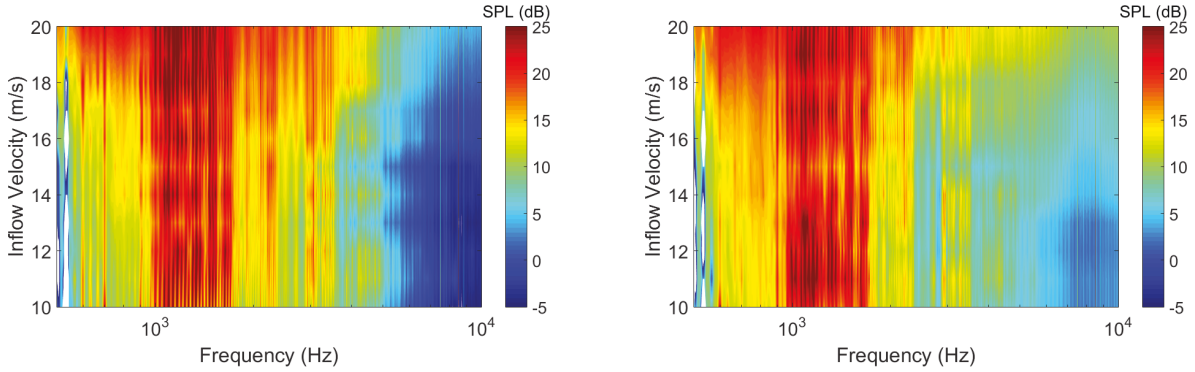

(a) Tripped, untreated

(b) Tripped, treated

Figure 6.12: Contour maps showing integrated noise levels across inflow velocities from 10 to 20 m/s, showing the effects of adding the finlet configuration 1 treatment to the tripped blades.

blades particularly in the peak frequency range from 1 to 2 kHz. Additional local peaks are observed for the tripped case in the frequency range from 2 to 3 kHz. For both the untripped and tripped cases, a sharp increase in broadband noise is observed beginning around 17 m/s. This is likely caused by flow separation when the blades are at high negative angles of attack (due to the higher inflow velocity).

The finlets appear to have made a significant impact on the noise across a wide frequency range. At moderate inflow velocities (10-18 m/s), the noise appears to have been reduced in the frequency range of 1-2 kHz, and in the range from 2-4 kHz for the tripped case in particular. Some additional low frequency noise is observed at frequencies below 1 kHz. In addition, it is clear that the finlets produce additional high-frequency noise across all inflow velocities, but especially for the highest inflow velocity.

Finlet configuration 1 was tested only with the tripped blades. For the sake of brevity, we only show contour maps of the noise for this configuration. As seen in the figures, configuration 1 is somewhat less effective than configuration 2, but still reduces noise particularly at higher inflow velocities in the frequency range above 2 kHz. The additional noise at low (< 1 kHz) and high (> 5 kHz) frequencies is again observed.

6.4.2 Comparison with Noise Predictions

Brooks, Pope, and Marcolini [1] developed empirical relations for the noise produced by airfoils and flat plates due to TBL-TE noise as well as TEB-VS noise. Although some assumptions are necessary, these relations can be used to provide a low-order estimate of the expected noise from the propeller. More importantly, the relations can be used to identify the frequency ranges where each source of noise will be dominant. To begin, the propeller

was assumed to be "frozen" in place with the blades moving directly towards the anechoic chambers (i.e., the effect of rotation was not taken into account for this prediction) and the observer location was taken to be the center of the microphone array towards which the blade was moving. Next, the majority of noise was assumed to be produced by the outer 40%, or 0.1 m, of the blade radius, where flow velocity was highest. The blade chord and flow velocity (due to rotation of the blades) were assumed to be constant and equal to the average physical values in this region, 0.16 m and 42 m/s respectively. The calculations were performed for a tripped airfoil at an angle of attack of zero degrees. The trailing edge thickness of the blades was measured as 4 mm.

The results of the calculation are shown and compared with experimental results in Figure 6.13. The results shown are for the tripped blades with an inflow velocity of 14 m/s when the blades were at low angle of attack. This acoustic results at this condition are typical of the noise results obtained from relatively low inflow velocities, and the angle of attack of the blades is near the value used in the prediction. The noise prediction reveals that the spectral peaks for trailing edge noise and bluntness noise share approximately the same Strouhal number based on trailing edge thickness (h) and average velocity over the blades (U_{av}) of 0.14, which corresponds to a dimensional frequency of 1400 Hz. The noise due to the trailing edge bluntness only contributes significantly to the overall noise in the non-dimensional frequency range from 0.1 to 0.2, and trailing edge noise is dominant at all other frequencies. The spectral peak of bluntness noise is nearly 15 dB higher than that of trailing edge noise.

Considering now the comparison with experimental results, particularly the untreated case, it can be seen that high noise levels are measured in the range of Strouhal numbers from 0.09 to 0.18. Here, the measured values are averaged over 1/6th octave bands for clarity of presentation while maintaining normalization of spectral values on a 1 Hz bandwidth. Although there is some misalignment between the peak frequencies and levels of the predicted and measured spectra, the agreement is acceptable considering the assumptions made for the prediction. The comparison thus presents strong evidence that trailing edge bluntness is responsible for the high measured spectral values in this frequency range. It is also seen that spectral levels are significantly reduced in this frequency range by up to 8 dB when finlets are applied. Further, the noise reduction is retained at higher frequencies when trailing edge noise becomes the dominant component of the total noise. These results indicate that the finlets are effective at reducing both relevant sources of noise present on the propeller. Note that the increases in noise at the lowest and highest frequencies observed in the contour plots of Figure 6.11 are visible in these line spectra as well.

6.4.3 Hot-Wire Results

Preliminary results obtained from the hot-wire probe are now presented. Hot-wire data was collected at a smaller subset of inflow velocities because of the longer acquisition time

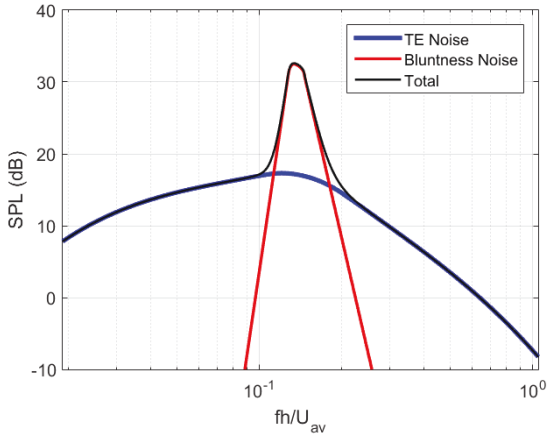

(a) Predicted noise sources

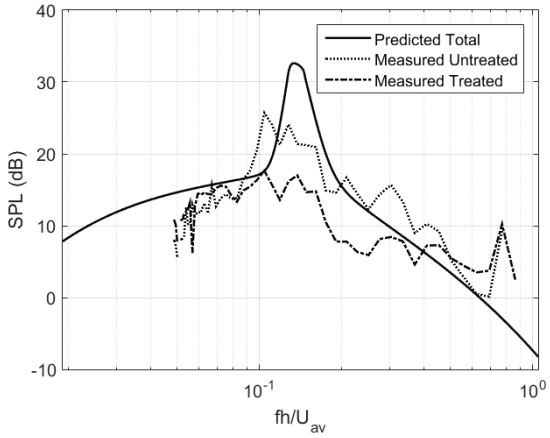

(b) Measured noise compared with predicted levels

Figure 6.13: Acoustic spectra of the predicted and measured noise levels. Measured spectra shown here are for a 14 m/s inflow velocity, and the treated case refers to finlet configuration 2.

compared to acoustic measurements, especially when taking radial profiles. To determine meaningful statistics from the hot-wire data, the time series obtained by the hot-wire must first be binned based on the position of the blades. To accomplish this, the sawtooth signal output by the servomotor driving the propeller was idealized to obtain a clean series of values free of spurious voltage artifacts. The hot-wire time series values were then binned based on the level of this sawtooth at the time the data points were obtained. By collecting data at 50 kHz for 30 seconds, and then binning over a rotation arc of 1°, roughly 4000 samples are obtained for each bin. The values can then be averaged to find the mean flow velocity or used to find turbulence intensity at each point. Figure 6.14 shows mean flow velocity and turbulence intensity for both the untreated propeller and the propeller treated with configuration 2 finlets.

As seen in Figure 6.14, the blade passage is clearly visible in both the mean velocity and turbulence intensity maps. The probe was traversed well past the blade tips. In these maps, the blade rotation is clockwise. The mean velocity maps show a slight increase in velocity over the entire propeller disk, with a stronger increase at the blade passage. The increase in velocity is much stronger when the finlets are present, suggesting an increase in drag on the blades. The turbulence intensity plots are near zero throughout the majority of the propeller disk, with a significant increase at the blade passage. The initial influence of the propeller's trailing edge is seen as a sharp line, particularly when finlets are present, and the intensity fades as the blades continue to turn. The turbulence intensity levels increase when finlets are present, and there are more well-defined streaks that appear downstream of the initial passage of the trailing edge, likely due to the irregular nature of the finlet geometry.

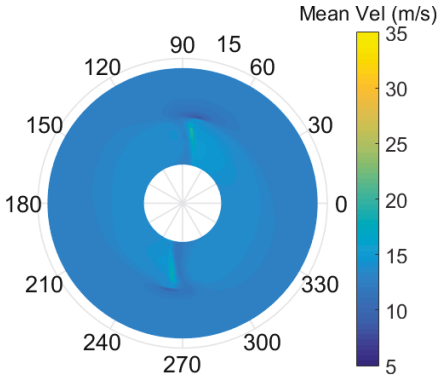

(a) Mean velocity, untreated

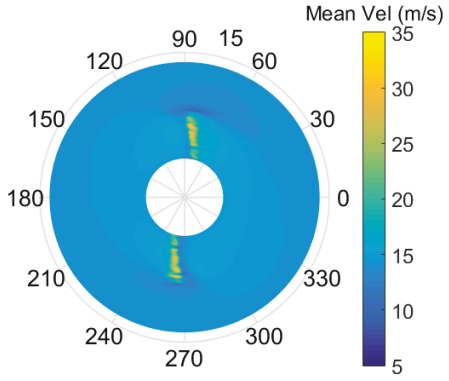

(b) Mean velocity, treated

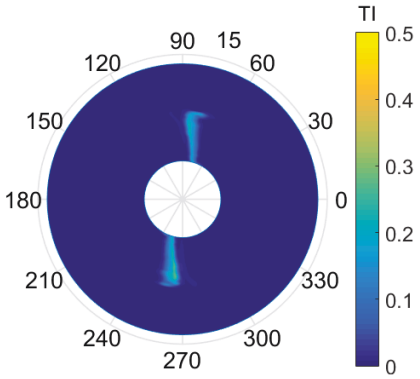

(c) Turbulence intensity, untreated

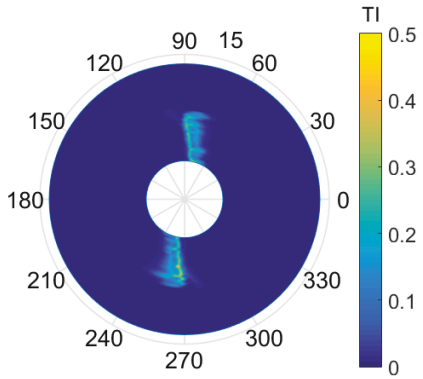

(d) Turbulence intensity, treated

Figure 6.14: Phase-averaged mean velocity and turbulence intensity values obtained by a hot-wire probe traversed downstream of the propeller, with an inflow velocity of 13 m/s.

The hot-wire results give some insight into the possible methods for noise reduction in this case, particularly when compared with the results of Chapter 5 of this dissertation. It was found that the finlets were likely to create their own turbulence as boundary layers formed on the surfaces of the finlets themselves. If the velocity in the boundary layer near the finlet was slow enough, it was found that the presence of the finlets would greatly increase the velocity deficit in the channels between them. The hot-wire results suggest a similar mechanism at work here, as the velocity data indicate that the finlets are "pulling" more fluid through the rotation than the propeller alone. The higher turbulence levels in the wake also suggest that the finlets exert a significant influence on the naturally occurring turbulence of the propeller blades' boundary layers. The data therefore supports the theory that the finlets reduce trailing edge noise through the same mechanism as observed for a stationary airfoil, while the additional turbulence in the flow near the trailing edge tends to suppress the formation of vortices at the blunt trailing edge. At the least, the vortices at the blunt trailing edge are likely to be uncorrelated over more than one finlet channel, as the uncorrelated turbulence in each finlet channel influences the formation of vortices at the trailing edge. The significant reduction in correlation lengthscale is expected to lead directly to a reduction in far-field sound observed.

6.5 Conclusions

Experimental investigations have been performed to analyze the effects of finlets on the noise produced by a marine propeller. Two sets of finlets were tested on a propeller spinning at 2000 revolutions per minute with inflow speeds of 10 to 20 m/s. Acoustic measurements were obtained with a 251-microphone phased array, and flow measurements were performed using a single hot-wire probe traversed just downstream of the propeller blades. Results indicated that closely-spaced finlets were effective at reducing both trailing edge noise and vortex shedding noise due to the blunt trailing edge. Widely spaced finlets were less effective. Noise predictions using the methods of Brooks, Pope, and Marcolini [1] revealed the frequency ranges where each source of noise was dominant, allowing for more detailed analysis of the acoustic results. The flow results indicated that the mechanism for noise reduction was likely similar to the noise reduction mechanism observed with finlets placed on a stationary airfoil in previous experiments. The data showed that the finlets produced additional turbulence near the trailing edge which was likely uncorrelated over multiple finlet channels, thus reducing the spanwise correlation lengthscale of both the natural turbulence present in the boundary layers of the propeller blades as well as that of the discrete vortices shed from the blunt trailing edge.

6.6 Acknowledgements

The authors would like to sincerely thank the Office of Naval Research, in particular Dr. Ki-Han Kim, for their support under grant numbers N00014-15-1-2721, N00014-14-1-0141, and N00014-16-1-2395. The authors are grateful to Mr. Nick Molinaro, Mr. Christopher Hickling, and Mr. Anthony Millican for their assistance during the experiment.

References

[1] Brooks, T. F., Pope, D. S., and Marcolini, M. A., "Airfoil Self-Noise and Prediction," Tech. rep., NASA, 1989.

[2] Howe, M. S., "Aerodynamic Noise of a Serrated Trailing Edge," *Journal of Fluids and Structures*, Vol. 5, 1991, pp. 33–45.

[3] Oerlemans, S., Fisher, M., Maeder, T., and Kögler, K., "Reduction of Wind Turbine Noise Using Optimized Airfoils and Trailing-Edge Serrations," *AIAA Journal*, Vol. 47, No. 6, 2009, pp. 1470–1481.

[4] Herr, M. and Dobrzynski, W., "Experimental Investigations in Low-Noise Trailing Edge Design," *AIAA Journal*, Vol. 43, No. 6, 2005, pp. 1167–1175.

[5] Graham, R. R., "The silent flight of owls," *The Journal of the Royal Aeronautical Society*, Vol. 38, 1934, pp. 837–843.

[6] Kroeger, R. A., Grushka, H. D., and Helvey, T. C., "Low Speed Aerodynamics for Ultra-Quiet Flight," Tech. rep., Air Force Flight Dynamics Laboratory, 1972.

[7] Jaworski, J. W. and Peake, N., "Aerodynamic noise from a poroelastic edge with implications for the silent flight of owls," *Journal of Fluid Mechanics*, Vol. 723, 2013, pp. 456–479.

[8] Lilley, G., "A study of the silent flight of the owl," *4th AIAA/CEAS Aeroacoustics Conference*, American Institute of Aeronautics and Astronautics, Toulouse, France, jun 1998.

[9] Clark, I., Alexander, W. N., Devenport, W. J., Glegg, S. A., Jaworski, J., Daly, C., and Peake, N., "Bio-Inspired Trailing Edge Noise Control," *21st AIAA/CEAS Aeroacoustics Conference*, American Institute of Aeronautics and Astronautics, Dallas, Texas, jun 2015.

[10] Clark, I., Baker, D., Alexander, W. N., Devenport, W. J., Glegg, S. A., Jaworski, J., and Peake, N., "Experimental and Theoretical Analysis of Bio-Inspired Trailing Edge Noise Control Devices," *22nd AIAA/CEAS Aeroacoustics Conference*, American Institute of Aeronautics and Astronautics, Lyon, France, may 2016.

[11] Devenport, W. J., Burdisso, R. A., Borgoltz, A., Ravetta, P. A., Barone, M. F., Brown, K. A., and Morton, M. A., "The Kevlar-walled anechoic wind tunnel," *Journal of Sound and Vibration*, Vol. 332, No. 17, 2013, pp. 3971–3991.

[12] Alexander, W. N., Molinaro, N. J., Hickling, C., Murray, H., Devenport, W. J., and Glegg, S. A., "Phased Array Measurements of a Rotor Ingesting a Turbulent Shear Flow," *22nd AIAA/CEAS Aeroacoustics Conference*, American Institute of Aeronautics and Astronautics, Lyon, France, may 2016.

[13] Weller, H. G., Tabor, G., Jasak, H., and Fureby, C., "A tensorial approach to computational continuum mechanics using object-oriented techniques," *Computers in Physics*, Vol. 12, No. 6, 1998, pp. 620–631.

[14] Drela, M., "XFOIL: An analysis and design system for low Reynolds number airfoils," 1989.

[15] Bearman, P. W., "Corrections for the effect of ambient temperature drift on hot-wire measurements in incompressible flow," *DISA Information*, Vol. 11, No. 1, 1971, pp. 25–30.

Chapter 7

Conclusions and Outlook

The work presented in this dissertation has focused on two sources of aerodynamic noise: rough surfaces and trailing edges. Both of these noise sources are relevant to real-world applications, and reducing or attenuating these sources can lead to tactical advantages, economic benefits, and improved quality of life for those living or working near aerodynamically noisy structures. The experiments and developments of this dissertation are aimed at providing new solutions to the noise problem while demonstrating the viability of these solutions for application to real structures.

The method of roughness noise control described in Chapter 3 was developed after detailed study of the anatomy of owls' feathers. The unique features of owls' wings allow these birds to fly silently. In particular, the downy coating on the surface of owls' feathers was examined as previously-published literature suggested that this feature played a significant role in the reduction of flight noise, but few studies exist which seek to replicate this feature in an engineering context. Sparse fabric canopies were chosen for experimentation by suspending them above rough surfaces in the Virginia Tech Anechoic Wall-Jet Wind Tunnel. This replicated the observed characteristics of the downy surface, which was seen to consist of small hairs which rose from the surface of the feather before bending over to form a similar canopy-type feature.

The results of these wind tunnel experiments showed that the canopies were effective at reducing far-field noise from rough surfaces underneath, but that certain configurations generated significant high-frequency noise. The data suggested that fibers which were not oriented parallel to the flow direction created additional noise. As such, a separate set of canopies, with fibers oriented only in the flow direction and supported from the streamwise ends of the fibers, were tested and found to reduce the total measured noise at all frequencies relative to the uncovered rough surface. In addition, the canopies were found to lead to reductions in the magnitude of pressure fluctuations sensed at the surface itself by up to 30 dB, or up to three orders of magnitude. This finding explained the mechanism by which the canopies reduce noise, as it is these pressure fluctuations which scatter from the rough surface into the far-field, creating noise.

The findings of this experiment led to inspiration which yielded the trailing edge finlets investigated in Chapters 4, 5, and 6. It was thought that if the canopies were effective at attenuating surface pressure fluctuations on a rough surface, a similar surface feature

could be designed for use on an airfoil to reduce these same surface pressure fluctuations in the region near the trailing edge, thereby reducing noise arising from pressure scattering at this edge. The first experiment (described in Chapter 4) is best described as a proof-of-concept study, in which a series of finlets were placed at the trailing edge, mimicking the geometry of the unidirectional canopies successfully tested over rough surfaces. Over twenty configurations were tested, with acoustic and lift measurements available for all cases. These measurements were used to determine the effects of various geometric parameters of the finlets such as maximum height, spacing between each finlet, and thickness of each finlet. Tests were also performed to determine the effect of extending the finlets past the trailing edge.

The results of this experiment showed that the finlets were effective at reducing trailing edge noise from a typical wind turbine airfoil by up to 10 dB across a wide frequency range. Finlet configurations with different maximum heights were tested, and it was found that larger finlets tend to produce more noise reduction. Similarly, the results showed that closely-spaced finlets perform better up to the point where blockage at the trailing edge leads to vortex shedding from the effectively-blunt trailing edge. Finlets with no trailing edge extension were found to yield slightly more noise reduction, although the true contribution of this result was proof that the finlets functioned by modifying the turbulence upstream of the trailing edge, and not by altering the scattering geometry of the trailing edge itself. The effect of finlet thickness was less clear, as the effect of thicker finlets was mixed over different frequency ranges when compared to thinner finlets. Preliminary lift measurements obtained during this test showed the finlets to have a negligible aerodynamic effect, although significant increases in drag were observed for those cases where drag data was available.

In order to better understand the noise reduction mechanism of the finlets, a new investigation (described in Chapter 5) was designed to understand the detailed flow statistics near the trailing edge of an airfoil with and without finlets. A computational study was undertaken which simulated the flow over the same DU96-W180 wind turbine airfoil used in experiments. A companion experiment was designed which featured microphones at the trailing edge of the airfoil itself for measurements of surface pressure fluctuations. In addition, an improved configuration of mean pressure taps was incorporated which would allow measurements to be taken along the entire chord of the airfoil even with finlets installed.

The results of this investigation revealed the effect that the finlets were having on the flow and associated turbulence near the trailing edge. It was found that the suction and pressure side finlets had different effects on the mean flow, but that the finlets on each side contributed to the noise reduction. The suction side finlets were observed to produce a significant velocity deficit in the channels between them. This effectively reduced the magnitude of turbulent velocity fluctuations and, consequently, the pressure fluctuations at the surface. The finlets also reduced the spanwise correlation lengthscale of the turbulence near the trailing edge, essentially breaking up any large scale turbulent structures which would otherwise contribute greatly to the far-field noise. The pressure side finlets were not found to create a large velocity deficit in the channels, but instead produced boundary layers which

grew into the channels. The data suggested that these boundary layers contained their own turbulence which interacted with the turbulence which would otherwise be present in the airfoil's boundary layer. This interaction effectively decorrelated the turbulence over the span, again leading to reduced noise by breaking up any large coherent structures which would produce significant noise. Methods of noise prediction previously developed in the literature were used to relate the effect of the finlets on surface pressure to the change in far-field noise. The prediction scheme was found to capture the trends observed in the measurements with some variation at certain frequencies. Overall, however, the agreement was acceptable and opens a path to further use of this method for prediction of far-field noise by finlets.

As a final investigation, an experiment (described in Chapter 6) was designed which sought to investigate the applicability of finlets to a rotating system. A marine (sailboat) propeller was used as a testbed for this purpose. Measurements were taken of noise and flow downstream of the propeller, which was rotating at 2000 revolutions per minute. Two configurations of finlet were tested, one of which was found to significantly reduce noise over a wide range of frequencies. Flow measurements downstream of the propeller suggested that the finlets increased the drag of the propeller by entraining more fluid and causing a greater change in flow velocity as the propeller blade passed the velocity probe. When one considers the flow in the rotating frame of the propeller, however, it can be surmised that this situation is very similar to that observed in the previous investigation in which the finlets cause a significant velocity deficit in the channels between them. It was observed that this deficit led to significant noise reduction, which was corroborated by the measurements of the noise from the propeller.

Previously-developed methods of noise prediction were utilized to gain insight into the noise sources of the propeller, and it was found that a significant portion of the measured noise was due to the blunt trailing edge of the propeller blades. This noise was observed to be significantly attenuated by the finlets. This result indicates that the process of modifying the flow upstream to reduce noise is valid not only for smooth flow over a streamlined wing, but also for a structure with blunt edges. This result increases the usefulness of the finlets for a greater variety of applications, such as near the root of wind turbine blades which frequently feature a blunt trailing edge.

The devices described in this dissertation, particularly the finlets, have strong potential for application to real engineering structures. Their ability to reduce noise under certain conditions has been clearly demonstrated. However, as this dissertation resembles the first body of work which studies these devices, many questions remain unanswered, and some barriers exist to their implementation under real-world conditions. Research into further improvement of the finlets would be useful and necessary. In particular, there are several performance metrics that can be addressed, both through experimentation and flow simulation.

The finlets have been shown to have negligible or even negative impact on the low-frequency noise emitted by the trailing edge. As wind turbine noise is dominated by low-frequency noise, and since low-frequency noise propagates efficiently over long distances, this perfor-

mance deficit severely limits the current utility of the finlets. Remedies for this condition may involve reworking the finlets' geometric parameters to exert more influence on the largest turbulent eddies responsible for low frequency noise. To retain the finlets' effect on higher frequencies, larger finlets may be combined with smaller finlets in a manner similar to configurations F6 and F7 referenced in Chapter 4. To evaluate the effectiveness of this type of configuration, it may be useful to employ Large Eddy Simulations to evaluate several design concepts and understand the flow functionality of the new design before moving to aeroacoustic wind tunnel testing. Bodling *et al.* [1] have performed Large Eddy Simulations for a NACA 0012 airfoil with and without finlets and have demonstrated that the results can be used to correctly predict the noise reduction in the mid-frequency range along with the noise increase at low frequencies. Further studies of this type will allow for greater understanding of the correlation between the physical scale of the finlets and that of the turbulent eddies to be influenced.

The experiments performed here have also shown that the finlets lose effectiveness at moderate to high angles of attack. Unfortunately, wind turbine blades normally operate at these angles to generate maximum lift and power. This presents a difficult problem, as the action of changing angle of attack has a direct influence on the turbulence lengthscales in the airfoil's boundary layer. Even worse, the turbulence structures tend to grow on the suction side with increasing angle while decreasing in size on the pressure side, due to the changing boundary layer thicknesses on each side. Speaking particularly of the suction side, as the turbulence structures grow in size, it can be expected that finlets of a given size will exert less influence on this turbulence. On the pressure side, the shrinking boundary layer may leave more of the finlets exposed to high-velocity air in the free-stream, producing more drag and potentially more noise. The results in this paper have clearly shown that the suction and pressure side finlets must be designed independently of one another to maximize performance, as the flows on each side of the airfoil can be significantly different. This stipulation becomes even more important when angle of attack is considered along with changing flow speed, which has an inverse relationship to the boundary layer thickness on both sides of the airfoil. Investigations into the effect of angle of attack and flow speed could begin by repeating the RANS simulations described in Chapter 5 for different flow conditions. The changing flow conditions could be mapped to changing acoustic performance as measured in aeroacoustic wind tunnel tests, and conclusions may be drawn from the correlation between the two.

Two potential solutions to the angle of attack problem are proposed. The first solution is to simply design the finlets for a single angle of attack and flow speed to maximize the performance at that condition. This is less than ideal, as off-design flow conditions may result in increased noise and decreased aerodynamic performance compared to the unmodified structure. The second, more technically complex solution is to design and implement actuated finlets which could be extended and retracted much like flaps of aircraft wings. This would allow control software to apply the appropriate size finlets for a given flow condition. The design of such actuated finlets would be difficult due to the limited interior space near the

trailing edge of an airfoil, but could yield ideal performance at all conditions.

The third major performance hurdle to overcome is the drag produced by the finlets. A drag rise of up to 10%, as seen in these investigations, would be detrimental to any vehicle or wind turbine. Although an increase in wetted surface area is likely to cause some of this increase in drag, it is worth noting that the finlets are shown to work best when embedded within the already-existing boundary layer of an airfoil. As such, their influence is limited to that flow which already has low momentum relative to the free-stream. More sophisticated geometric features may alleviate the problem. For example, fairing of the finlet's interface with the airfoil to eliminate the ninety-degree interior corner may prevent streamwise vortices from forming which could have a negative impact on the aerodynamics. As another example, designing a smooth, continuous shape for both the leading and trailing edges of the finlets (perhaps modeling a shark fin or other streamlined shape) could reduce any tendency of the flow to separate when encountering these edges. Simulations again could play a key role in the evaluation of new design concepts which follow these recommendations.

As a final word, it is noted here that this dissertation has introduced new methods of noise control which take an entirely different approach from traditional methods. Namely, the idea of modifying flow turbulence through the use of aerodynamically-faired elements that have a minimal effect on the mean flow is novel. The majority of existing noise-control treatments seek to modify the geometry which scatters pressure fluctuations from turbulence while ignoring the turbulence itself. It is hoped that new potential application areas for this novel method are found. The use of this method in treating other sources of noise such as aircraft landing gear, to give one example, is a particularly exciting concept. It is even possible that this type of methodology may have potential for applications beyond noise reduction. Similar structures may be useful for shielding surfaces from heat-transporting flow turbulence. Of course, such treatments may look drastically different from those presented here. The most important contribution of this dissertation is not any particular geometry or device, but rather a methodology for the treatment of noise. The author sincerely hopes that the investigations carried out here are merely the first examples of long series of new developments which utilize this methodology for noise reduction and other benefits.

References

[1] Bodling, A., Agrawal, B. R., Sharma, A., Clark, I., Alexander, W. N., and Devenport, W. J. "Numerical Investigations of Bio-Inspired Blade Designs to Reduce Broadband Noise in Aircraft Engines and Wind Turbines." *55th AIAA Aerospace Sciences Meeting*. Grapevine, Texas, 2017.